Micromagnetic simulation of nanogratings as possible devices for unidirectional spin wave propagation

Master's thesis

Markus Kügle

Garching - 31. May 2024

Supervisor: Prof. Dr. Rudolf Gross
Advisors: Dr. Stephan Geprägs, Monika Scheufele

Contents

Chapter 1

Introduction

Nowadays, the computer industry finds itself at a crossroads facing goals that seem incompatible at first sight. For one, the emergence of technologies based on artificial intelligence, combined with their need for enormous amounts of data, demands more powerful computer chips than ever before. On the other hand, the looming threats of climate change provide big incentives to strive towards increasing energy efficiency. As an example, a single ChatGPT inquiry consumes at least ten times the amount of power necessary for a Google search, with a tendency to increase for upcoming, more powerful versions [1]. Considering that some journals already list ChatGPT as a top ten contributor to science as a whole, it may be in interest of everybody that computers and thus data centers become not only more powerful but more efficient [2]. Satisfying both of these demands, however, poses a serious challenge for the classical semiconductor-based computer industry. The further miniaturization of chips is hindered by the physical limitations imposed by e.g., quantum tunneling effects, whereas simply increasing clock speeds of chips ventures into diminishing-returns territory with regards to energy consumption [3].
A possible solution to overcome these challenges may lie in the field of magnonics, which revolves around using spin waves instead of electrons to process, transmit and carry information [4, 5]. Spin waves are collective excitations of magnetically ordered systems and are often referred to by their quanta, known as magnons [5]. In theory, they offer many enticing properties towards a new generation of computing devices. For one, the dynamics of spin waves take place in the frequency regime from GHz to THz [6]. Therefore, they are compatible with current microwave technology, while also physically supporting far higher clock speeds in the future [6]. At the same time, the wavelength of spin waves is orders of magnitude smaller than that of microwaves at the same frequency, making them suitable for even nanoscale applications [6]. Moreover, the information transport via waves instead of electrons enables the possibility of vector operations, while also eliminating the concerns about Joule-heating [6]. Consequently, magnonic logic devices are theoretically capable of both, drastically increasing the computational power available while simultaneously

increasing energy efficiency.
In recent years, a focal point in magnonics research has been to create devices capable of unidirectional spin wave transport on the nanometer scale [7]. Unidirectional transport is an invaluable property for the creation of magnonic logic devices, as it allows construction of e.g., spin wave insulators and diodes, which would be the building blocks of magnonic computing units [7]. Furthermore, unidirectionality is also an important concept in microwave electronics and optics. However, these devices are usually on the centimeter scale and would therefore profit from nanometer-sized on-chip solutions based on magnonics [7].
A promising approach to realize unidirectional spin wave propagation on the nanometer scale is *chiral pumping*, as first proposed in 2019 by Yu *et al.* [8, 9]. In this framework, unidirectional spin waves are induced via dipole-coupling of an array of ferromagnetic wires (nanograting) with an underlying magnetic thin film [9]. The direction of spin wave transport is hereby controlled via an external magnetic field, which allows to leverage the higher shape anisotropy of the wires consisting the grating to realize an either parallel or anti-parallel alignment of thin film and nanograting magnetizations [9]. An experimental realization of chiral pumping in a system of a Co nanograting on a $Y_3Fe_5O_{12}$ (YIG) thin film was published by Chen *et al.* [10], reporting close to 100% non-reciprocity for spin waves of wavelengths $\lambda \approx 50\,\mathrm{nm}$. In contrast, in-house experiments in similar material systems conducted by C. Mang at WMI did not confirm such large values of non-reciprocity [11].

Consequently, in this thesis we turn to micromagnetic simulations in order to further investigate unidirectional spin wave propagation in systems of nanogratings placed on ferromagnetic thin films. We focus on the impact of certain grating parameters, such as the edge-to-edge spacing, on the collective properties of the nanograting, in particular their applicability for chiral pumping when placed on a ferromagnetic thin film.
In Chapter 2, we start with a discussion of the theoretical background needed for the interpretation of the obtained results. Concretely, we introduce the macrospin model for ferromagnetic materials, allowing us to describe phenomena such as ferromagnetic resonance and the propagation of spin waves. Afterwards, the chapter ends with a discussion of unidirectional spin waves, including a formal description of the chiral pumping effect.
Based on the theoretical background, Chapter 3 then explores the methodology of micromagnetic simulations, starting off with a general overview of the field. We follow this by detailing the specifics of conducting micromagnetic simulations using the software MuMax^3. Thereby, we highlight the impact of the different input parameters, before we verify the simulations by comparing them to known analytical results. Lastly, we discuss the numerous algorithms for post-

processing conceptualized and written in the scope of this work.
After establishing an understanding of the simulation process, we then turn towards discussing the simulation results for isolated, ferromagnetic nanogratings in Chapter 4, where we inspect the ferromagnetic resonance (FMR) response of gratings with different inter-wire spacings in detail. This allows us to gain insight into the influence of the sparsity of the grating onto its collective Kittel mode, which directly influences its applicability to chiral pumping. Furthermore, we study their spin wave transport properties by analyzing their dispersion relation. Besides these homogeneous gratings, composed of wires of constant widths, we shift towards the study of arrays of nanowires with alternating widths in adjacent wires in Chapter 5. There, we again focus on the collective FMR response, leading to the proposal of a potential new device type.
Finally, we investigate the properties of combined stacks of homogeneous, ferromagnetic nanogratings and low magnetic damping thin films in Chapter 6. Specifically, we focus on the question of whether a finite non-reciprocity is to be expected in experiments according to the simulation. To this end, we compare the FMR response of such a nanograting/thin film stack to that of an isolated grating. Lastly, we discuss potential non-reciprocities in the spin wave dispersion.
To close this thesis, Chapter 7 summarizes all results presented in this work, before highlighting potential starting points for further research.

Chapter 2

Theory

This chapter aims to introduce the necessary theoretical concepts to understand and describe the physical phenomena investigated in the scope of this thesis. Conceptually, it will follow the idea of starting with the simplest models possible and extending them piece by piece, highlighting the influence of the additional interactions. After briefly introducing the definition of ferromagnets in Sec. 2.1, a simple macrospin model is derived in Sec. 2.2, including both static magnetic properties and the Landau-Lifshitz-Gilbert equation as a description of the magnetic system dynamics. This simple model is extended by adding oscillating, microwave driving fields in Sec. 2.3, discussing ferromagnetic resonance. Moving away from ground-state behaviors, the collective excitations of ferromagnets, spin waves, are presented in Sec. 2.4 and described in the formalism of previous chapters. Lastly, mechanisms responsible for unidirectional propagation of spin waves are explored in Sec. 2.5, specifically focusing on magnetostatic surface spin waves in Sec. 2.5.1 and chiral pumping in magnetic heterostructures in Sec. 2.5.2.

2.1 Ferromagnetic solids

Ferromagnetic materials exhibit a long-range ordered phase of their spin structure, characterized by a spontaneous net magnetization $\boldsymbol{M}$ in absence of external magnetic fields $\boldsymbol{H}$. This is due to permanent, microscopic magnetic moments $\boldsymbol{\mu}_i$ interacting mutually via exchange interaction, favoring a collinear alignment in a single-domain ferromagnet with volume V [12]. Their collective orientation gives rise to a macroscopically detectable quantity, the magnetization $\boldsymbol{M}$, which is defined as [12]

$$\boldsymbol{M} = \frac{1}{V} \sum_{\boldsymbol{\mu}_i \in V} \boldsymbol{\mu}_i = M_\mathrm{s} \boldsymbol{m}. \tag{2.1}$$

In the context of this thesis mainly the orientation of $\boldsymbol{M}$ is discussed, therefore it is convenient to express the magnetization via the saturation magnetization M_s,

which corresponds to the magnitude of the magnetization of a fully polarized sample, and the unit vector of the magnetization direction $\boldsymbol{m} = \boldsymbol{M}/M_\mathrm{s}$. Using the magnetization to model a ferromagnet instead of explicitly modeling the quantum many-body system of the interacting electrons with spin $\boldsymbol{S}$ is valid in this context due to the large number of electrons typically contained in a ferromagnetic solids volume ($\approx 10^{28}\,\mathrm{m}^{-3}$), making an exact quantum mechanical approach non-feasible [13].
Alternatively to Eq. (2.1), the magnetization can also be expressed via the linear response of a material to a magnetic field $\boldsymbol{H}$ as described by the magnetic susceptibility $\hat{\boldsymbol{\chi}}$ [14]:

$$\boldsymbol{M} = \hat{\boldsymbol{\chi}}\boldsymbol{H}, \tag{2.2}$$

where $\hat{\boldsymbol{\chi}}$ is a dimensionless tensor. Considering a case where χ is a scalar quantity, ferromagnetic materials are classified by $\chi \approx 10 - 10^7 \gg 1$, signifying a strong magnetization even in the absence of an external magnetic field [15]. Note that Eq. (2.2) is an approximation for small fields in the regime of linear response, whereas for arbitrary fields a differential definition applies ($\hat{\boldsymbol{\chi}} = \mathrm{d}\boldsymbol{M}/\mathrm{d}\boldsymbol{H}$) [16].

2.2 Macrospin model of a ferromagnetic solid

Since the magnetization is defined as the sum of magnetic moments in Eq. (2.1), it becomes evident that the dynamics of a (fully polarized) ferromagnet may be described by the motion of a single magnetic dipole moment of macroscopic magnitude, coining the term *macrospin model*.
A general magnetic (dipole) moment $\boldsymbol{\mu}$ can be expressed via the total angular momentum vector $\boldsymbol{J}$, e.g., of the corresponding atom, as

$$\boldsymbol{\mu} = -g\mu_\mathrm{B}\frac{\boldsymbol{J}}{\hbar} = -\gamma\boldsymbol{J}, \tag{2.3}$$

where g is Landé-factor, μ_B the Bohr magneton and $\hbar$ the reduced plank constant, often combined into the gyromagnetic ratio $\gamma = g\mu_\mathrm{B}/\hbar$ [12]. A magnetic field $\boldsymbol{H}$ will exert a torque $\boldsymbol{T}$ on the dipole, which is given as [15]

$$\boldsymbol{T} = \frac{\mathrm{d}\boldsymbol{J}}{\mathrm{d}t} = \boldsymbol{\mu} \times \mu_0\boldsymbol{H}, \tag{2.4}$$

where $\mu_0 \approx 4\pi \times 10^{-7}\,\mathrm{Vs/Am}$ is the magnetic vacuum permeability.
As the magnetization $\boldsymbol{M}$ is defined as the sum over the internal magnetic moments of the ferromagnet (c.f. Eq. (2.1)), it shows analogue behavior to that of a simple magnetic moment. Assuming all internal magnetic moments $\boldsymbol{\mu}_i$ to be of equivalent magnitude, the summation in Eq. (2.1) can be expressed via a factor

N, denoting the number of magnetic moments in the ferromagnet, and the relation between a magnetic moment and the total associated angular momentum in Eq. (2.3), finally reading [12, 13]

$$\boldsymbol{M} = \frac{N}{V}\boldsymbol{\mu} = -\gamma\frac{1}{V}\boldsymbol{J}. \tag{2.5}$$

2.2.1 Effective field

In the effort of modeling a ferromagnet, apart from externally applied magnetic fields $\boldsymbol{H}_{\text{ext}}$, internal magnetic field contributions have to be taken into account, giving rise to the effective magnetic field

$$\mu_0\boldsymbol{H}_{\text{eff}} = -\left(\frac{\partial}{\partial m_x}, \frac{\partial}{\partial m_y}, \frac{\partial}{\partial m_z}\right)^T F_m = -\nabla_m F_m, \tag{2.6}$$

where F_m is the free energy density of the ferromagnet [13, 17]. Several contributions to the free energy landscape have to be considered to calculate an accurate equilibrium magnetization orientation. In the following, the contributions considered most important for this work will be laid out.

Zeeman energy The first contribution to the effective field is given by any single or sum of (homogeneous) external fields $\boldsymbol{H}_{\text{ext}}$ the ferromagnet is exposed to. As the strength of external fields is rather easily varied compared to intrinsic material parameters, the *Zeeman*-interaction is essential, as it allows to control the magnetization direction in experiment and simulation. Its contribution to the free energy density is given by the general expression for energy of a magnetic dipole in an external, homogeneous magnetic field [12]:

$$F_{\text{Zee}} = -\mu_0\boldsymbol{M}\cdot\boldsymbol{H}_{\text{ext}}. \tag{2.7}$$

Exchange energy As mentioned in the beginning of this chapter, the single magnetic moments in the ferromagnet interact mutually via the exchange interaction, modeled by a simple Heisenberg Hamiltonian. In the framework of this thesis, we will consider only collinear spin structures and neglect any asymmetric exchange interactions like the Dzyaloshinskii-Moriya interaction [12, 18]. The free energy density for the exchange interaction between a spin $\boldsymbol{S}_i$ and adjacent spins $\boldsymbol{S}_j$ is governed by the magnitude of the exchange integral J_{ij} and assumes the general form [18]

$$F_{\text{ex}} = -\frac{1}{V}\sum_{<i,j>} J_{ij}\boldsymbol{S}_i\cdot\boldsymbol{S}_j, \tag{2.8}$$

where the summation is over pairs of nearest neighbors $<i,j>$ as a reasonable simplification. It is useful to note that the sign of J_{ij} governs the type of coupling between neighboring spins, $J_{ij} < 0$ signifies antiferromagnetic coupling favoring opposing orientation of adjacent spins, whereas $J_{ij} > 0$ causes ferromagnetic coupling with parallel alignment. This general expression can be written in terms of the magnetization using some simplifications, namely assuming equal coupling between all nearest neighbors ($J_{ij} = J$), equal magnitude of spins/magnetic moments ($S_i = S_j = S$) and expressing the scalar product in Eq. (2.8) via a taylor-expanded cosine (assuming small angles θ_{ij} between the spins), simplifying Eq. (2.8) to [13, 18]

$$F_{\mathrm{ex}} = -\frac{JS^2}{V} \sum_{<i,j>} \cos\theta_{ij} \approx -\frac{JS^2 N_{\mathrm{n.n.}}}{V} + \frac{JS^2}{2V} \sum_{<i,j>} \theta_{ij}^2. \tag{2.9}$$

In Eq. (2.9), $N_{\mathrm{n.n.}}$ is the number of nearest neighbors in the respective lattice geometry. To get a final expression in terms of the magnetization of a ferromagnet, the angle between neighboring moments can be expressed via the gradient of the magnetization. Further omitting the constant terms, the final contribution of the exchange energy to the total free energy density reads [18]

$$F_{\mathrm{ex}} = \frac{JS^2 a^2 N_{\mathrm{n.n.}}}{2V} \left(\frac{\nabla \boldsymbol{M}}{M_{\mathrm{s}}} \right)^2 = A_{\mathrm{ex}} (\nabla \boldsymbol{m})^2, \tag{2.10}$$

where a is the lattice constant of the considered system, absorbed into the *exchange stiffness* $A_{\mathrm{ex}} = JS^2 a^2 N_{\mathrm{n.n.}}/(2V)$. A_{ex} is an important material parameter, especially for spin-wave calculations [13].

Shape anisotropy When considering ferromagnetic materials of finite dimensions, the macroscopic geometry of the ferromagnet also shapes the magnetic field landscape inside the material. This is due to the *demagnetization field* $\boldsymbol{H}_{\mathrm{d}}$, which is oriented opposite to the external field direction and is only present inside the volume of the ferromagnet [12, 17]. Its origin is often explained in the simple picture of fictional "magnetic charges" accumulating on the sample surface, which in turn create an opposing magnetic field of their own. Mathematically, the demagnetization field $\boldsymbol{H}_{\mathrm{d}}$ is connected to the sample magnetization $\boldsymbol{M}$ via the demagnetization tensor $\hat{\mathbf{N}}$ [12]:

$$\boldsymbol{H}_{\mathrm{d}} = -\hat{\mathbf{N}}\boldsymbol{M} \qquad \text{with} \qquad \hat{\mathbf{N}} = \begin{pmatrix} N_{xx} & N_{xy} & N_{xz} \\ N_{yx} & N_{yy} & N_{yz} \\ N_{zx} & N_{zy} & N_{zz} \end{pmatrix}. \tag{2.11}$$

Subsequently, the magnitude of $\boldsymbol{H}_{\mathrm{d}}$ depends on $\hat{\mathbf{N}}$, which in turn is dependent on the macroscopic geometry of the ferromagnetic sample. For ellipsoid-shaped

samples, all non-diagonal elements of $\hat{\mathbf{N}}$ vanish in the coordinate system of the principal axes and one obtains [12]

$$\hat{\mathbf{N}} = \begin{pmatrix} N_{xx} & 0 & 0 \\ 0 & N_{yy} & 0 \\ 0 & 0 & N_{zz} \end{pmatrix} \quad \text{and} \quad N_{xx} + N_{yy} + N_{zz} = 1. \tag{2.12}$$

In this case, the diagonal elements N_{ii} may be calculated as shown in Ref. [19]. The scope of this thesis mainly focuses on two geometries of ferromagnets, both differing from an ellipsoid shape: a planar (infinite) thin film and a rectangular prism/cuboid.

The rather simple edge case of an (infinite) planar thin film can by modeled well by an infinitely extended disk of finite thickness [17]. With this approach, one finds that Eq. (2.12) holds and demagnetization factors in the thin film plane vanish $N_{\text{ip}} = N_{xx} = N_{yy} = 0$, whereas the out-of-plane component satisfies $N_{\text{oop}} = N_{zz} = 1$ [18].

A less general case is that of a rectangular-shaped prism or cuboid. Assuming a homogeneous magnetization in a cuboid centered around the origin of the coordinate system, it was shown that conveniently the ellipsoid properties in Eq. (2.12) still apply [20]. Such a general cuboid, extending over the ranges $-a \leq x \leq a$, $-b \leq y \leq b$ and $-c \leq z \leq c$, is illustrated in Fig. 2.1 (a). The diagonal elements of $\hat{\mathbf{N}}$ can be determined analytically when the dimensions of the prism are known [20]:

$$\begin{aligned} \pi N_{zz}(a,b,c) =& \frac{b^2-c^2}{2bc} \ln\left(\frac{\sqrt{a^2+b^2+c^2}-a}{\sqrt{a^2+b^2+c^2}+a}\right) + \frac{a^2-c^2}{2ac} \ln\left(\frac{\sqrt{a^2+b^2+c^2}-b}{\sqrt{a^2+b^2+c^2}+b}\right) \\ &+ \frac{c}{2a} \ln\left(\frac{\sqrt{b^2+c^2}-b}{\sqrt{b^2+c^2}+b}\right) + \frac{c}{2b} \ln\left(\frac{\sqrt{a^2+c^2}-a}{\sqrt{a^2+c^2}+a}\right) + \frac{a^3+b^3-2c^3}{3abc} \\ &+ 2\arctan\left(\frac{ab}{c\sqrt{a^2+b^2+c^2}}\right) + \frac{a^2+b^2-2c^2}{3abc}\sqrt{a^2+b^2+c^2} \\ &+ \frac{c}{ab}\left(\sqrt{a^2+c^2}+\sqrt{b^2+c^2}\right) \\ &- \frac{(a^2+b^2)^{3/2}+(b^2+c^2)^{3/2}+(c^2+a^2)^{3/2}}{3abc}, \end{aligned} \tag{2.13}$$

where the other two diagonal components are obtained via the cyclic permutation $c \to a \to b \to c$ as [20]

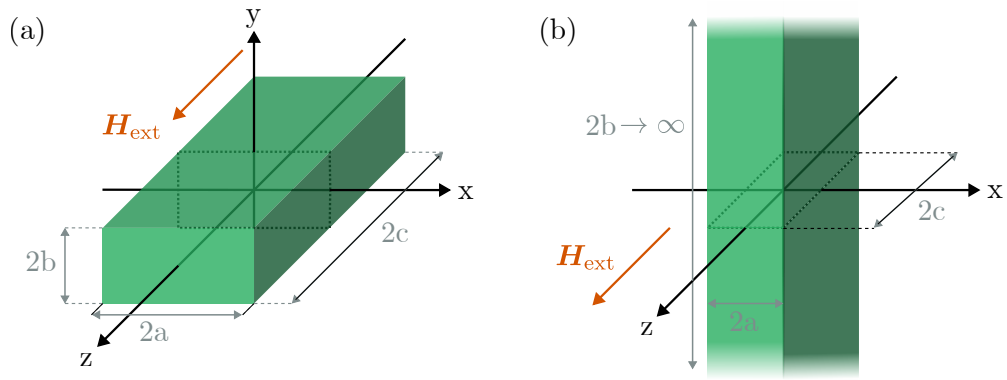

Figure 2.1: Visualization of the rectangular prism centered around the origin of the coordinate system. **(a)** General case of a rectangular prism with dimensions $2a \times 2b \times 2c$ with the external magnetic field $\boldsymbol{H}_{\text{ext}}$ (orange) applied along the z-axis. The diagonal demagnetization tensor elements for this geometry are calculated using Eq. (2.13). **(b)** Edge case of an infinitely long wire ($b \to \infty$) with the external magnetic field $\boldsymbol{H}_{\text{ext}}$ (orange) perpendicular to the wire, where the demagnetization factor N_{zz}^{∞} is described by Eq. (2.15).

$$\pi N_{xx}(a,b,c) = \pi N_{zz}(c,a,b) \quad \text{and} \quad \pi N_{yy}(a,b,c) = \pi N_{zz}(b,c,a). \tag{2.14}$$

In order to visualize Eq. (2.13) and Eq. (2.14) and verify them against the known limit of a planar thin film, Fig. 2.2 (a) shows the demagnetization factors N_{xx}, N_{yy} and N_{zz} for a transition from a rectangular cuboid towards a thin film by fixing the width along the external field direction $c = 1$, while extending the cuboid along the other dimensions $a = b$. For a small extension of the cuboid perpendicular to the external magnetic field, N_{zz} is around zero and N_{xx}/N_{yy} are finite, with their value depending on the exact ratio of a and b. For an (in-plane) extension normal to the field of $a/c \approx 100$, the limit of the previously discussed thin film edge case is reasonably met by both Eq. (2.14) with $N_{xx} = N_{yy} = N_{\text{ip}} = 0$ and Eq. (2.13) with $N_{zz} = N_{\text{oop}} = 1$.
In order to get the demagnetization factors for an infinitely long wire with the external magnetic field applied perpendicular to the wire direction one takes the limit $b \to \infty$ in Eq. (2.13). This geometry is depicted schematically in Fig. 2.1 (b). The simplified expression for this case, using the dimensionless parameter $p = c/a$, is given by [20, 21]

$$\pi N_{zz}^{\infty}(p) = \frac{1-p^2}{2p}\ln(1+p^2) + p\ln p + 2\arctan\left(\frac{1}{p}\right). \tag{2.15}$$

In Fig. 2.2 (b), the special case of the transition from a rectangular prism towards an infinite wire is shown by increasing b while keeping $a = c = 1$ fixed. For this

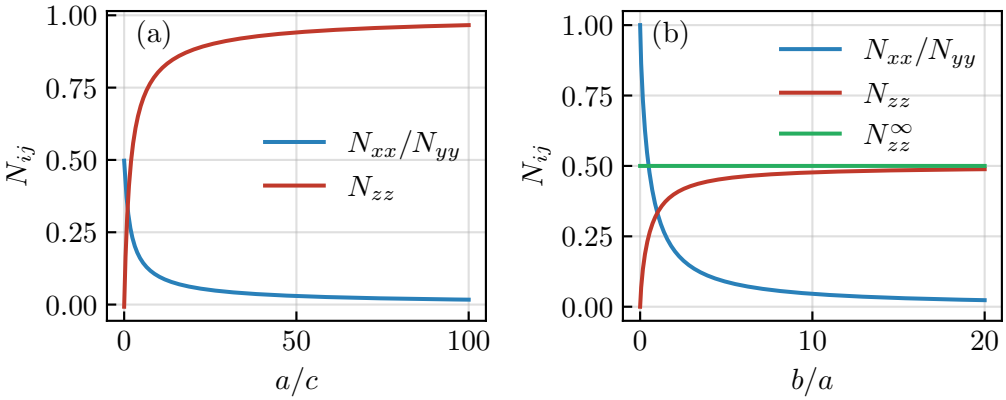

Figure 2.2: Analytical forms of the demagnetization factors N_{xx}, N_{yy} and N_{zz} for rectangular prisms according to Eq. (2.13) for different dimensions. **(a)** Transition of a rectangular prism towards an extended thin film by simultaneously increasing $a = b$ while fixing the length along the external field direction ($c = 1$). N_{xx}/N_{yy} starts from a finite value depending on the ratio of a and b, whereas N_{zz} increases from 0 for small $a = b$. At an in-plane extension of $a/c \approx 100$ compared to the thickness c, the demagnetization factors are in reasonable proximity to the thin film limit, i.e., $N_{zz} = N_{\mathrm{oop}} = 1$ and $N_{xx} = N_{yy} = N_{\mathrm{ip}} = 0$. **(b)** Transition from a rectangular prism to an infinitely long wire by increasing the length b perpendicular to the external magnetic field direction, whereas $a = c = 1$ stays fixed (c.f. Fig. 2.1 (b)). For additional reference, the analytical limit for $b \to \infty$ of Eq. 2.13, denoted N_{zz}^{∞} (c.f. Eq. (2.15)), is shown. It can be seen that the two expressions N_{zz} and N_{zz}^{∞} are in reasonable agreement for an extension $b/a \approx 20$ perpendicular to the external magnetic field direction.

case, N_{zz} is zero and N_{xx}/N_{yy} is finite for vanishing b, depending on the ratio of a and c (similar to Fig. 2.2 (a)). For a value of $b = 20a$, the analytical expression Eq. (2.13) already matches sufficiently well with the expression for the limit of the infinitely long wire N_{zz}^{∞} as described by Eq. (2.15).

All in all, the effective field landscape derives from the sum of all internal and external magnetic fields acting on the magnet. In the scope of this thesis, the contributions of the Zeeman-energy alongside the shape anisotropy are deemed most important, whereas the contribution of the exchange field will be neglected going forward for didactic purposes, under the assumption of a homogeneously magnetized sample with collinear neighboring magnetic moments. Thus, the total effective field reads

$$\boldsymbol{H}_{\mathrm{eff}} = \boldsymbol{H}_{\mathrm{ext}} + \boldsymbol{H}_{\mathrm{d}} = \boldsymbol{H}_{\mathrm{ext}} - \hat{\mathbf{N}}\boldsymbol{M}. \tag{2.16}$$

2.2.2 Landau-Lifshitz-Gilbert equation

In case of a fully saturated magnet, the orientation of the magnetization in energetic equilibrium can be determined by minimizing the free energy density F_m, meaning the magnetization will be aligned with the direction of the effective magnetic field $\boldsymbol{H}_{\text{eff}}$ in Eq. (2.6) [22].
Driving the magnetization now out of thermal equilibrium leads to a finite angle between the orientation of the magnetization $\boldsymbol{M}$ and the effective magnetic field $\boldsymbol{H}_{\text{eff}}$, thus the effective magnetic field $\boldsymbol{H}_{\text{eff}}$ will exert a torque on the magnetic moment akin to Eq. (2.4) due to the definition of torque as the rate of change of angular momentum. Combined with Eq. (2.5), this results in the equation of motion for the magnetization in case of no loss-channels for energy dissipation, called the *Landau-Lifshitz-equation* [23]:

$$\frac{\mathrm{d}\boldsymbol{M}}{\mathrm{dt}} = -\gamma \boldsymbol{M} \times \mu_0 \boldsymbol{H}_{\text{eff}}. \tag{2.17}$$

Physically, it describes the precession of the magnetization $\boldsymbol{M}$ around the effective magnetic field $\boldsymbol{H}_{\text{eff}}$ for all times at a fixed opening angle θ between $\boldsymbol{M}$ and $\boldsymbol{H}_{\text{eff}}$ and a precession frequency linearly dependent on the magnitude of the effective field, $\omega_{\text{LL}} = \gamma\mu_0|\boldsymbol{H}_{\text{eff}}|$ [14], as shown exemplarily in Fig. 2.3 (a).
However, in a real system, a relaxation towards the direction of the effective field is observed due to the presence of so far neglected energy dissipation mechanisms, such as e.g., eddy currents or magnon-phonon scattering [24]. Without venturing into the physical description of these loss channels, their combined effect can be modeled well by introducing a phenomenological damping term into Eq. (2.17), which is controlled by a material-dependent Gilbert damping parameter α and results in the *Landau-Lifshitz-Gilbert-equation* (LLG) [25]:

$$\frac{\mathrm{d}\boldsymbol{M}}{\mathrm{dt}} = -\gamma \boldsymbol{M} \times \mu_0 \boldsymbol{H}_{\text{eff}} + \frac{\alpha}{M_s} \boldsymbol{M} \times \frac{\mathrm{d}\boldsymbol{M}}{\mathrm{dt}}. \tag{2.18}$$

In a physical picture, Eq. (2.18) describes the relaxation of the magnetization $\boldsymbol{M}$ towards the direction of the effective field $\boldsymbol{H}_{\text{eff}}$ following a spiral trajectory due to the finite Gilbert damping parameter α, as illustrated in Fig. 2.3 (b). In analogy to classical mechanics Eq. (2.18) thus describes a damped harmonic oscillator as the equation of motion for the magnetization in presence of either no or static external magnetic field [13].

2.3 Ferromagnetic resonance

As established in Sec. 2.2, in presence of only static external magnetic fields the dynamics of a small, homogeneously magnetized ferromagnet are well modeled

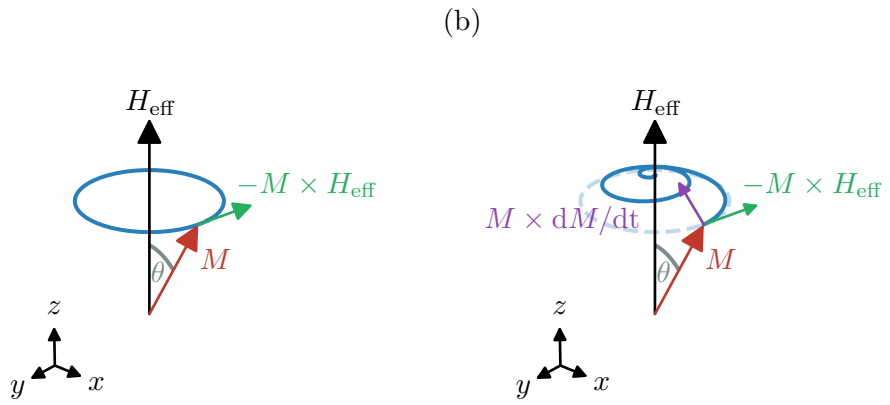

Figure 2.3: Exemplary visualization of the magnetization trajectory as described by the Landau-Lifshitz-Gilbert Equation (2.18) for the cases with and without finite Gilbert damping α. **(a)** $\alpha = 0$: No Gilbert damping leads to continuous precession of the magnetization $\boldsymbol{M}$ around the effective field $\boldsymbol{H}_{\text{eff}}$ at a fixed opening angle θ. **(b)** $\alpha \neq 0$: With Gilbert damping, the magnetization $\boldsymbol{M}$ eventually relaxes into energetic equilibrium at $\boldsymbol{M} \parallel \boldsymbol{H}_{\text{eff}}$, following a spiral-like trajectory.

by a damped harmonic oscillator given by Eq. (2.18). Building on the analogy of the harmonic oscillator, an external, oscillating driving field $\boldsymbol{h}_{\text{rf}}$ shall now be considered on top of any applied static magnetic fields. This driving field $\boldsymbol{h}_{\text{rf}}$ exerts an additional torque on the magnetization $\boldsymbol{M}$ of the shape $-\gamma \boldsymbol{M} \times \mu_0 \boldsymbol{h}_{\text{rf}}$ (c.f. Eq. (2.18)). Upon correct orientation of $\boldsymbol{h}_{\text{rf}}$, this additional torque can counteract the damping torque in the second term in the Landau-Lifshitz-Gilbert-equation (2.18), as shown in Fig. 2.4 (a). Thereby, a resonance effect is expected if the driving frequency matches the precession frequency ω_{LL} [17].
To describe this resonant behavior mathematically, the systems response function, the magnetic susceptibility $\hat{\boldsymbol{\chi}}$ as introduced in Sec. 2.1, will be derived. In the following, it is assumed that the effective magnetic field is oriented along the z-axis ($\boldsymbol{H}_{\text{eff}} \parallel \boldsymbol{z}$) and the driving field lies in the x-y-plane ($\boldsymbol{h}_{\text{rf}} \perp \boldsymbol{z}$), as schematically visualized in Fig. 2.4 (a). Furthermore, the demagnetization tensor $\hat{\mathbf{N}}$ of the ferromagnetic sample fulfills the properties of vanishing non-diagonal elements of a general ellipsoid as shown in Eq. (2.12). This is also valid for general rectangular prisms in the exact solution, as established in Sec. 2.2.1 [20]. Adding the oscillatory driving field $\boldsymbol{h}_{\text{rf}}(t)$ to Eq. (2.16), the total effective field is

$$\begin{aligned}\boldsymbol{H}_{\text{eff}}^{\text{tot}} &= \boldsymbol{H}_{\text{ext}} - \hat{\mathbf{N}}\boldsymbol{M} + \boldsymbol{h}_{\text{rf}}(t) = \begin{pmatrix} -N_{xx}M_x(t) \\ -N_{yy}M_y(t) \\ H_{\text{ext}} - N_{zz}M_z \end{pmatrix} + \begin{pmatrix} h_{\text{rf},x}(t) \\ h_{\text{rf},y}(t) \\ 0 \end{pmatrix} = \\ &= \boldsymbol{H}_{\text{eff}} + \boldsymbol{H}'_{\text{eff}}(t),\end{aligned} \tag{2.19}$$

where in this context $\boldsymbol{H}_{\text{eff}}$ denotes the static and $\boldsymbol{H}'_{\text{eff}}(t)$ the time-dependent contribution to $\boldsymbol{H}_{\text{eff}}^{\text{tot}}$. In general, the driving field $\boldsymbol{h}_{\text{rf}}(t)$ causes a time dependent magnetization $\boldsymbol{M}(t)$. As a simplification, the magnetization is assumed to have a fixed magnitude ($|\boldsymbol{M}| = M_s$) and to only be slightly perturbed out of the equilibrium direction ($M_{x/y} \ll M_z$, θ small), which is reasonable for a driving field much weaker than the static effective field ($|\boldsymbol{h}_{\text{rf}}| \ll |\boldsymbol{H}_{\text{eff}}|$) [13, 17]. Furthermore, the contribution of the exchange interaction to the effective magnetic field can be omitted due to the internal magnetic moments staying aligned for weak perturbations [26]. Note that these simplifications are already taken into account in Eq. (2.19).
The magnetization $\boldsymbol{M}(t)$ can now be divided into a constant and a time-dependent part:

$$\boldsymbol{M}(t) = \boldsymbol{M}_0 + \boldsymbol{M}_{\text{rf}}(t) = \begin{pmatrix} 0 \\ 0 \\ M_s \end{pmatrix} + \begin{pmatrix} M_{\text{rf},x}(t) \\ M_{\text{rf},y}(t) \\ 0 \end{pmatrix}. \tag{2.20}$$

In the linear response regime, a plane-wave ansatz for the dynamic magnetization $M_{\text{rf},x/y}(t)$ and the driving field $h_{\text{rf},x/y}(t)$ is used to solve the differential equation [27]:

$$\begin{aligned}\boldsymbol{h}_{\text{rf}}(t) &= \begin{pmatrix} h_{\text{rf},x} & h_{\text{rf},y} & 0 \end{pmatrix}^{\text{T}} \cdot \mathrm{e}^{i\omega t} \\ \boldsymbol{M}_{\text{rf}}(t) &= \begin{pmatrix} M_{\text{rf},x} & M_{\text{rf},y} & 0 \end{pmatrix}^{\text{T}} \cdot \mathrm{e}^{i\omega t}.\end{aligned} \tag{2.21}$$

Solving now the LLG (c.f. Eq. (2.18)) for this system as described by Eqs. (2.19), (2.20) and (2.21) results in a set of differential equations for the x- and y-component of the magnetization $\boldsymbol{M}$, which can be expressed in matrix form via the *Polder-susceptibility* $\hat{\boldsymbol{\chi}}_{\text{P}}$ [26]:

$$\begin{pmatrix} h_{\text{rf},x} \\ h_{\text{rf},y} \end{pmatrix} = \hat{\boldsymbol{\chi}}_{\text{P}}^{-1} \begin{pmatrix} M_{\text{rf},x} \\ M_{\text{rf},y} \end{pmatrix} \tag{2.22}$$

with

$$\hat{\boldsymbol{\chi}}_{\text{P}}^{-1} = \frac{1}{M_s} \begin{pmatrix} H_{\text{ext}} + (N_{xx} - N_{zz})M_s + \frac{i\omega\alpha}{\gamma\mu_0} & -\frac{i\omega}{\gamma\mu_0} \\ +\frac{i\omega}{\gamma\mu_0} & H_{\text{ext}} + (N_{yy} - N_{zz})M_s + \frac{i\omega\alpha}{\gamma\mu_0} \end{pmatrix}. \tag{2.23}$$

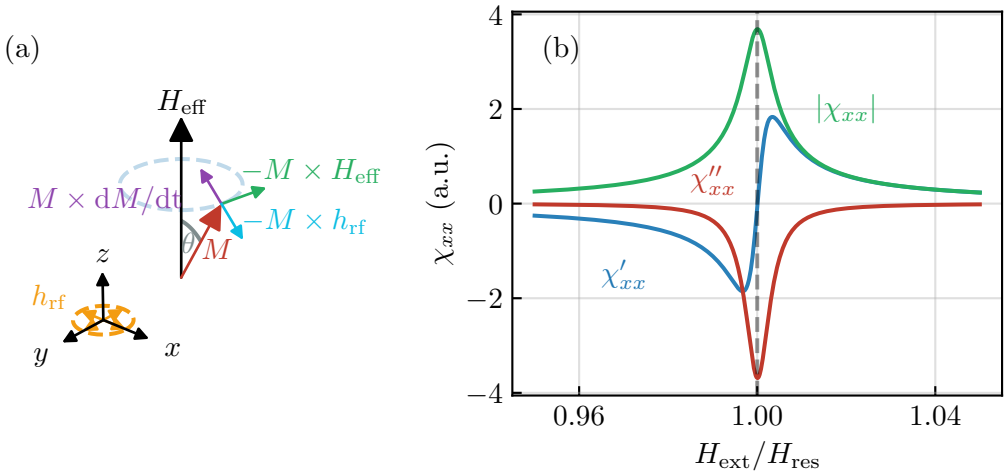

Figure 2.4: (a) Exemplary coordinate system visualizing the mutual orientation of the different torque terms in the context of a ferromagnetic resonance experiment. Upon correct orientation of the driving microwave field $\boldsymbol{h}_{\mathrm{rf}}$ (orange), the resulting torque $-\boldsymbol{M} \times \boldsymbol{h}_{\mathrm{rf}}$ (cyan) is able to compensate the damping torque $\boldsymbol{M} \times \mathrm{d}\boldsymbol{M}/\mathrm{dt}$ (purple), leading to resonant absorption of the microwave energy and consequent opening of the precession cone with a finite angle θ. **(b)** Visualization of the Polder susceptibility $\hat{\boldsymbol{\chi}}_{\mathrm{P}}$ (c.f. Eq. (2.24)) for the exemplary case of a permalloy thin film ($N_{xx} = N_{yy} = 0$, $N_{zz} = 1$) with material parameters $f = \omega/2\pi = 10\,\mathrm{GHz}$, $\mu_0 M_{\mathrm{s}} = 1\,\mathrm{T}$ and $\alpha = 0.006$ (parameters taken from Ref. [17]). Upon varying the static external field H_{ext} around the resonance field H_{res} the distinctive line shapes of the individual components of $\chi_{xx} = \chi'_{xx} + i\chi''_{xx}$ can be observed. The real part χ'_{xx} (blue) describes the dispersive system response and has an anti-symmetric Lorentzian line shape around the resonance field. The dissipative imaginary part χ''_{xx} (red) is characterized by a symmetric Lorentzian line shape signifying the absorption of the microwave power at H_{res}. Additionally, the absolute magnitude of the Polder susceptibility, $|\chi_{xx}|$, is shown (green).

The Polder susceptibility $\hat{\boldsymbol{\chi}}_{\mathrm{P}}$ describes the linear response of $\boldsymbol{M}_{\mathrm{rf}}(t)$ to a weak external perturbation field $\boldsymbol{h}_{\mathrm{rf}}(t)$, and is given as [13, 26]

$$\hat{\boldsymbol{\chi}}_{\mathrm{P}} = \frac{1}{M_s A} \begin{pmatrix} H_{\mathrm{ext}} + (N_{yy} - N_{zz})M_s + \frac{i\omega\alpha}{\gamma\mu_0} & +\frac{i\omega}{\gamma\mu_0} \\ -\frac{i\omega}{\gamma\mu_0} & H_{\mathrm{ext}} + (N_{xx} - N_{zz})M_s + \frac{i\omega\alpha}{\gamma\mu_0} \end{pmatrix}, \tag{2.24}$$

where $A = \det\left(\hat{\boldsymbol{\chi}}_{\mathrm{P}}^{-1}\right)$. Since $\hat{\boldsymbol{\chi}}_{\mathrm{P}}$ is complex valued, it can be decomposed as $\hat{\boldsymbol{\chi}}_{\mathrm{P}} = \boldsymbol{\chi}' + i\boldsymbol{\chi}''$, where the real part $\boldsymbol{\chi}'$ describes the dispersive and the imaginary part $\boldsymbol{\chi}''$ the dissipative response of the system to the external probe $\boldsymbol{h}_{\mathrm{rf}}$ [28]. Both $\boldsymbol{\chi}'$ and $\boldsymbol{\chi}''$ possess a characteristic line-shape. In Fig. 2.4 (b), χ'_{xx} and χ''_{xx} are shown for an exemplary case of a thin film ($N_{xx} = N_{yy} = 0$, $N_{zz} = 1$) with typical parameters ($f = \omega/2\pi = 10\,\mathrm{GHz}$, $\mu_0 M_s = 1\,\mathrm{T}$ and $\alpha = 0.006$ for permal-

loy ($Ni_{80}Fe_{20}$) [17]. The dissipative part χ''_{xx} displays a distinctly Lorentzian line-shape and the dispersive part χ'_{xx} shows an anti-symmetric double-peak. Additionally, Fig. 2.4 (b) shows the absolute magnitude $|\chi_{xx}|$.
The system of equations derived for describing ferromagnetic resonance in Eq. (2.22) only has a non-trivial solution if the condition $\det(\boldsymbol{\chi}_{\mathrm{P}}) = 0$ is met. The resulting equation can then be solved for either the resonance frequency ω_{res} or the resonance field H_{res}. Solving for $\omega_{\mathbf{res}}$ and omitting the imaginary part of the solution gives rise to the famous *Kittel equation* [27]:

$$f_{\mathrm{res}} = \frac{\omega_{\mathrm{res}}}{2\pi} = \frac{\gamma\mu_0}{2\pi}\sqrt{[H_{\mathrm{ext}} + (N_{xx} - N_{zz})M_{\mathrm{s}}] \cdot [H_{\mathrm{ext}} + (N_{yy} - N_{zz})M_{\mathrm{s}}]}. \quad (2.25)$$

To close this discussion of ferromagnetic resonance, it is worth emphasizing that the resonant mode as described by Eq. (2.25) corresponds to a uniform, in-phase precession of all magnetic moments in the ferromagnetic material, as the derivation of the system according to Eq. (2.22) was based on a fully saturated sample, where all magnetic moments align and add up according to Eq. (2.1). Subsequently, the ferromagnetic resonance mode satisfies $k = \frac{2\pi}{\lambda} \to 0$ (infinite wavelength λ) as explained in Sec. 2.4, due to the non-existing phase difference of neighboring spins [29].

2.4 Spin waves in ferromagnetic solids

So far, only fully saturated ferromagnets with all interal magnetic moments aligned in the same direction were considered as a simple model for ferromagnetic materials. Upon ignoring thermal effects, this approximation is valid as the fully aligned state is the energetic ground state of a ferromagnetic system [16]. At finite temperatures, this perfect order is, however, disrupted by fluctuations of the spin system known as *spin waves*, which share many similarities with the vibrations of a crystal lattice, as both arise from the fundamental concept of symmetry breaking [16, 30]. An important property shared between lattice vibrations (phonons) and spin waves is quantization [12, 30]. Here, the quanta of spin waves are called *magnons* [12, 30]. In a more semi-classical picture, spin waves can be derived in the picture of a single magnetic moment in the material being flipped into anti-parallel alignment with its neighbors, which comes at an energetic price due to the exchange-interaction (c.f. Eq. (2.8)). This excitation can alternatively be distributed over the entire lattice by tilting all magnetic moments slightly out of the equilibrium position, leading to a collective excitation - the spin wave [12]. As established previously, the magnetic magnetic moments will precess around the equilibrium direction along the effective magnetic field as described by Eq. (2.18). This precessional motion does not necessarily need

adjacent moments to be in phase, but also allows a finite phase shift between neighboring magnetic moments, making it possible to define a wavelength λ and a corresponding wave number k via the wave vector $\boldsymbol{k}$: $k = |\boldsymbol{k}| = 2\pi/\lambda$ [17]. This definition is illustrated schematically in Fig. 2.5 (b), where the wavelength λ of a spin wave is defined as the real space interval over which the phase shift between neighboring magnetic moments $\boldsymbol{\mu}_i$ accumulates to 2π. Importantly, spin waves with finite k have been shown to carry information via their angular momentum, making them interesting for applications in magnon-based computing [31, 32].
Subsequently, ferromagnetic resonance as discussed in Sec. 2.3 describes a spin wave of infinite wavelength $\lambda \to \infty$ and zero momentum $k = 0$ due to all magnetic moments precessing in phase, and thus carries no information [29, 33]. This is shown in Fig. 2.5 (a) upon comparison to a finite k spin wave in Fig. 2.5 (b).
In general, the two interactions responsible for the propagation of spin waves are the short-range exchange-interaction and the long-range dipole-interaction between the magnetic moments. This allows to differentiate two edge cases: spin waves with large k (short λ) are dominated by the contribution of the exchange-interaction to the effective field (c.f. Eq. (2.9)) and are thus referred to as *exchange modes*. For small k (large λ) on the other hand the contribution of the dipole-interaction (stray fields caused by e.g., the shape anisotropy) dominate the effective field, subsequently they are named *dipole modes* [12]. An important parameter to quantify the relative strength of exchange- and dipole-energies is the exchange length [34]

$$l_{\mathrm{ex}} = \sqrt{\frac{2A_{\mathrm{ex}}}{(\mu_0 M_{\mathrm{s}})^2}}, \tag{2.26}$$

where A_{ex} is the exchange stiffness defined in Eq. (2.10) and M_{s} is the saturation magnetization. The thus purely material parameter dependent l_{ex} allows to differentiate regimes of length scales smaller than l_{ex}, where the exchange interaction dominates, from those at length scales larger than l_{ex}, which in turn are dominated by the dipole/magnetostatic-interactions [13]. Spin waves that lie in between these edge cases, where both interactions are relevant, are usually referred to as *dipole-exchange-modes*.

In the following, the dispersion relation of spin waves is derived for the well known edge case of an in-plane magnetized magnetic thin film, as no solution exists for arbitrary magnet geometries [13]. Mathematically, the influence of the exchange- and dipole-interaction is taken into account via respective effective magnetic fields acting on the magnetization. The exchange-interaction adds an isotropic field term proportional to the squared wave number k, given as [35]

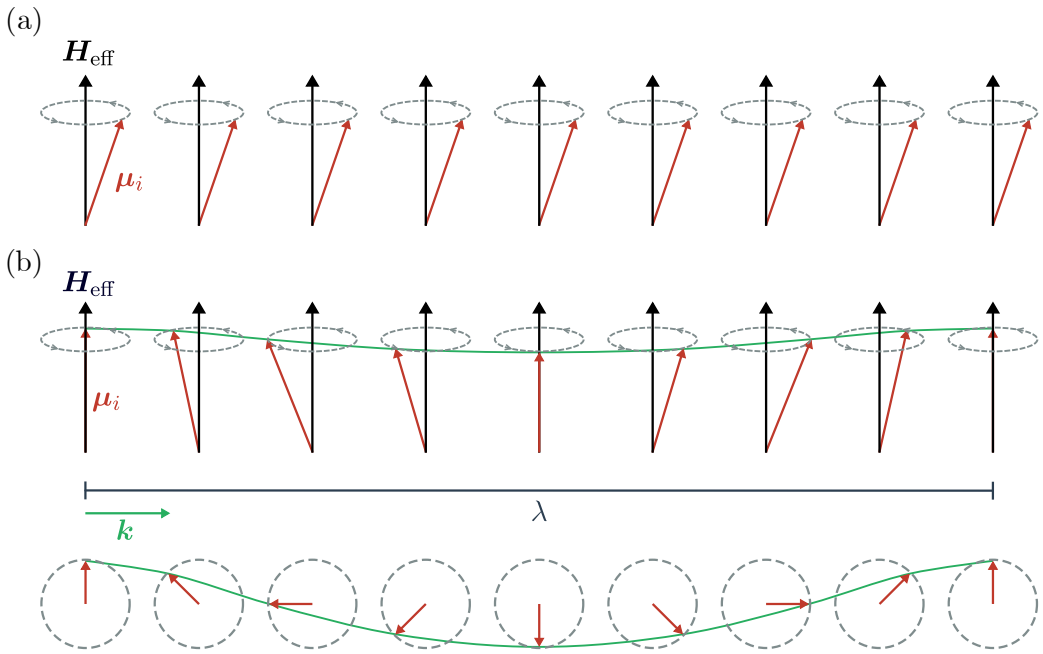

Figure 2.5: Precessional motion of magnetic moments $\boldsymbol{\mu}_i$ (red) around the effective magnetic field $\boldsymbol{H}_{\text{eff}}$ (black). **(a)** Ferromagnetic resonance of all magnetic moments describes a spin wave of infinite wavelength and wave number $k = 0$, as all magnetic moments $\boldsymbol{\mu}_i$ precessing in phase around the effective magnetic field $\boldsymbol{H}_{\text{eff}}$ (c.f. Sec. 2.3). **(b)** Side and top view of a spin wave for $k \neq 0$. The wavelength λ is defined as the interval in real space, in which the accumulative phase difference is 2π.

$$\mu_0 H_{\text{ex}} = \frac{2A_{\text{ex}}}{M_{\text{s}}} k^2. \tag{2.27}$$

It is assumed that the surface normal of the thin-film is oriented along the y-direction and the in-plane magnetization points along the z-direction (see Fig. 2.6). Further assuming the thin film thickness t_{TF} to satisfy $k \cdot t_{\text{TF}} \ll 1$, the dynamic dipole fields were then derived by Kalinikos and Slavin, resulting in [36]

$$\begin{aligned} H_x^{\text{dip}} &= M_{\text{s}} \left(1 - \frac{1 - \mathrm{e}^{-kt_{\text{TF}}}}{kt_{\text{TF}}}\right) \sin^2(\phi) \\ H_y^{\text{dip}} &= M_{\text{s}} \frac{1 - \mathrm{e}^{-kt_{\text{TF}}}}{kt_{\text{TF}}}, \end{aligned} \tag{2.28}$$

where ϕ is the angle between the wave vector $\boldsymbol{k}$ and the magnetization $\boldsymbol{M}$. Using a similar procedure as in Sec. 2.3, the magnetization can be divided into

a static contribution $\boldsymbol{M}_0$ and dynamic contribution $\tilde{\boldsymbol{M}}$, where in contrast to ferromagnetic resonance the plane wave ansatz for the dynamic magnetization now includes finite wave vectors $\boldsymbol{k}$ (i.e., $\mathrm{e}^{i(\omega t-\boldsymbol{kr})}$), leading to [13]

$$\boldsymbol{M} = \begin{pmatrix} 0 \\ 0 \\ M_\mathrm{s} \end{pmatrix} + \begin{pmatrix} \tilde{M}_x \mathrm{e}^{i(\omega t-\boldsymbol{kr})} \\ \tilde{M}_y \mathrm{e}^{i(\omega t-\boldsymbol{kr})} \\ 0 \end{pmatrix} \quad \text{and} \quad \boldsymbol{H}_\mathrm{eff} = \begin{pmatrix} -H_x^\mathrm{dip} \\ -H_y^\mathrm{dip} \\ H_0 + H_\mathrm{ex} \end{pmatrix} + \begin{pmatrix} h_{\mathrm{rf},x}(t) \\ h_{\mathrm{rf},y}(t) \\ 0 \end{pmatrix}. \tag{2.29}$$

In Eq. (2.29), the space vector $\boldsymbol{r} = x\hat{\boldsymbol{e}}_x + z\hat{\boldsymbol{e}}_z$ and the wave vector $\boldsymbol{k} = k_x\hat{\boldsymbol{e}}_x + k_z\hat{\boldsymbol{e}}_z$ are both restricted into the thin film plane, and the external field is now labeled $\boldsymbol{H}_0 = \boldsymbol{H}_\mathrm{ext}$ to avoid confusion with the exchange field in Eq. (2.27). Furthermore, the shape anisotropy field vanishes in the limit of an infinite thin film ($N_{yy} = 1$) with in-plane magnetization ($M_y = 0$), as $\boldsymbol{H}_\mathrm{d} = -\hat{\mathbf{N}}\boldsymbol{M} = -1M_\mathrm{y}\hat{\boldsymbol{e}}_y = 0$. Inserting now the two identities in Eq. (2.29) into the LLG in Eq. (2.18) again gives a system of equations, which can be conveniently be expressed in matrix form $\boldsymbol{h}_\mathrm{rf} = \hat{\boldsymbol{\chi}}^{-1}\tilde{\boldsymbol{M}}$, with the inverse susceptibility given as

$$\hat{\boldsymbol{\chi}}^{-1} = \frac{1}{M_\mathrm{s}} \begin{pmatrix} H_0 + H_\mathrm{ex} + H_\mathrm{x}^\mathrm{dip} + \frac{i\omega\alpha}{\gamma\mu_0} & -\frac{i\omega}{\gamma\mu_0} \\ +\frac{i\omega}{\gamma\mu_0} & H_0 + H_\mathrm{ex} + H_\mathrm{y}^\mathrm{dip} + \frac{i\omega\alpha}{\gamma\mu_0} \end{pmatrix}. \tag{2.30}$$

To receive the resonance frequency for in-plane spin waves in thin films, Eq. (2.30) must have a non-trivial solution and must thus fulfill $\det(\hat{\boldsymbol{\chi}}^{-1}) = 0$. Taking only the real part of the solution into account results in the Kalinikos-Slavin equation [36]

$$f = \frac{\omega}{2\pi} = \frac{\gamma\mu_0}{2\pi}\sqrt{\left(H_0 + H_\mathrm{ex} + H_\mathrm{x}^\mathrm{dip}\right)\left(H_0 + H_\mathrm{ex} + H_\mathrm{y}^\mathrm{dip}\right)}. \tag{2.31}$$

As in Sec. 2.3, the derivation of Eq. (2.31) again assumes ellipsoidal properties of the demagnetization tensor (shown in Eq. (2.12)), which is fulfilled by both thin films and rectangular cuboids [20]. Taking the limit of $k \to 0$ for Eq. (2.31) as a consistency check, the dipole fields reduce to $H_\mathrm{x}^\mathrm{dip} = M_\mathrm{s}$ and $H_\mathrm{y}^\mathrm{dip} = 0$ and the exchange field vanishes, i.e., $H_\mathrm{ex} = 0$, resulting in the expected Kittel equation for an in-plane magnetized thin film $\omega = \gamma\mu_0\sqrt{H_0 \cdot (H_0 + M_\mathrm{s})}$. Considering on the other hand large wave numbers k (short wavelengths λ), the contributions of the dipole fields can be omitted and the dispersion relation becomes quadratic in k: $\omega(k) = \gamma\mu_0(H_0 + H_\mathrm{ex}) \propto k^2$ [13].

Finally, two important cases for the relative orientation of the propagation direction $\boldsymbol{k}$ and the magnetization $\boldsymbol{M}$ as parameterized by the angle ϕ shall be

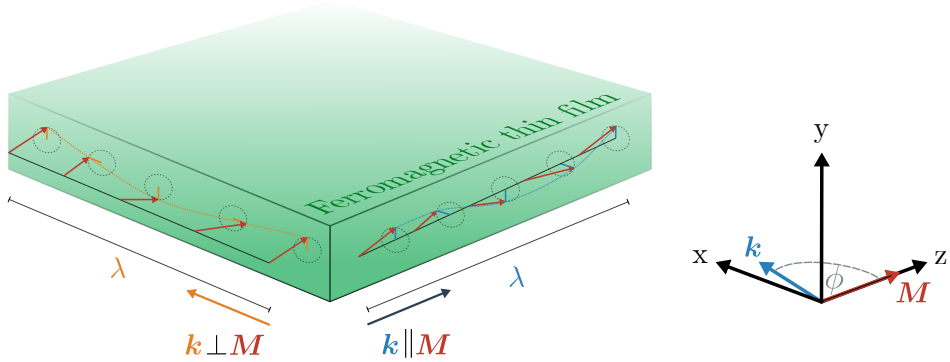

Figure 2.6: Illustration of different in-plane spin wave modes in a ferromagnetic thin film magnetized in the thin film plane. The angle ϕ is used to parameterize the relative orientation between the wave vector (propagation direction) $\boldsymbol{k}$ and the thin film magnetization $\boldsymbol{M}$. The two edge cases of propagation collinear or perpendicular to the magnetization are visualized schematically. The Backward-Volume (BV) mode describes a spin wave propagating along the magnetization direction ($\boldsymbol{k} \parallel \boldsymbol{M}$, $\phi = 0$), which is localized within the volume of the thin film (blue). The Damon-Eshbach (DE) mode on the other hand is characterized by spin wave propagation perpendicular to the magnetization direction ($\boldsymbol{k} \perp \boldsymbol{M}$, $\phi = \pi/2$), and is localized on the top- or bottom surface of the thin film depending on the orientation of the propagation $\pm\boldsymbol{k}$ (orange).

discussed. The first special case is for collinear orientation of $\boldsymbol{k}$ and $\boldsymbol{M}$ ($\boldsymbol{k} \parallel \boldsymbol{M}$, $\phi = 0$). These spin waves are usually referred to as backward volume (BV) modes and are localized within the volume of the thin film, with their naming being derived from their negative group velocity [13]. The second important constellation is wave propagation perpendicular to the magnetization direction ($\boldsymbol{k} \perp \boldsymbol{M}$, $\phi = \pi/2$). Spin wave modes in this geometry are called magneto-static surface (MS) modes or Damon-Eshbach (DE) modes and are localized on the top- or bottom surface of the thin film depending on their propagation direction $\pm\boldsymbol{k}$ [37]. Both Backward-Volume and Damon-Eshbach modes are depicted schematically in Fig. 2.6.

2.5 Unidirectional spin wave propagation

After introducing the concept of spin waves in Sec. 2.4, this section aims to explore different physical mechanisms to induce unidirectional transport properties in real material systems. Unidirectionality or non-reciprocity of spin waves can emerge in different forms, such as different amplitude, frequency or group velocity for counter-propagating spin waves. In the following, we focus on on the unidirectional properties of magneto-static surface spin waves in Sec. 2.5.1,

before discussing the so-called chiral pumping mechanism for the induction of non-reciprocal spin waves in Sec. 2.5.2.

2.5.1 Magneto-static surface spin waves

As mentioned briefly in Sec. 2.4, spin waves in in-plane magnetized thin films propagating perpendicular to the magnetization direction are called Damon-Eshbach (surface) spin waves or magneto-static surface spin waves (MSSWs). They possess the interesting property of counter-propagating spin waves being exponentially localized in their amplitude on opposite surfaces of the thin film, e.g., on the top/bottom surface of the film for the wave vector $\pm\boldsymbol{k}$ as depicted schematically in Fig. 2.7 (a) [7]. This has been shown for the limit of long wavelengths, where the effective field contribution caused by the exchange interaction (c.f. Eq. (2.27)) becomes negligible [38]. Thus considering only the dipole fields leads to a non-reciprocity in the amplitude of the spin wave [38]. Additionally, when considering both dipole- and exchange-interaction (as was done in Sec. 2.5), it has been shown that the addition of the exchange-interaction leads to the fundamental spin wave mode to be localized on the respective opposite surface of the film than in the dipole-only case, however, without disrupting the non-reciprocity (for standard excitation types) [39].
This localization at the thin film surface can be understood by considering a dynamic dipole field generated by the dynamics of the magnetization [40]. Again, the magnetization $\boldsymbol{M}$ is separated into a static contribution $\boldsymbol{M}_0$ and a dynamic contribution $\tilde{\boldsymbol{M}}$, as shown in Eq. (2.29). The spatial distribution of $\tilde{\boldsymbol{M}}$ across the wavelength of a spin wave with wave number $k > 0$ is shown schematically in Fig. 2.7 (b). Both components $\tilde{M}_x$ (red) and $\tilde{M}_y$ (blue) lead to the formation of magnetic poles, which cause a dynamic dipole field of their own. These dipole fields add up in the lower half of the ferromagnetic thin film, whereas in the top half, they are oppositely oriented. Therefore, for $k > 0$, the dipole field is larger in the lower part of the film, whereas for $k < 0$ the situation is reversed. This asymmetry in the dynamic dipole field is now compensated by the dynamic magnetization when building spin wave eigenmodes by increasing its amplitude on the side of the weaker dipole field [40]. This localization can furthermore be switched (e.g., from top to bottom surface for $k < 0$) upon inverting the external field direction [40].

Considering the schematic shown in Fig. 2.7 (a), it is a reasonable thought to increase the thickness t_{TF} of the ferromagnetic film to decrease the overlap between the exponential localizations of the amplitudes, that is to reduce *leakage* of modes onto the opposite localization surface. It has been shown experimentally that for $Y_3Fe_5O_{12}$ (YIG) films with $d = 254\,\mu\mathrm{m}$, unidirectionality of spin waves is in

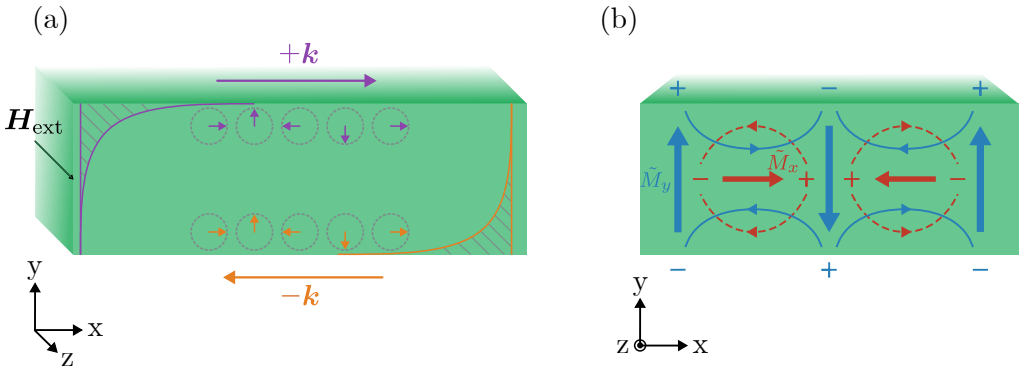

Figure 2.7: Schematic illustrations of magneto-static (Damon-Eshbach) surface spin waves (MSSWs). **(a)** MSSWs are localized on the top or bottom surface of the ferromagnetic thin film medium (green), depending on their propagation direction $\boldsymbol{k}$. The localization to the surface is due to exponential decay of the spin wave amplitude (indicated by the hatched surface), caused by interactions with the dynamic dipole fields. **(b)** Illustration of the dynamic dipole fields $\tilde{M}_x$ (red) and $\tilde{M}_y$ (blue) for a MSSW with a positive wave number $k > 0$. Both dynamic dipole fields create magnetic poles, which in turn create dipole fields of their own. These dipole fields (shown as field lines) then add up in the lower half of the film, but are oppositely oriented in the top half, leading to stronger dipole fields in the lower half. In an effort to form a spin wave eigenmode, the dynamic magnetization tends to compensate the asymmetric dipole field by increasing the amplitude on the respective side with weaker dipole fields. Counter-propagating spin waves $\pm\boldsymbol{k}$ are located on opposite sides of the film, however, the localization can be inverted by inverting the external field direction. Figure (b) is recreated from Ref. [40].

fact achieved on the respective surfaces [41]. However, it has also been found that the unidirectionality decreases for thinner films and is almost completely destroyed (reduced to $\approx 3\%$) due to mode leakage for $Ni_{20}Fe_{80}$ thin films with $t_{TF} = 20\,\text{nm}$ due to mode leakage [41]. Furthermore, it should be noted that the physical mechanism responsible for the unidirectionality of MSSWs is based on the compensation of dynamic dipole fields, and is thus not valid in the regime of very short wavelengths, where the spin waves are dominated by the exchange interaction and dipole fields are negligible (c.f. Sec. 2.4). These limitations are considerable drawbacks in the quest to achieve small magnonic nano-devices, where both material dimensions on the nanometer scale and small wavelengths are desirable [7]. Additionally, MSSWs are known to have small group velocities and are susceptible to dephasing by surface roughness, making them further sub-optimal for application [9].

2.5.2 Unidirectional spin waves via chiral pumping

Besides using the intrinsic properties of a single magnetic material leading to non-reciprocal behavior, as e.g., in Sec. 2.5.1 in terms of magneto-static surface

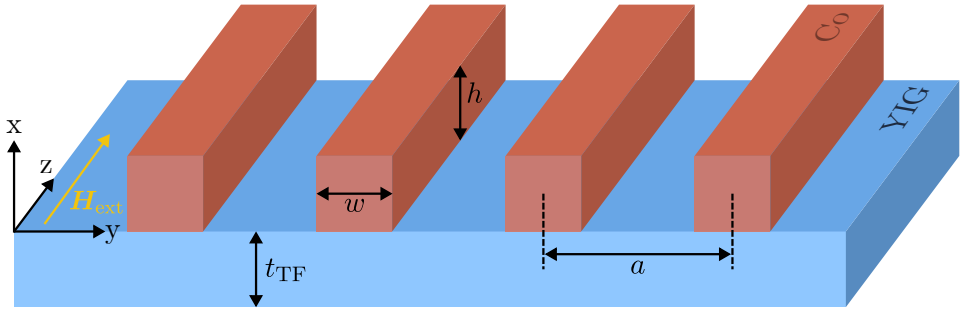

Figure 2.8: Illustration of the system setup for chiral spin wave pumping. The spin wave medium is given by a low-damping, ferromagnetic thin film material (blue), here $Y_3Fe_5O_{12}$ (YIG), oriented such that the y-z-plane describes the film plane and x is surface normal. On top of the thin film is a nanograting (red) made from a ferromagnetic material with high saturation magnetization, here Co. The individual wires consisting the grating have a width w, height h and are spaced a distance a from center-to-center. The thin film is defined by its thickness t_{TF}. A static external field $\boldsymbol{H}_{\text{ext}}$ is applied along the z-axis, orienting the magnetization of both the thin film and the grating along the wire direction.

spin waves, another approach to realize unidirectional spin waves is to combine magnetic materials in such a way that their interaction with each other allows for non-reciprocal behavior. A popular technique is to place a (periodic) array of magnetic nanowires onto a low-damping ferro- or ferri-magnetic thin film, inducing non-reciprocal spin waves by so-called *chiral pumping* [9]. Chiral pumping refers to the generation of unidirectional (exchange-)spin waves in ultra-thin magnetic films with thicknesses of order $\mathcal{O}(10\,\text{nm})$ via the dipole-interaction between the film and the magnetic wires [9]. Physically, this is realized by the Kittel mode of the nanowires coupling chirally to spin waves in the film propagating perpendicular to the wire array (and thus the film magnetization), even though the surface-localized and chiral Damon-Eshbach mode (as discussed in Sec. 2.5.1) does not exist in films of these thicknesses due to large overlaps between the exponential localizations on the film surfaces [8]. In the following, a brief overview over the theoretical background of this coupling is given.
In Fig. 2.8, the general layout of the system is depicted: a nanograting consisting of a periodic array of ferromagnetic wires with high saturation magnetization (usually Ni or Co) is placed on a ferro- or ferri-magnetic thin film with low magnetic damping, in most cases the ferrimagnetic insulator $Y_3Fe_5O_{12}$ (YIG). The individual wires oriented along the z-axis (see Fig. 2.8) have a width w and a height h, and the center-to-center spacing between adjacent wires is denoted

as a. The thin film is characterized by its thickness t_{TF} along the surface normal x of the film. An external field is applied in the z-direction, orienting the magnetizations of the wires and the thin film along the grating. Going forward, the interlayer exchange interaction will be neglected, as in real experiments it can be suppressed effectively by inserting a thin, non-magnetic spacer between the individual wires and the thin film [9].

To describe the coupling, this section will roughly follow the procedure in Ref. [8]. First the dynamic magnetization $\boldsymbol{M}^{\mathrm{K}}$ of the Kittel mode of the nanograting is derived, which in turn induces a dipole field $\boldsymbol{h}^{\mathrm{D}}$. Considering then spin waves propagating in the thin film plane, it will become apparent that their dynamic magnetization $\boldsymbol{M}^{\mathrm{SW}}$ can interact with the dipole field stemming from the grating.
When the Kittel mode is excited, the magnetization of a nanowire will precess around the direction of the effective field (z-axis) with a frequency of ω_{K} (as shown in Eq. (2.25)) and a corresponding amplitude (m_x^K, m_y^K). Neglecting inter-wire dipole-interactions in the grating, the dynamic magnetization $\boldsymbol{M}^{\mathrm{K}}$ of the grating can thus be written as [8]

$$\boldsymbol{M}^{\mathrm{K}} = \begin{pmatrix} M_x^{\mathrm{K}}(\boldsymbol{r},t) \\ M_y^{\mathrm{K}}(\boldsymbol{r},t) \end{pmatrix} = \Theta(h-x)\Theta(x) \sum_{m\geq 0}^{\text{even}} 2 f_{\mathrm{m}} \cos(k_y^{(\mathrm{m})} y) \cdot \begin{pmatrix} m_x^K \cos(\omega_{\mathrm{K}} t) \\ m_y^K \sin(\omega_{\mathrm{K}} t) \end{pmatrix}, \tag{2.32}$$

where $\Theta(x)$ denotes the Heaviside step function, $k_y^{(\mathrm{m})} = m\pi/a$ with $m \in \{2, 4, 6, ..., \infty\}$ and

$$f_m = \left(1 - \frac{1}{2}\delta_{m,0}\right) \frac{2}{\pi m} \sin\left(\frac{w}{2} k_y^{(\mathrm{m})}\right). \tag{2.33}$$

Using the dipole field [42]

$$h_\beta^D(\boldsymbol{r},t) = \frac{1}{4\pi}\partial_\beta \int \mathrm{d}\boldsymbol{r}' \frac{\partial_\alpha M_\alpha^{\mathrm{K}}(\boldsymbol{r}',t)}{|\boldsymbol{r}-\boldsymbol{r}'|} \quad \text{with} \quad \alpha,\beta \in \{x,y\} \tag{2.34}$$

and the expression for the dynamic magnetization of the nanograting $\boldsymbol{M}^{\mathrm{K}}$ from Eq. (2.32), the dipole field $\boldsymbol{h}^{\mathrm{D}}$ generated by the in-phase precession of the nanowires yields [8]

$$\boldsymbol{h}^{\mathrm{D}} = \begin{pmatrix} h_x^{\mathrm{D}}(\boldsymbol{r},t) \\ h_y^{\mathrm{D}}(\boldsymbol{r},t) \end{pmatrix} = \sum_{m\geq 0}^{\text{even}} F_{\mathrm{m}} \mathrm{e}^{|k_y^{(\mathrm{m})}|x} \left[m_{\mathrm{R}}^{\mathrm{K}} \begin{pmatrix} \cos(-k_y^{(\mathrm{m})} y - \omega_{\mathrm{K}} t) \\ \sin(-k_y^{(\mathrm{m})} y - \omega_{\mathrm{K}} t) \end{pmatrix} + m_{\mathrm{L}}^{\mathrm{K}} \begin{pmatrix} \cos(k_y^{(\mathrm{m})} y - \omega_{\mathrm{K}} t) \\ -\sin(k_y^{(\mathrm{m})} y - \omega_{\mathrm{K}} t) \end{pmatrix} \right]. \tag{2.35}$$

Note that Eq. (2.35) includes the form factor

$$F_m = f_m \cdot \left(1 - \mathrm{e}^{-|k_y^{(\mathrm{m})}|h}\right) \tag{2.36}$$

and the dynamic wire magnetization, which is separated into left- and right-circularly polarized components to simplify the expression using

$$\begin{pmatrix} m_x^{\mathrm{K}} \\ m_y^{\mathrm{K}} \end{pmatrix} = m_{\mathrm{R}}^{\mathrm{K}} \begin{pmatrix} 1 \\ 1 \end{pmatrix} + m_{\mathrm{L}}^{\mathrm{K}} \begin{pmatrix} 1 \\ -1 \end{pmatrix}. \tag{2.37}$$

The dipole field $\boldsymbol{h}^{\mathrm{D}}$ emitted by the Kittel mode of the nanograting causes the emission of two counter-propagating dipole field waves, with the respective propagation direction locked by the polarization, since $k_y^{(\mathrm{m})} > 0$. Therefore, a right-circular polarized ($m_{\mathrm{L}}^{\mathrm{K}} = 0$) excitation of the nanograting will, for example, emit a left-circular polarized dipole wave [8]. The dipole field of the nanograting $\boldsymbol{h}^{\mathrm{D}}$ can now couple to the dynamic magnetization $\boldsymbol{M}^{\mathrm{SW}}$ of spin waves in the thin film plane (parameterized by $\boldsymbol{r}_{\parallel} = y\hat{\boldsymbol{e}}_y + z\hat{\boldsymbol{e}}_z$) with a frequency ω, which can be written as [8]

$$\boldsymbol{M}^{\mathrm{SW}} = \begin{pmatrix} m_x^{\boldsymbol{k}}(x)\ \cos(\boldsymbol{k}\cdot\boldsymbol{r}_{\parallel} - \omega t) \\ -m_y^{\boldsymbol{k}}(x)\ \sin(\boldsymbol{k}\cdot\boldsymbol{r}_{\parallel} - \omega t) \end{pmatrix}. \tag{2.38}$$

The coupling of the dipole field $\boldsymbol{h}^{\mathrm{D}}$ and the dynamic magnetization $\boldsymbol{M}^{\mathrm{SW}}$ of the spin wave can now be expressed using a simple Zeeman coupling Hamiltonian (c.f. Eq. (2.7)) as [8]

$$\begin{aligned} \bar{F}_d &= -\mu_0 \int_0^{\mathrm{T}} \mathrm{d}t \int \mathrm{d}\boldsymbol{r} \boldsymbol{M}^{\mathrm{SW}}(\boldsymbol{r},t) \cdot \boldsymbol{h}^{\mathrm{D}}(\boldsymbol{r},t) = \\ &= -\mu_0 \sum_{m\geq 0}^{\text{even}} F_m \int \mathrm{d}x\, \mathrm{e}^{|k_y^{(\mathrm{m})}|\,x} \left(\tilde{m}_{\mathrm{R}}^{k_y}(x) m_{\mathrm{L}}^{\mathrm{K}} \delta_{k_y, k_y^{(\mathrm{m})}} + \tilde{m}_{\mathrm{L}}^{k_y}(x) m_{\mathrm{R}}^{\mathrm{K}} \delta_{k_y, -k_y^{(\mathrm{m})}} \right). \end{aligned} \tag{2.39}$$

In the second step of Eq. (2.39), the integration was performed over one driving cycle $T = 2\pi/\omega_\mathrm{K}$ performed by the Kittel mode in order to get the average coupling energy. Furthermore, the spin wave amplitude is again expressed via a left- and right-circularly polarized component $(m_x^{\boldsymbol{k}}, m_y^{\boldsymbol{k}})^\mathrm{T} = \tilde{m}_\mathrm{R}^{\boldsymbol{k}}(1,1)^\mathrm{T} + \tilde{m}_\mathrm{L}^{\boldsymbol{k}}(1,-1)^\mathrm{T}$. The main takeaways from Eq. (2.39) are the following [8]:

- The Kittel mode of the nanograting couples only to spin waves propagating perpendicular to the wire direction with momentum $k_y = m\pi/a$, as indicated by the Dirac delta-functions $\delta_{k_y,k_y^{(\mathrm{m})}}$ and $\delta_{k_y,-k_y^{(\mathrm{m})}}$.
- If both the Kittel mode and the spin wave are circularly polarized, they couple only if the magnetizations of nanograting and thin film are antiparallel, i.e., $\tilde{m}_\mathrm{R}^{k_y}(x) m_\mathrm{L}^\mathrm{K} \neq 0$ or $\tilde{m}_\mathrm{L}^{k_y}(x) m_\mathrm{R}^\mathrm{K} \neq 0$. However, if the Kittel mode has elliptical polarization (i.e., $m_\mathrm{L}^\mathrm{K}(x), m_\mathrm{R}^\mathrm{K}(x) \neq 0$) and only the spin wave is circularly polarized (either $\tilde{m}_\mathrm{L}^{k_y}(x)$ or $\tilde{m}_\mathrm{R}^{k_y}(x) = 0$), the coupling is perfectly chiral, even for parallel alignment of the magnetizations $\boldsymbol{M}^\mathrm{K}$ and $\boldsymbol{M}^\mathrm{SW}$.

A more intuitive picture of the coupling can be gained by visualizing both the dipole field of the grating and the dynamic magnetization of the spin wave. Using the material parameters $n = 2$, $h = 30\,\mathrm{nm}$, $w = 110\,\mathrm{nm}$ and $a = 600\,\mathrm{nm}$ (akin to experimental realizations in Ref. [10]), Fig. 2.9 (a) shows the spatial distribution of the Kittel mode dipole field $\boldsymbol{h}^\mathrm{D}$ for a right-circularly polarized mode ($m_\mathrm{L}^\mathrm{K} = 0$) at a time $t = 0$. The individual nanowires are indicated by red rectangles in the figure. The spatial orientation of the dipole field can now be compared to that of the dynamic magnetization of a spin wave: Fig. 2.9 (b) shows the spatial orientation of the spin wave magnetization at $t = 0$ for a right polarized ($\tilde{m}_\mathrm{L}^{\mathrm{k_y}} = 0$) spin wave propagating in $+y$ direction with $k_y = +2\pi/a$, whereas in Fig. 2.9 (c) a counter-propagating wave in $-y$ direction with $k_y = -2\pi/a$ is shown. It can be seen that for this example, the precession of the dipole field $\boldsymbol{h}^\mathrm{D}$ in (a) matches only with the magnetization of the wave with $k_y > 0$ in (b), but not with its analogon traveling in $-y$-direction with $k_y < 0$ in (c). Subsequently, the dipole field only couples to the $k_y > 0$ spin wave but not to the spin wave with $k_y < 0$, making the coupling chiral. This effect can be inverted by switching the relative orientation of the equilibrium magnetizations of thin film and nanograting, which is possible due to the finite magnetic anisotropy of the nanograting and a magnetically softer thin film [8]. If the thin film magnetization is reversed, Fig. 2.9 (b) and (c) switch places, thus making the coupling now stronger for $k_y < 0$. Therefore, the direction of the favored spin wave propagation direction can be controlled via external control parameters such as external magnetic fields.

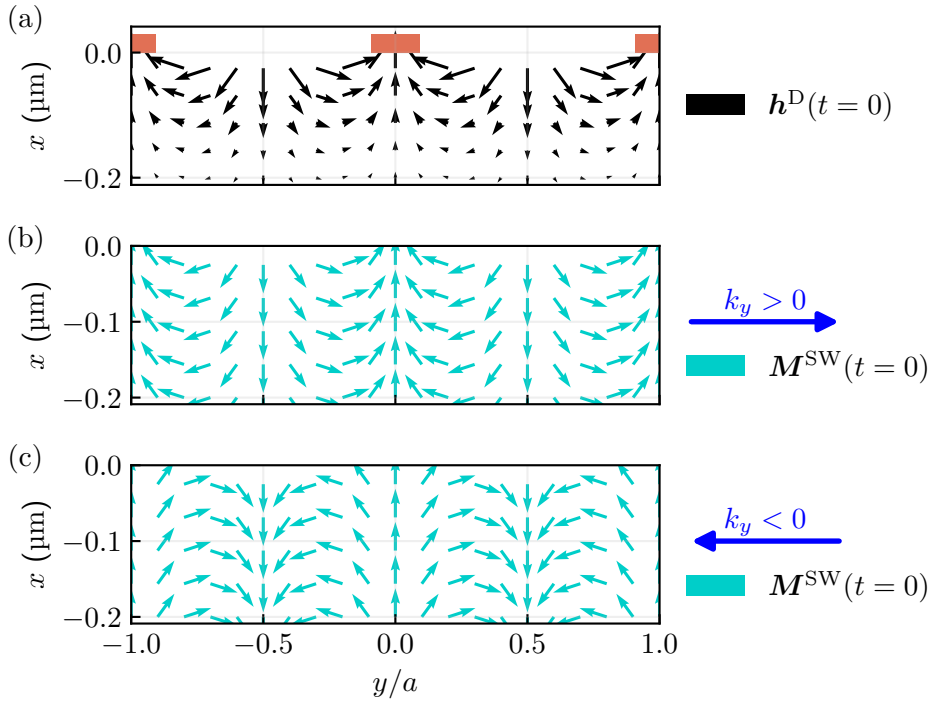

Figure 2.9: Exemplary visualization of the dipole field $\boldsymbol{h}^{\mathrm{D}}$ (c.f. Eq. (2.35)) and the dynamic magnetization of the thin film $\boldsymbol{M}^{\mathrm{SW}}$ (c.f. Eq. (2.38)) for realistic material parameters $n = 2$, $h = 30\,\mathrm{nm}$, $w = 110\,\mathrm{nm}$ and $a = 600\,\mathrm{nm}$ (taken from Ref. [10], c.f. Fig 2.8). **(a)** Dipole field $\boldsymbol{h}^{\mathrm{D}}(t=0)$ of the Kittel mode of the nano grating for a right-circularly polarized mode ($m_{\mathrm{L}}^{\mathrm{K}} = 0$). The positions of the individual nanowires are indicated by red squares. **(b)** Dynamic magnetization $\boldsymbol{M}^{\mathrm{SW}}(t=0)$ of the thin film for a right-circularly polarized mode ($\tilde{m}_{\mathrm{L}}^{k_y} = 0$) propagating to the right with $k_y = +2\pi/a$. **(c)** Dynamic magnetization $\boldsymbol{M}^{\mathrm{SW}}(t=0)$ of the thin film for a right-circularly polarized mode ($\tilde{m}_{\mathrm{L}}^{k_y} = 0$) propagating to the left with $k_y = -2\pi/a$.
The dipole field in (a) matches the precession of the spin wave with $k_y > 0$ in (b), but not for $k_y < 0$ in (c). Thus the dipole field couples only to the spin wave propagating in $+y$-direction with $k_y > 0$, making the coupling chiral. If the magnetization of the thin film is inverted with respect to the nanogratings, (b) and (c) switch places, making the dipole field now only couple for $k_y < 0$.

This mechanism for the creation of unidirectional spin waves via chiral pumping was experimentally realized by Chen *et al.* [10] in 2019. They investigated a device consisting of an array of Co nanowires with center-to-center spacing $a = 600\,\mathrm{nm}$, made from individual wires measuring $w = 110\,\mathrm{nm}$, $h = 30\,\mathrm{nm}$ placed on a YIG thin film of thickness $t_{\mathrm{TF}} = 20\,\mathrm{nm}$ (c.f. Fig. 2.8). To quantify the unidirectionality, frequency-dependent microwave transmission (S_{21} and S_{12}) and reflection (S_{11} and S_{22}) parameter spectra have been measured using a vector network analyzer. To switch between a parallel or anti-parallel orientation of the nanograting magnetization with respect to the thin film magnetization, the magnetization of the magnetically softer thin film is switched by sweeping the external magnetic field. First, the magnetizations of both the thin film as well as the nanograting are saturated by applying a magnetic field of $\mu_0 H_{\mathrm{ext}} = -200\,\mathrm{mT}$ along the wires. Afterwards, the magnetic field is swept from negative to positive values.
In Fig. 2.10 (a) the resulting reflection spectrum S_{11} is shown. Since it quantifies energy dissipated into the sample, the finite signal can be interpreted as the ferromagnetic resonance discussed in Sec. 2.3. Upon crossing the zero field, the pronounced upper mode, interpreted as the Kittel mode of the Co-grating, continues on a downward slope and only switches above $\approx 80\,\mathrm{mT}$. In contrast, the bottom mode, identified as the thin film mode, is symmetric around zero field, indicating the thin film reversed its magnetization direction whereas the grating did not yet, due to its larger demagnetization field.
To now visualize the potential non-reciprocity, the transport parameters S_{21} (corresponding to $-\boldsymbol{k}$ spin wave propagation) and S_{12} (corresponding to $+\boldsymbol{k}$ spin wave propagation) are depicted in Fig. 2.10 (b) and (c), respectively. Their parameter range is indicated by the dashed rectangle in the S_{11}-spectrum in a). In (b) and (c) the signal carried by $-\boldsymbol{k}$ ($+\boldsymbol{k}$) spin waves is only present for negative (positive) external field values and vanishes with a strong contrast at zero field. This demonstrates the generation of unidirectional (exchange-)spin waves above 18 GHz and the theoretically predicted inversion of propagation direction upon changing the relative orientation of the magnetization of thin films and grating [10].
The combination of being able to excite short wavelength spin waves with high group velocity, compatibility with ultra-thin film and switchable transport direction make chiral pumping using nanogratings a promising outlook towards the realization of unidirectional magnon devices [7]. Therefore, nanogratings as mediators for unidirectional spin waves will be the focal point of this work.

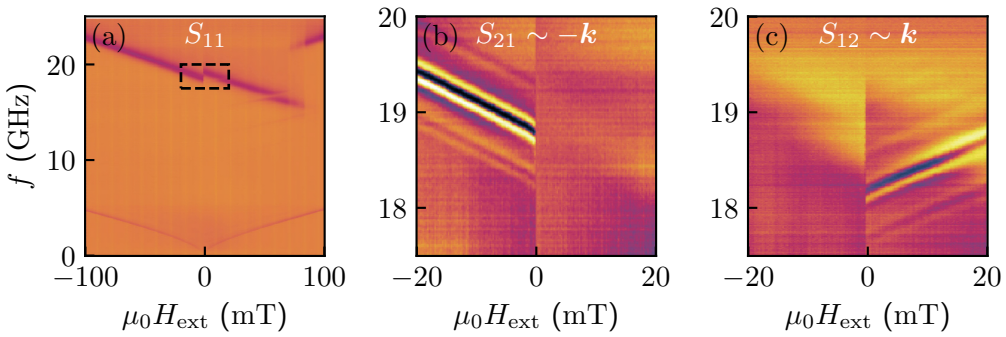

Figure 2.10: Experimental results reported by Chen *et al.* [10] of their experimental realization of unidirectional spin waves using a device of a Co-nanograting on a $Y_3Fe_5O_{12}$ (YIG) thin film with parameters $h = 30\,\text{nm}$, $w = 110\,\text{nm}$, $a = 600\,\text{nm}$ and $t_{\text{TF}} = 20\,\text{nm}$ (c.f. Fig. 2.8). **(a)** Reflection parameter S_{11} spectrum. The pronounced top mode (identified as the Kittel mode of the Co-grating) demonstrates the grating does not switch its magnetization up to a field value of about 80 mT as it is magnetically harder than the YIG thin film. According to theory this allows for switching between favored propagation directions of the chiral coupling (parallel and anti-parallel alignment of the magnetizations of thin film and nanograting). The dashed rectangle signifies the parameter range in which the unidirectionality in (b) and (c) is depicted. **(b)** Transmission parameter S_{21} spectrum, carried by spin waves with $-\boldsymbol{k}$. Strong non-reciprocity of the signal can be seen during the magnetic field sweep from negative to positive values, indicating the change of the favored propagation direction of the chiral coupling. **(c)** Transmission parameter S_{12} spectrum, carried by spin waves with $+\boldsymbol{k}$. The inverted non-reciprocity of the signal compared to the $-\boldsymbol{k}$ spin waves in (b) demonstrates that, in fact, the favored propagation direction changes at zero field, subsequently confirming the unidirectionality of the excited modes. The spin waves shown in (b) and (c) have a wavelength $\lambda \sim 60\,\text{nm}$. Figures taken from Ref. [10]

Chapter 3

Micromagnetic simulation

Micromagnetic simulations are a popular tool in modern research to investigate magnetic phenomena on scales too large for the computational modeling of singular atoms [43]. Common applications revolve around designing, predicting and understanding experiments. Therefore, simulations can be understood as a connecting piece between experiment and theory [44]. This chapter serves as an introduction to micromagnetic simulations, starting with a brief overview of the field in Sec. 3.1. Then, focus is shifted towards the software used in this work, MuMax^3 [45], explaining its core principles and structure in Sec. 3.2, before discussing the impact of different simulation parameters on the physicality of the results in Sec. 3.3. In order to verify MuMax^3 as a simulation tool for dynamic magnetic properties, the workflow behind creating a typical ferromagnetic resonance simulation is explained in Sec. 3.4, comparing the output with the theoretical results from Ch. 2. Finally, this chapter is closed by detailing the developed post-processing algorithms necessary to compare micromagnetic simulations to experimental results in Sec. 3.5.

3.1 Overview

The term *micromagnetics* describes a theory developed by W. Brown [46] in an effort to describe ferromagnetic materials. Its goal was to model ferromagnetism on "intermediate" length scales, where instead of considering the spins of individual atoms, a continuum theory is used to describe the material using a continuous function of the magnetization vector [43]. Effectively, this allows for using calculus to describe magnetic phenomena on length scales of the order of 0.01 µm to 10 µm [43]. The magnetization dynamics in this framework are described by the time- and space-dependent version of the previously derived Landau-Lifshitz-Gilbert (LLG) equation (c.f. Sec. 2.2.2):

$$\frac{\mathrm{d}\boldsymbol{M}(\boldsymbol{r},t)}{\mathrm{d}t} = -\frac{\gamma\mu_0}{1+\alpha^2}\boldsymbol{M}(\boldsymbol{r},t)\times\boldsymbol{H}_{\mathrm{eff}}(\boldsymbol{r},t) - \frac{\alpha\gamma\mu_0}{M_{\mathrm{s}}(1+\alpha^2)}\boldsymbol{M}(\boldsymbol{r},t)\times\frac{\mathrm{d}\boldsymbol{M}(\boldsymbol{r},t)}{\mathrm{d}t}. \tag{3.1}$$

Note that Eq. (3.1) differs from the previously derived Eq. (2.18) due to the fact that the gyromagnetic ratio γ and the Gilbert damping parameter are both scaled by an extra factor of $1/(1+\alpha^2)$ as a correction term, since Eq. (2.18) is technically an approximation for $\alpha \ll 1$. Unfortunately, Eq. (3.1) is hard to solve exactly, e.g., due to the ambiguity of initial- and boundary-conditions, leading to big interest towards numerical solutions [47].
Coupled with the rise of cheaply available computational power, this has led to the rise of the now vast field of *micromagnetic simulations*. In research they nowadays find wide application with different intentions, such as trying to replicate experiments to gain insight into the physical mechanisms behind observations, making predictions about novel phenomena or testing and optimizing designs for setups [44]. Although many different software solutions exist nowadays, the core principle is nearly the same for all of them: discretize the magnetic volume into a finite number of computational cells and solve the LLG Eq.(3.1) in these cells as an ordinary differential equation (ODE) in time [44].
In terms of discretization, two basic approaches are commonly used. The first is called finite-difference-method (FDM) and works by dividing the simulated material into a regular array of orthorhombic unit cells, making it possible to directly express derivatives via finite difference approximations. Here, physical quantities are represented directly on-site for each mesh point without additional interpolations [48]. The strong suits of FDM are that it leads to efficient and fast calculations and is quite easy to set up, however, it can struggle to provide accurate solutions of irregularly shaped samples [48]. A second popular approach is the finite-elements-method (FEM), which divides the sample into an irregular array of cells called "elements" (often tetrahedron-shaped). Hereby, the mesh density is increased in areas where large forces are expected. Physical quantities (i.e., fields) are then represented using nodal basis functions and continuous (often polynomial) interpolation between the elements [48]. FEM excels at the local resolution of the solution and can handle arbitrarily shaped samples well, however, at the cost of complexity, increased calculation time and the caveat of the solution being very sensitive to the type of mesh chosen [48].

In general, micromagnetic simulations can be split into two types: static simulations aim to find an equilibrium configuration of the magnetic moments in the sample after sufficiently long time, and are often used to simulate magnetic hysteresis loops, finding the magnetic ground states before dynamics considerations or to evaluate the static magnetic (stray) fields created by a certain magnetic configuration [44]. Dynamic simulations, on the other hand, aim to deliver the magnetization as a function of time, allowing insight into effects such as ferromagnetic resonance, spin wave dynamics or domain wall motion to name a few [44].

3.2 MuMax^3

MuMax^3 is an open-source software for micromagnetic simulations developed by the DyNaMat group of the University of Ghent, Belgium [45]. Among the first open-source programs, MuMax^3 allows to use relatively inexpensive consumer market gaming graphics-processing-units (GPUs) and their parallel processing capabilities to accelerate micromagnetic simulations by around two orders of magnitude compared to similar programs running on traditional CPUs [49]. Written in Go (see Ref. [50]) and CUDA (Compute Unified Device Architecture, see Ref. [51]), the only requirements for running MuMax^3 are an NVIDIA GPU and the corresponding GPU drivers, thus having a low cost entry-barrier [45]. In the following, a rough sketch of its basic design will be given, following the original publication by Vansteenkiste *et al.* [45].
MuMax^3 uses a 2D or 3D finite-difference discretization of the simulation volume into orthorhombic cells. Volumetric quantities, such as the magnetization, are considered at the center of each of these cells, whereas coupling quantities such as the exchange coupling strength are considered at the faces between cells. These parameters are, however, not stored for each cell, but rather in look-up tables in an effort to conserve memory. This is done by further subdividing the sample in the simulation volume into a maximum of 256 material *regions* with region indices $0, ..., 255$, where for each region separate material parameters and external excitations (magnetic fields) can be assigned. In principle, this allows a maximum of 256 different magnetic materials to be considered in one simulation.
Different *geometries* (e.g., cuboids, spheres, cylinders, ...) are defined in MuMax^3 using boolean functions (e.g., sphere: $f(x, y, z)$ returns true if (x,y,z) inside the sphere, false otherwise), which can be translated, rotated, scaled, repeated and combined with other geometries using boolean operators. Geometries can be used to define the *shape* of the magnet, necessary in cases where the shape of the simulation box (i.e. cuboid) is not equal to that of the considered magnet. The combination of geometries and material regions thus allows the construction of a magnetic system of arbitrary complexity in terms of material composition or geometry. Furthermore, periodic boundary conditions (PBC) can be applied in each spatial dimension, implying a wrap-around magnetization for short-range interactions. For the long-ranged dipole interaction, PBC are approximated by simulating a (large) finite amount of copies of the simulation box in each spatial direction, the exact number of which can be set by the user.
As for initializing the system, the initial magnetization orientation can be set into various shapes (e.g., uniform, vortex, domains,...) for either different material regions or in geometric areas of the simulation box. Excitations in form of external magnetic fields can be static or dynamic in both time and space,

supporting also the import of previously generated vector fields. As for material parameters, at least the saturation magnetization M_s (`Msat`), the exchange stiffness A_ex (`Aex`) and the Gilbert damping parameter α (`alpha`) must be supplied for simulations to run.
The magnetization dynamics are calculated for each cell by solving a simplified Landau-Lifshitz-Gilbert (LLG) equation in time:

$$\begin{aligned}\frac{\mathrm{d}\boldsymbol{M}(\boldsymbol{r},t)}{\mathrm{d}t} =& -\frac{\gamma\mu_0}{1+\alpha^2}\boldsymbol{M}(\boldsymbol{r},t)\times\boldsymbol{H}_\mathrm{eff}(\boldsymbol{r},t)\\ &-\frac{\alpha\gamma\mu_0}{M_\mathrm{s}(1+\alpha^2)}\boldsymbol{M}(\boldsymbol{r},t)\times(\boldsymbol{M}(\boldsymbol{r},t)\times\boldsymbol{H}_\mathrm{eff}(\boldsymbol{r},t))\,.\end{aligned} \tag{3.2}$$

Notably, Eq. (3.2) differs from the original analytic expression in Eq. (3.1) by assuming that for small Gilbert damping α, $\mathrm{d}\boldsymbol{M}(\boldsymbol{r},t)/\mathrm{d}t$ can be approximated by the first term (precession) of Eq. (3.1). The physics of the system is considered via various contributions to the effective field landscape $\boldsymbol{H}_\mathrm{eff}$. The solution of the LLG in Eq. (3.2) in time for dynamic magnetic simulations is handled by a number of available explicit Runge-Kutta-methods (see e.g., Ref. [52]), offering a dynamical time step control based on error boundaries or fixed time steps. In order to minimize the energy of a given magnet (i.e. bringing the system into energetic equilibrium via static simulation), MuMax^3 will disable the precession term in Eq. (3.2) and propagate the system in time until the system energy is converged in the scope of numerical precision. Then, the torque between neighboring cells will be monitored as a more precise measure of equilibrium: the system is again propagated in time until the torque converges and is no longer distinguishable from numerical noise. It should be noted that even though this procedure usually succeeds in finding the energetic equilibrium, depending on the system it is always possible to accidentally end up in a saddle-point or generally flat part of the energy landscape.
The output of MuMax^3 simulations can be delivered via two channels: first, each simulation automatically generates a `table.txt` output table, saving the averaged magnetization components either manually or in automated time steps. Arbitrary quantities may be added to the table in the simulation script, and are then also averaged over the sample and saved in the table. Alternatively, the spatial quantities such as the magnetization can be exported as entire vector fields, saved in the open-vectorfield-format `.ovf`, also either manually or at fixed time steps.

3.3 Impact of simulation parameters

Due to the multitude of different parameters that go into a micromagnetic simulation in MuMax^3, it is important to know how these parameters influence not

only the physicality of the results but also the computational expense. This is especially true for larger simulations involving broad field sweeps or long sampling to obtain high resolutions, where the computational efficiency of a single simulation run is of the essence. This section attempts to discuss how to design simulations and choose parameters in such a way that they produce the desired physical results reliably and fast.
An important parameter not discussed explicitly in the following sections is temperature. In principle, MuMax^3 allows to consider arbitrary sample temperatures, which are accounted for via the addition of a fluctuating magnetic field contribution to the effective magnetic field [45]. This is, however, in most cases not desirable, as the addition of these fluctuating fields causes discontinuities in the magnetic torque of the system and therefore forces the system to choose a lower-order integration algorithm [45]. Specifically, these lower order integration algorithms do not offer variable time steps and have a uncertainty two to three orders of magnitude worse in the time step, forcing the user to adapt the manual time step accordingly [45]. We conducted test simulations with different finite temperatures and found that temperature effects do not alter the dominant modes of the spectrum, but lead to worse contrast due to higher background noise and a broadening of the modes in frequency (see Appendix A.1.2). Subsequently, simulating at finite temperatures impedes our goal of simulating as efficiently as possible, as they increase the simulation time oftentimes from hours to days, while also bearing no observable influence of the physical nature of the modes. Therefore, in this thesis, all simulations are performed at a sample temperature of 0 K.

3.3.1 Mesh

A very basic but one of the most influential user inputs is defining the finite-difference (FD) mesh used to discretize the sample. The core quantity in defining the mesh are the dimensions of a single computational grid cell (c_x, c_y, c_z). There, one is confronted with a weigh-off: on one hand, choosing the cells very large results in a lower amount of computational cells in the simulation box, which drastically increases performance in FDM solvers and thus lowers the simulation time [44]. On the other hand choosing large cell sizes has been shown to generate large errors in the results due to underestimating the exchange interaction, while also causing problems in resolving curves in sample geometries [14, 44]. As previously derived in Sec. 2.4, the exchange length l_{ex} gives the length scale of exchange-interaction dominated effects. Therefore, as a general rule of thumb, if one wants to simulate exchange-interaction influenced phenomena, such as exchange spin waves or dipole-exchange spin waves, it is necessary to choose a cell size $(c_x, c_y, c_z) < l_{\mathrm{ex}}$ [14, 44]. Conversely, a cell size larger than l_{ex} was

found to be unproblematic for dipole-interaction dominated phenomena such as ferromagnetic resonance or magneto-static spin waves in thin films, as the error induced by different cell sizes is comparable to typical experimental resolutions [14]. Apart from its influence on the physical results, the cell size also controls the range of observable wave numbers k for spin wave dispersion simulations. This is due to the Shannon-Nyquist-theorem, stating that the maximum wave number resolvable is determined by the sampling rate in real space (i.e. cell size) via $|k_{x,\max}| = 2\pi/2c_x$ [53]. Another important choice to make when configuring the simulation mesh is whether to use periodic boundary conditions (PBC). It has been found that proper ferromagnetic resonance is not possible in simulated finite-size thin films due to the stray fields at the edges prohibiting uniform precession [14]. This can be remedied by using in-plane PBC, effectively removing the edge effects [14]. In general, it makes sense to almost always use PBC, as it usually enhances the physicality of the simulations and the performance hit taken due to more complex magneto-static kernel calculations is more often than not negligible. It then makes sense to choose a high number of "copies" of the simulation box to calculate the dipole field (c.f. Sec. 3.2). In this thesis usually $\mathrm{PBC}_x = \mathrm{PBC}_y = 100$ is chosen, as this already achieves good agreement with analytical limits [45]. However, in the case of some specific simulations it makes sense to disable PBC in a particular direction to, e.g., determine the attenuation of the signal.

3.3.2 Sample

After configuring the mesh, the next important point of consideration is the size (l_x, l_y, l_z) of the simulated sample, which is controlled by the number of grid cells (N_x, N_y, N_z) in each spatial direction. This is especially relevant in cases, where PBC cannot be used, e.g., due to interest in spin wave attenuation. For ferromagnetic thin films, it was found that for the results to agree with those using PBC (and thus the analytical expectation), the simulated thin film must be constructed such that the in-plane extension must be around 1000 times larger than the thickness [14]. This implies huge computational effort and demonstrates that PBC are an efficient way to simulate realistic magnetic systems by greatly reducing simulation time for large samples.
Furthermore, the number of cells constituting the simulation box in each spatial direction (N_x, N_y, N_z) also plays an important role in spin wave dispersion simulations, as the number of cells in real space corresponds to the total number of samples. Thus, via elementary properties of the fast-Fourier-transform (FFT) the maximally achievable resolution in reciprocal space, δk_x, is connected to the cell size c_x and the number of cells N_x via $\delta k_x = 1/(c_x N_x)$. It is therefore advisable to choose a large $N_{x,y,z}$ in the sample direction, where finite

$k_{x,y,z}$ properties are to be resolved, and as low as possible in the other sample directions to balance the computational effort.
The most important constrain on (N_x, N_y, N_z) in terms of performance comes directly from MuMax^3 and is more relevant than the absolute number of cells: the largest bottleneck is given by the CUDA FFT routine, which works fastest if (N_x, N_y, N_z) are all chosen as powers of 2, e.g., $(256, 128, 2)$ [45]. This is extremely relevant for the performance of all simulations and should always be respected.
Lastly, attention is shifted towards the `edgesmooth` parameter of MuMax^3. Its purpose is to further define the resolution of geometries or shapes by subdividing simulation cells that are on their boundary. Specifically, `edgesmooth` is an integer parameter, where `edgesmooth=n` implies a further subdivision of a cell on the edge of a structure into n^3 subcells, scaling the saturation magnetization accordingly. This enables a much more realistic calculation of the magneto-static field by determining the number of the subcells that lie in versus outside of the geometry edge. Usually, choosing `edgesmooth=8` results in accurate results for smooth edges, however, it has to be considered that not well-resolved edges may induce pinning effects or nucleation points, which mimics the effects of disorder in experimental settings [54].

3.3.3 Magnetic Excitations

Excitations in MuMax^3 are realized via adding various static and dynamic external magnetic fields to the simulation landscape. Static fields are used for saturating the sample magnetization along a certain axis and can be swept to record broad-band ferromagnetic resonance spectra. In their usual, spatially homogeneous form, they are defined by a simple direction vector and field strength value. Here, it can be advantageous to misalign this direction vector with the actual desired direction by a small angle ($\approx 1°$) to mimic experiments, where experimental uncertainties make it challenging to determine the exact orientation of sample and external field [14].
All dynamical simulations include some form of external excitation applied to the sample to probe its response. Since the form of the excitation is entirely up to the user to be defined in MuMax^3, it is important to know the implications of different excitation types. Designing a driving magnetic field can be broken down into three choices: the temporal shape, the spatial shape and the amplitude of the signal.
For the temporal shape, a straightforward approach would be to use a Dirac delta distribution $\delta(t)$, due to its property of uniformly exciting the entire frequency range. However, since numerics work in discrete time domains, this is not feasible [44]. Rather, one would have to use a Gaussian pulse profile,

$H_{\mathrm{G}}(t) = \exp(-a(t-t_0)^2)$, as an approximation, which is a common choice for studies of a range of large wave vectors [44]. A much more popular choice, however, is a sinc-type excitation:

$$H_{\mathrm{s}}(t) = \mathrm{sinc}(2\pi f_c(t-t_0)) = \frac{\sin(2\pi f_c(t-t_0))}{2\pi f_c(t-t_0)}, \tag{3.3}$$

where f_c defines the cut-off frequency and t_0 is the temporal delay of the signal. The sinc-shape in Eq. (3.3) is favored as its frequency space representation (in an ideal, continuous case) is given by a rectangle function. This allows the definition of the range of desired excited frequencies, but also helps avoid spectral aliasing, which can introduce numerical artifacts in the final spectra [44]. A common mistake in literature is to claim that H_s in Eq. (3.3) will have an approximately rectangular Fourier representation with borders $[-f_c, f_c]$ [14, 44]. This is incorrect due to the factor π in the argument of Eq. (3.3) as shown in Fig. 3.1, where the real-time signal $H_{\mathrm{s}}(t)$ in (a) can be compared to the energy-spectral-density ESD $= 40\log_{10}|\mathrm{FFT}(H_{\mathrm{s}})|$ in (b). The parameters chosen for this example are $f_c = 100\,\mathrm{GHz}$ and $t_0 = 50\,\mathrm{ps}$, as they are also the typical choice in the following of this thesis. Fig. 3.1 (b) shows that the signal in (a) provides a uniform excitation energy in the interval [-πf_c, πf_c] with a steep fall-off outside of this range.
As for the spatial shape of the excitation, the easiest case is to use a spatially homogeneous magnetic field varying only temporally, which is useful for simulating ferromagnetic resonance. In terms of simulating spin wave dispersions, it is recommendable to use a sinc-type excitation also in real space, completely analogous and for the same reasons as the temporal case:

$$H_{\mathrm{s}}(x) = \mathrm{sinc}(2\pi k_c(x-x_0)) = \frac{\sin(2\pi k_c(x-x_0))}{2\pi k_c(x-x_0)}, \tag{3.4}$$

where k_c defines a cut-off wave number to get a total excitation of shape $H_{\mathrm{ext}} = H_{\mathrm{s}}(x) \cdot H_{\mathrm{s}}(t)$ [44, 55].
Finally, the amplitude h_0 of the external excitation must be chosen. Since usually only the linear response regime is probed, the excitation must be weak enough to not introduce non-linear effects. This is usually fulfilled for $h_0 = 1\,\mathrm{mT}$, which is the value used in this thesis [14, 44].

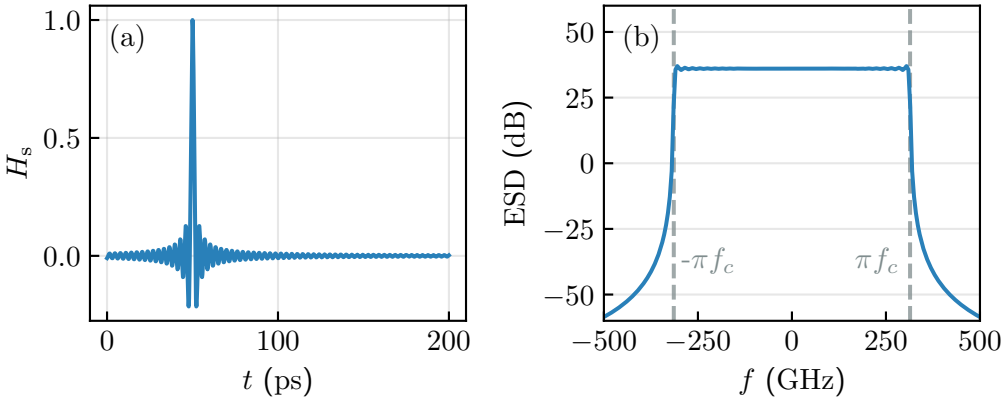

Figure 3.1: Comparison of a sinc-type temporal excitation pulse and its energy spectrum in frequency space. **(a)** Signal $H_s(t) = \mathrm{sinc}(2\pi f_c(t - t_0))$ with parameters $t_0 = 50\,\mathrm{ps}$ and $f_c = 100\,\mathrm{GHz}$. **(b)** Energy spectral density $\mathrm{ESD} = 40\log_{10}|\mathrm{FFT}(H_s)|$ of the signal shown in (a). The ESD assumes an approximately (due to discrete numerics) rectangular shape, with maximum energy being evenly distributed in the interval $[-\pi f_c, \pi f_c]$. Outside of this interval the energy provided by the pulse in (a) drops off steeply, only providing weak to negligible excitation. Sinc-type excitations in time are thus well suited to excite a pre-defined range of frequencies.

3.3.4 Simulation

Apart from defining the sample and its discretization or the type of excitation, the exact manner in which the simulation is conducted also plays an important role in the eventual results. As for static simulations, finding the ground state of the magnetic sample can be achieved via two internal functions in MuMax[3]: `relax()` and `minimize()`. In most cases, it is recommendable to use `relax()` as it is the more robust variant to minimize the energy, whereas `minimize()` is usually much faster but more prone to divergence [56]. However, the function `minimize()` is useful for simulating detailed hysteresis curves, where small incremental changes in the external magnetic field value cause the sample never being too far out of equilibrium [56].
As for dynamical simulations, two important parameters need to be set: the total simulated timespan T and the saving interval of the output files dt. Starting with T, two points are to be considered: first, the simulation should be long enough so that the sample can reach equilibrium. Second, the total simulation time also controls the maximum resolution in frequency space that can be resolved in this simulation via $\delta f = 1/T$ (similarly to the sample size in real space in Sec. 3.3.2). These two points favoring simulating long time spans have to be weighed against the additionally induced computational effort. It was found that in the realm

of this work $T = 20\,\text{ns}$ is usually a good choice to satisfy both precision and efficiency concerns. For the sampling interval dt the Shannon-Nyquist-theorem must be considered to choose dt in such a way that only frequencies up to a maximum value f_c are sampled: $dt = 1/(2f_c)$ [53]. This allows to save storage by not sampling irrelevant frequencies and can be matched with the maximally induced excitation frequency (c.f. Sec. 3.3.3).

3.4 Simulation workflow and verification of MuMax^3

This section seeks to deliver a practical guide on how the MuMax^3 simulations were constructed for this work, while also serving as a proof of concept to validate the obtained results. Scripting in MuMax^3 follows the syntax of the Go programming language (see Ref. [50] for a detailed description), extended by certain keywords, functions and parameters. An overview of the internal parameters and supported functions can be found in the MuMax^3 API in Ref. [56]. In the following, a basic ferromagnetic resonance experiment will be simulated for a ferromagnetic rectangular wire made of permalloy ($Ni_{80}Fe_{20}$) as an illustrative example of the general MuMax^3 procedure and a consistency check whether the simulation agrees with the theory as established in Sec. 2.3. Note that representative examples of the actual code used in this work to conduct micromagnetic simulations are included in the Appendix B.1.

Setting up the simulation box Starting off, the simulation box (the mesh) must be initialized. For this example, it will be sized $(l_x, l_y, l_z) = (1000\,\text{nm}, 1000\,\text{nm}, 10\,\text{nm})$ (see coordinate system in Fig. 4.1). In order to choose the correct number of cells to discretize this box, the exchange length for permalloy $l_{\text{ex}}^{\text{NiFe}} = 5.69\,\text{nm}$ [14] gives a physically sensible upper bound for the size of a single cell to fulfill $(c_x, c_y, c_z) < l_{\text{ex}}^{\text{NiFe}}$. This code example will determine the number of grid cells $N_{x,y,z}$ by using the integer binary logarithm (`ilogb`) function of MuMax^3, in order to automatically have cell numbers as powers of 2. Periodic boundary conditions will not be used to simulate a single wire of finite length.

```
//Simulation box dimensions
lx := 1000e-9
ly := 1000e-9
lz := 10e-9
//Approximately desired cell sizes
cx := 3e-9
```

```
cy := 3e-9
cz := 10e-9
//Calculate number of cells to discretize simulation box
Nx := pow(2, ilogb(lx/cx))
Ny := pow(2, ilogb(ly/cy))
Nz := pow(2, ilogb(lz/cz))
//Do not use periodic boundary conditions
PBCx := 0
PBCy := 0
PBCz := 0

//Set up the final mesh
SetMesh(Nx, Ny, Nz, lx/Nx, ly/Ny, lz/Nz, PBCx, PBCy, PBCz)

//Use edgesmooth
Edgesmooth = 8
```

Constructing the wire sample The geometry of the wire can be set by using the internal `cuboid` function to first create a geometry object, which can then be set as the magnet shape. Geometry objects are always centered around the origin (i.e. center of the simulation box), similar to the sketch in Fig. 2.1. The wire shall have the measurements $(d_x, d_y, d_z) = (200\,\mathrm{nm}, 1000\,\mathrm{nm}, 10\,\mathrm{nm})$. The material parameters of the wire will be set by defining the wire as the material region with index 1, using $M_\mathrm{s} = 800\,\mathrm{kA/m}$, $A_\mathrm{ex} = 13\,\mathrm{pJ/m}$ and $\alpha = 0.01$ [14, 55].

```
//wire geometry
dx := 200e-9
dy := 1000e-9
dz := 10e-9
wire := cuboid(dx, dy, dz)

//the total magnet geometry is just the wire
setgeom(wire)

//assign material region and parameters
defregion(1, wire)
msat.setregion(1, 800e+3)
alpha.setregion(1, 0.01)
aex.setregion(1, 13e-12)
```

Relax system into groundstate Simulated samples are usually initialized with random magnetization, before relaxing into energetic equilibrium after applying an external bias field. Typically when simulating ferromagnetic resonance (FMR), a field sweep will be performed, thus it is sensible to iteratively relax the system for each subsequent field value as well. Here, a field sweep will be performed from $\mu_0 H_{\text{ext}} = 0.5\,\text{T}$ to $\mu_0 H_{\text{ext}} = -0.5\,\text{T}$ in 4 mT increments, where H_{ext} is applied along the y-axis.

```
//Initialize a random magnetization
m = RandomMag()
//Apply the maximum static field value in y-direction
B_ext = vector(0, 0.5, 0)
//Relax the system into equilibrium
Relax()
```

Define excitations For FMR, usually the excitation of choice is uniform in space and sinc-shaped in time (c.f. Sec. 3.3.3). The parameters for the temporal sinc Eq. (3.3) are $f_{\text{c}} = 100\,\text{GHz}$ and $t_0 = 50\,\text{ps}$. The sinc-excitation will be applied perpendicular to the static magnetic field H_{ext} in x-direction with a maximum amplitude of 1 mT.

Set simulation parameters As established in Sec. 3.3.4, a simulation time of $T = 20\,\text{ns}$ is usually sufficient for the system to reach equilibrium. This timespan will thus be simulated for each external field value in the field sweep of the FMR simulation. The sampling (i.e. saving the averaged magnetization to the output table) will be performed every $dt = 5\,\text{ps}$, which according to the Shannon-Nyquist sampling theorem allows to resolve signals of a maximum frequency of 100 GHz, which is sufficient for this case [53]. In this example, ferromagnetic resonance will be simulated, which ideally would correspond to a collective, in-phase precession of the entire sample. This involves averaging ("integrating") the magnetization over all grid cells anyway. Therefore, it makes sense to not even output the magnetization data for the entire sample in order to save storage. This is realized easily by simply auto-saving the `table` output in the desired interval, as it only contains spatially averaged data:

```
tableautosave(5.0e-12)
```

Run simulation The dynamic part of the simulation will be handled using a simple `for`-loop structure, sweeping over the external field values. Here, it is crucial that in the output table, each saved value of the magnetization can be identified by two associated entries: the point in time where it was recorded, and

the current value of the magnetic field sweep. In each iteration, the simulation time t will be reset, as otherwise, the excitation (being t-dependent) will only be present in the first iteration. Then, the system will be relaxed after applying the new field value, before adding the dynamic component to the external field. Finally, the simulation is started using `run`.

```
//Initialize the B_stat variable to keep track of the field sweep
B_stat := 0.5
//Keep track of B_stat by adding it to the output table
TableAddVar(B_stat, "B_stat", "T")

//Field sweep simulation using a for-loop
for B_stat=0.5; B_stat>=-0.5; B_stat-=4e-3{

    //Reset the simulation time
    t = 0

    //Apply new static field and relax the structure
    B_ext = vector(0, B_stat, 0)
    Relax()

    //Add the driving field in x-direction (ampl. = 1mT)
    B_ext = vector(1e-3*sinc(2*pi*100e+9*(t - 50e-12)), B_stat, 0)

    //Run the simulation for 20ns
    run(20e-9)
}
```

Comparison to theory At last, to verify that MuMax^3 and the numerical analysis explained in Sec. 3.5 are able to reproduce the analytical solutions, the results of the simulation built in this section will be compared to the Kittel formula (c.f. Eq. (2.25)), using the demagnetization factors determined via Eq. (2.13). In Fig. 3.2, the output spectrum of the simulation is shown as a two-dimensional colormap, allowing to view the results as both a function of frequency f and external field strength $\mu_0 H_{\text{ext}}$. Additionally, the analytical result as given by the Kittel equation (2.25) is shown as a red dotted line. It can be seen that the analytical curve shows reasonable agreement with the dominant FMR mode in the simulated spectrum. The additionally visible but far weaker mode below the FMR mode in the simulation spectrum can be attributed to an edge-mode of the wire caused by the boundaries in y-direction. As no periodic boundary conditions were used, additional stray fields accumulate at the edges,

leading to the formation of edge-domains and the corresponding excitation [14]. The discrepancy between the analytical curve and the simulation spectrum in a range of approximately $\mu_0 H_{\text{ext}} = 0$ to $\mu_0 H_{\text{ext}} = -50\,\text{mT}$ can be explained by the shape anisotropy of the wire: the magnetization of the wire does not immediately switch upon sweeping from positive to negative external field values. All in all, this example simulation illustrates the typical workflow for simulating FMR while verifying the methodology by matching the analytical result well.

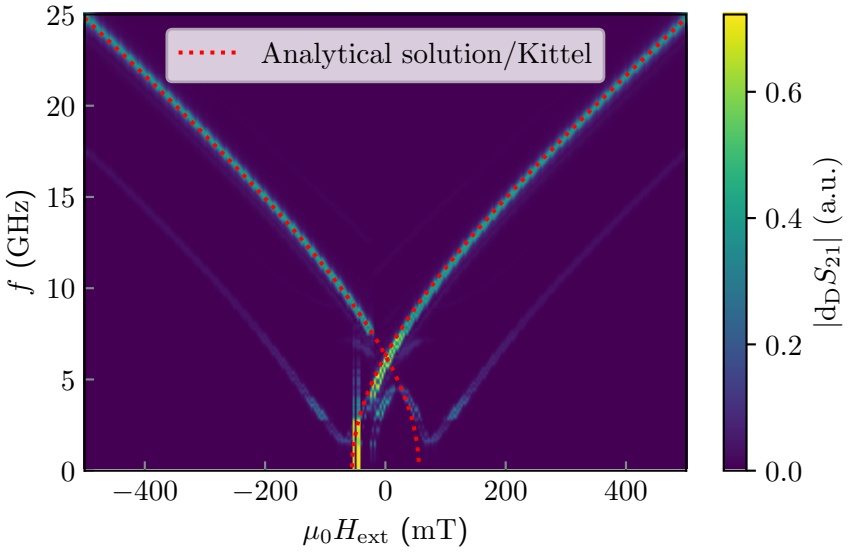

Figure 3.2: Result of the ferromagnetic resonance (FMR) simulation of a $Ni_{80}Fe_{20}$ ($M_s = 800\,\text{kA/m}$, $A_{\text{ex}} = 13\,\text{pJ/m}$ and $\alpha = 0.01$ [14, 55]) rectangular prism with dimensions $(d_x, d_y, d_z) = (200\,\text{nm}, 1000\,\text{nm}, 10\,\text{nm})$, compared to the analytical solution as given by the Kittel equation (2.25). The simulation result $|S_{21}|$ is shown as a two-dimensional color spectrum as a function of both frequency f and external field $\mu_0 H_{\text{ext}}$. The solution of the Kittel formula (red dashed line) shows reasonable agreement with the spectrums dominating main mode, which is identified as the FMR mode. A weaker, lower frequency mode is also visible in the spectrum, which can be explained as an edge-mode of the prism in y-direction, induced by additional stray fields due to open boundary conditions. The coercivity of the cuboid ferromagnet caused by the shape anisotropy explains the discrepancy between the theory curve and the spectrum between $\mu_0 H_{\text{ext}} = 0$ to $-50\,\text{mT}$: the branch of the FMR mode coming from positive field values continues, indicating non-switching wire magnetization.

3.5 Data analysis

After running micromagnetic simulations, the raw output, such as the magnetization or effective magnetic field as discrete functions of space and time, has

little use by itself, since, as initially discussed in this chapter, most motivations in micromagnetic simulations revolve around either predicting, optimizing or understanding experimental findings. Thus, it is indispensable to apply post-processing and data analysis to the raw simulation output with the goal of recovering data, which can be more or less directly compared to experimentally accessible parameters. This section lays out an overview of the post-processing algorithms developed in the realm of this thesis.
Generally, all post-processing in this work is done in PYTHON. Note that in the following, all quantities are discrete-valued; however, for didactic purposes the notation of continuous functions will be used at some points. As for the general simulation output, the quantities are saved either only time- or both space- and time-dependent. Usually, time-dependent data such as $\boldsymbol{M}(t)$ is obtained via the table output of MUMAX^3 by including the command `tableautosave(ts)` in the simulation script to sample spatial averages in intervals of `ts`. This holds the big advantage that by averaging before saving, the storage demands of the simulation are drastically reduced, typically from the order ofGB to MB. The output table can also be used to save space-dependent output data when simulating periodic structures, i.e., magnonic crystals. For the latter, it makes sense to periodically save spatial averages of each periodic object, e.g., a nanowire, by adding certain simulation cells to the output table using the `crop` command. Most commonly, space- and time-dependent data, e.g., $\boldsymbol{M}(\boldsymbol{r}, t)$, is obtained by saving the entire vector-field of, e.g., the magnetization `m` in intervals of `ts` using `autosave(m, ts)` in the simulation script.
In Fig. 3.3, a flow-chart depicts different kinds of data presentation used in this thesis, depending on the output of the simulation. If the sample magnetization $\boldsymbol{M}(t)$ is saved only as a function of time, i.e. averaged over the entire structure, only quantities regarding a collective sample response may be obtained, as illustrated on the left portion of Fig. 3.3. Most commonly, these will be resonance spectra as functions of external parameters like the frequency f, the magnetic field strength $\mu_0 \boldsymbol{H}_{\text{ext}}$ or magnetic field angle ϑ, which are obtained from $\boldsymbol{M}(t)$ by numerically determining either the systems susceptibility $\hat{\boldsymbol{\chi}}$ or the transmission parameter S_{21}, background corrected using the derivative-divide method [57], i.e., $\mathrm{d_D}S_{21}$, as a function of these quantities. A more detailed description of the workflow behind resonance spectra is discussed in Sec. 3.5.1.
For a more intricate analysis of the sample behavior, it is necessary to save the magnetization $\boldsymbol{M}(\boldsymbol{r}, t)$ as a both time- and space-dependent vector field, as depicted on the right half of Fig. 3.3. Commonly, the output $\boldsymbol{M}(\boldsymbol{r}, t)$ will be used to provide more elaborate insight into the previously mentioned resonance spectra. By obtaining a frequency- and space-dependent power distribution $P(f, x, y, z)$, the spatial mode profiles at fixed frequencies may be obtained, allowing to assign the visible modes in the resonance spectra to their actual

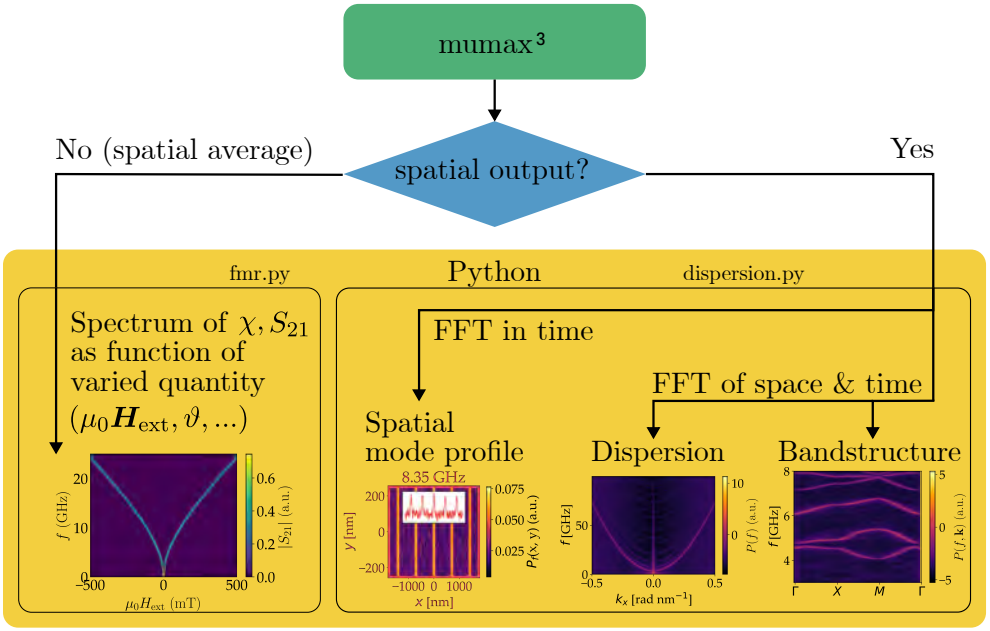

Figure 3.3: Flowchart depicting the possibly obtainable data depending on the simulation output of MuMax³. If the spatial average of the magnetization $\boldsymbol{M}(t)$ is saved, only the averaged response of the entire magnet (or region) is accessible. This allows for spectra depicting the frequency behavior of the susceptibility χ or the background-corrected transmission parameter $\mathrm{d_D}S_{21}$ to swept system parameters such as the external field strength $(\mu_0 H_{\text{ext}})$ or magnetic field angle (ϑ). Saving the magnetization $\boldsymbol{M}(\boldsymbol{r}, t)$ in a spatially resolved format allows more detailed examination of the system properties. By transforming the output data into frequency space using a fast-Fourier-transform (FFT), spatial mode profiles can be obtained allowing to classify the nature of system modes. If being brought into frequency and momentum space using a multi-dimensional FFT, the spin wave dispersion relation can be visualized along certain sample directions up to multi-dimensional band structures.

physical interpretation. The algorithm behind spatial mode profiles is explained in more detail in Sec. 3.5.2. Spatially resolved magnetization $\boldsymbol{M}(\boldsymbol{r}, t)$ also enables the analysis of finite wave vectors $\boldsymbol{k}$ by transferring it into reciprocal space. In its simplest form, this allows to obtain dispersion spectra along a specified transport direction, as detailed in Sec. 3.5.3. More involved techniques allow to obtain the band structure by traversing over momentum space, as discussed in Sec. 3.5.4.

3.5.1 Parameter sweep spectrum

Ferromagnetic resonance (FMR) spectroscopy is a popular experimental technique, allowing to gain insight into the magnetization dynamics and therefore many characteristics of magnetic materials [58]. It is thus of interest to be able to replicate or predict FMR experimental data using micromagnetic simulations. As FMR describes a uniform mode with in-phase precession (c.f. Sec. 2.3), it is not necessary to resolve the magnet spatially to analyze it. Subsequently, it makes sense to utilize the table-output functionality of MuMax^3, where quantities are averaged over the entire lattice before being saved, thus saving both system memory and storage requirements. The algorithm used to obtain the spectra out of the output-table assumes that each entry (row in the table) has the current external magnetic field strength $\mu_0 H_{\text{ext}}$ saved in the column `B_stat`. The general algorithm is depicted as a flowchart in Fig. 3.4. However, it can technically be extended to work with any parameter in the output-table that allows to group the data in blocks to keep track of the sweep. First, all unique values `B` are extracted from the column `B_stat`. For each value `B`, the corresponding magnetization $m_i(t)$ is extracted ($i = \{x, y, z\}$ depending on the orientation of the excitation field), which is the average sample magnetization orientation over time for this specific value in the field sweep experiment. Note that t and all other variables in this case refer to discrete variables. In an optional step, the data $m_i(t)$ can now be interpolated (with, e.g., cubic splines), which is sensible especially if `tableautosave()` was used. To obtain the frequency-dependent magnetization $m_i(f)$, a fast-Fourier-transform (FFT) is performed on the data, before it is saved into a new array. The output of this loop thus gives a frequency and external field-dependent magnetization component $m_i(f, \mu_0 H_{\text{ext}})$, which cannot yet be directly compared to the experiment. As defined in Sec. 2.1, the magnetic susceptibility χ is the response function of a magnetic system to weak external perturbation. It can be obtained easily from the already calculated frequency-dependent magnetization via $\chi(f, \mu_0 H_{\text{ext}}) = \mathrm{d}m_i(f, \mu_0 H_{\text{ext}})/\mathrm{d}H_{\text{ext}}$ and allows insight into the dissipative and dispersive properties of a magnetic sample (c.f. Sec. 2.3). The susceptibility $\chi(f, \mu_0 H_{\text{ext}})$ can be then plotted as a color spectrum and be directly compared to experimental findings, as done e.g., by Zhou *et al.* in Ref. [59]. There, the numerically determined susceptibility $\chi(f, \mu_0 H_{\text{ext}})$ was used to compare the line shape of the numerical versus the experimentally determined absorption of microwaves into NiFi nano dots of various thicknesses [59]. The code developed for this thesis to obtain the dynamic susceptibility from the output-table is included in the Appendix B.2.1.
Since broadband FMR experiments are usually done using vector-network-analyzer (VNA) devices, a common experimental parameter used to present FMR data is the transmission parameter S_{21}. It was found that by remov-

ing the measurement background by the so-called derivative-divide method, the resulting spectrum $\mathrm{d_D}S_{21}$ is connected to the susceptibility via [57]

$$\mathrm{d_D}S_{21} \propto -if\frac{\mathrm{d}\chi}{\mathrm{d}f}. \tag{3.5}$$

Since it is used in many experimental works, most FMR spectra in this work will thus be presented using $|\mathrm{d_D}S_{21}|$. It should be noted that in cases where not only a dominant main mode is of interest, it makes sense to work with $\log_{10}|\mathrm{d_D}S_{21}|$, as the intensity of the dominant mode and other present modes in the spectrum is oftentimes several orders of magnitude (see Appendix A.1.1).

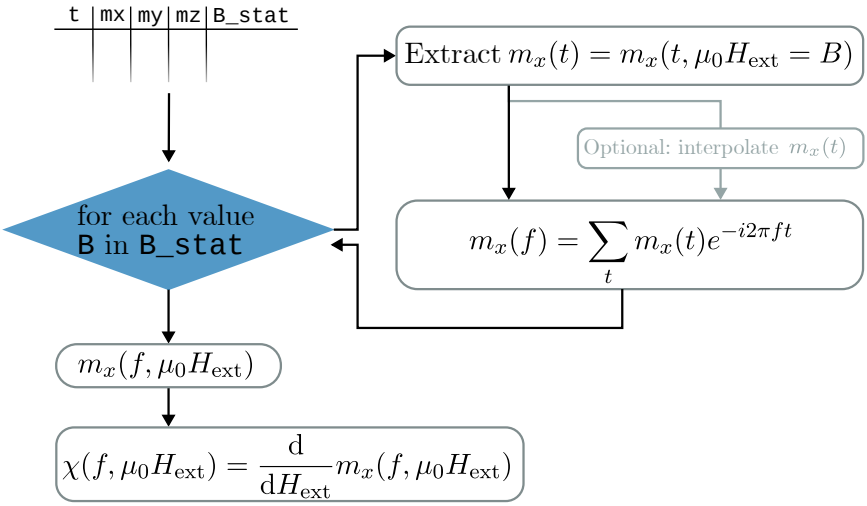

Figure 3.4: Flowchart depicting the general algorithm of obtaining the (dynamical) susceptibility $\chi(f, \mu_0 H_{\mathrm{ext}})$ from the output-table of a MuMax^3 field sweep simulation. The column `B_stat` in the table is used to group the output by the separate values of the external field, allowing to extract the time-dependent magnetization $m_i(t)$ for each simulation run, where $i = \{x, y, z\}$ denotes the direction of the external driving magnetic field. Optionally, $m_i(t)$ may be interpolated using cubic splines, as it allows to migitate artifacts that arise if the data was not sampled at the exact same point in time for each subsequent field value. In order to obtain the frequency-dependent magnetization, each $m_i(t)$ is fast-Fourier-transformed into $m_i(f)$. Finally, the susceptibility is recovered via $\chi(f, \mu_0 H_{\mathrm{ext}}) = \mathrm{d}m_i(f, \mu_0 H_{\mathrm{ext}})/\mathrm{d}H_{\mathrm{ext}}$. The dynamical susceptibility can then be either visualized directly as the FMR spectrum or processed into the derivative-divide transmission parameter $\mathrm{d_D}S_{21}$ using Eq. (3.5) to allow for more direct comparison to experimentally accessible quantities.

3.5.2 Spatial mode profiles

Upon examining ferromagnetic resonance (FMR) spectra, it is often ambiguous what the physical interpretation of the visible modes is, e.g., differentiating which

modes are edge-modes, Damon-Eshbach modes or Kittel modes. Micromagnetic simulations can provide valuable insight towards the proper physical interpretation of mode spectra by visualizing the spatial distribution of the power of the frequency-dependent magnetization. The resulting spatial mode profiles can be examined from each angle, but most commonly they are presented as two-dimensional color spectra in a top-down or front view of the sample to visualize the real space nature of a mode with fixed frequency [14, 60, 61]. The algorithm used to obtain these mode profiles is depicted as a flowchart in Fig. 3.5. Starting with importing the time- and space-dependent magnetization files, in a first step their spatial information gets averaged along the z-axis, as usually a top-down view is desired. This can, however, be changed for, e.g., a front- or side-view of the sample. Then, a loop iterates over the discrete space values (grid cell positions) x_i and y_i, effectively traversing over the 2D real-space grid and bringing the dynamical magnetization $\boldsymbol{m}(t, x_i, y_i)$ into frequency space using a FFT. The resulting $\boldsymbol{m}(f, x_i, y_i)$ replaces the previous time-dependent array slice in-place, as usually system memory is a big constraint for larger sample sizes. Finally, to obtain a power function $P(f, x_i, y_i)$ of frequency and real-space, the single components of the frequency-dependent magnetization are combined using a L^2 norm. Importantly, one can instead simply add up the complex phase of all three magnetization components and proceed normally in order to obtain a spacial phase profile of the dynamic magnetization. This resulting array can now be used to visualize certain mode profiles by using the corresponding array of frequencies f to identify the indices corresponding to the mode frequencies of interest. Usually, these mode frequencies can be determined via fitting of peaks f_p in FMR spectra at the current value of the external field $\mu_0 H_\mathrm{ext}$. Performing a numerical integration over the FWHM of the peak f_p then results in the spatial mode profile for the frequency f_p. The code developed for the analysis of spatial mode profiles is included in the Appendix B.2.5.

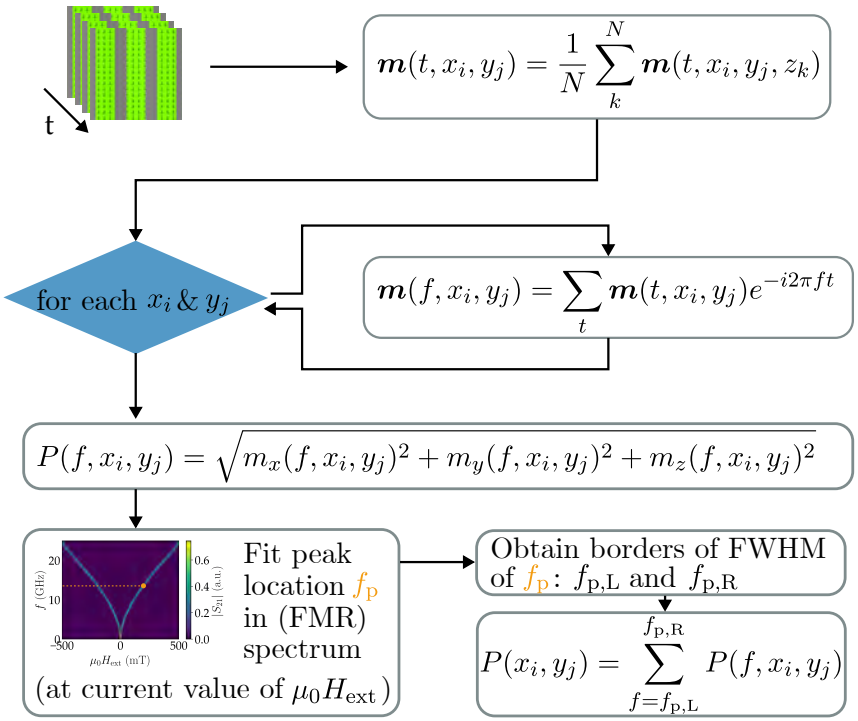

Figure 3.5: Flowchart depicting the algorithm for obtaining spacial mode profiles out of a MuMax^3 simulation. The spacial output files are loaded into memory and averaged over the z-axis to obtain $\boldsymbol{m}(t, x_i, y_j)$, since usually a top-down view of the sample is visualized . Then, for each "pixel" (x_i, y_j) the magnetization is brought into frequency space using a FFT. To obtain the mode power $P(f, x_i, y_j)$ as a function of frequency and space, the single magnetization components are combined via a L^2-norm. Note that in this step, alternatively the complex phase of the magnetization components can be added up to provide a spatial phase profile. To now display the profile for a mode visible in, e.g., a FMR spectrum, one must fit the peak location of interest, f_p, in the (separate) FMR simulation output. By numerically integrating over the full-width-half-maximum range (FWHM) of this peak, one receives the spacial mode profile for f_p.

3.5.3 Spin wave dispersion

Knowing how the dispersion of spin wave modes differ in various material systems (e.g., magnonic crystals) is important for both the fundamental understanding and the engineering of novel material systems [62]. Micromagnetic simulations can provide the spin wave dispersion spectra by following the procedure depicted in Fig. 3.6. Starting from loading in the spatially resolved magnetization output files of MuMax^3, a loop iterates over the grid coordinates perpendicular to the spin wave travel direction. Usually, the system is initialized in such a

way that the excitation will be along the x-direction, thus the loop will iterate over the perpendicular dimensions y and z. For each (y_j, z_k), a 2D fast-Fourier-transformation is applied on the x-component of the magnetization, bringing it into frequency and wave number domain $m_x^{y_j,z_k}(f,k_x)$. Here, the quantity $|m_x^{y_j,z_k}(f,k_x)|$ describes the dispersion along the x-direction for the coordinate pair (y_j, z_k). By summing over all (y_j, z_k), one subsequently obtains the total dispersion relation of the sample along x-direction by visualizing the power $P(f,k_x) = \log_{10}|m_x(f,k_x)|$, which is in units of dB. This method is well established in literature [44, 62, 63]. Code examples on how to obtain the spin wave dispersion from both the spatial magnetization output files and the region-wise ordered output table (in the following often referred to as "magnonic crystal approach") are included in the Appendix B.2.3 and B.2.4, respectively.

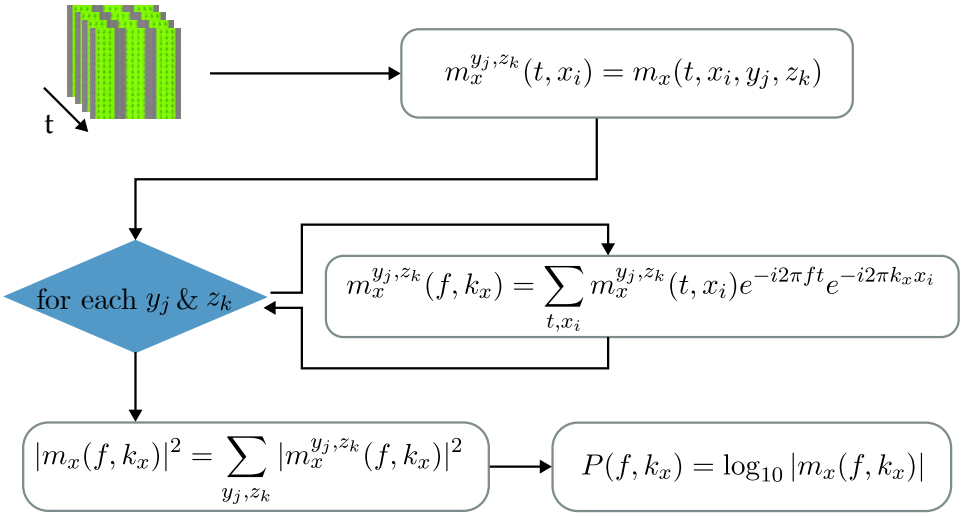

Figure 3.6: Illustration of the algorithm used to obtain spin wave dispersion spectra from MuMax^3 simulations. After loading the spatial magnetization output files in memory, a loop iterates over coordinate pairs (y_j,z_k), assuming that the propagation direction is along the x-axis. For each (y_j,z_k), a 2D FFT is applied to the x-component of the magnetization to transfer it into the frequency and wave number domain $m_x^{y_j,z_k}(f,k_x)$. Summing up the absolute values $|m_x^{y_j,z_k}(f,k_x)|$ for all (y_j,z_k) allows to obtain the total power $P(f,k_x)$ of a spin wave traveling along the x-direction in the sample, which can be visualized using a 2D color spectrum to show the dispersion.

3.5.4 Band structure

Upon moving to more complicated structures, such as, e.g., magnonic crystals, it is often desirable to visualize the systems band structure in order to observe

band gap closings or openings as done for example by Feilhauer *et al.* in the context of topological edge modes in magnonic crystals [64]. The procedure is similar to that of determining the spin wave dispersion in Sec. 3.5.3, however, extended to multi-dimensional wave vector spaces as illustrated in Fig. 3.7. The loaded spatially resolved magnetization data is again averaged over the z-dimension as a simplifying step, as most often dynamics along the z-axis are not of interest. Note this step is optional, as the workflow can analogously be expanded towards three-dimensional wave vector space. The averaged $\boldsymbol{m}(t, x_i, y_j)$ is then component-wise transferred into the frequency and wave number dependent $m_i(f, k_x, k_y)$ by using a 3D fast-Fourier-transformation. The absolute magnitude $|m(f, k_x, k_y)|$ is constituted by the absolute magnitudes of the single components. Now, two possible outputs are possible using $|m(f, k_x, k_y)|$. First, one can use this array to visualize a mode profile $P(f, k_x, k_y)$ for fixed frequency in momentum space, similarly to the one discussed in Sec. 3.5.2 for the real space case. Secondly, one can proceed to construct the band structure for a fixed succession of (high symmetry) points in reciprocal space, e.g., $\Gamma \to X \to M \to \Gamma$. This is done by traversing the 2D array of possible momenta (k_x, k_y) along the path in momentum space and saving the indices. The possible momenta are given by the numerically sampled momenta, controlled by the cell sizes and the total size of the simulation box. This is done using a slightly modified version of Bresenhams algorithm [65], originally designed to draw angled lines on a discrete pixel plane. By saving the index pairs along the path one can then extract the corresponding slices along the frequency axis from $|m(f, k_x, k_y)|$ and arrange them in order of the path $\Gamma \to X \to M \to \Gamma$, resulting in a 2D array $|m(f, k)|$. To now visualize the band structure, one only has to plot a color spectrum of the power $P(f, k) = \log_{10} |m(f, k)|$.

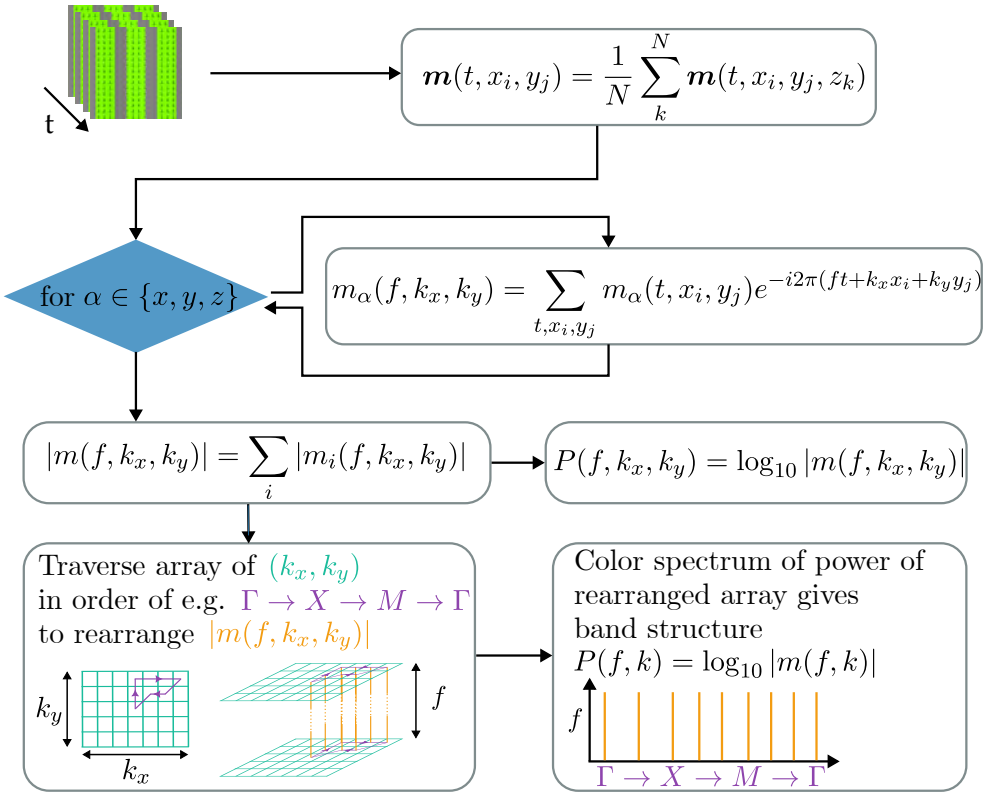

Figure 3.7: Algorithm used to obtain the (multi-dimensional) band structure from a MuMax^3 simulation. The output files containing the spatially resolved magnetization $\boldsymbol{m}(t, x_i, y_j, z_k)$ are loaded into system memory. Since most commonly the dynamics are considered in the x-y-plane, the data is averaged along the z-direction, which can be changed if necessary. Afterwards, the data is transferred into frequency f and wave number k space by applying a 3D FFT on each magnetization component, before summing up the absolute magnitude of each component to obtain $|m(f, k_x, k_y)|$. From here on, one can directly use a base 10 logarithm to plot a mode profile in momentum space, $P(f, k_y, k_z)$, similarly to the real space case. Alternatively, the band structure can be obtained by traversing over the array of discrete (k_x,k_y) (turquoise) along a fixed path (magenta) and saving the index pairs. Using these indices, one can construct the band structure by extracting the slices along the frequency axis in $|m(f, k_x, k_y)|$ and plotting them.

Chapter 4

Ferromagnetic nanogratings

Nanogratings, i.e., regular arrays of nanometer-sized ferromagnetic wires, have gained significant interest in the magnonics community due to their possible application in mediating unidirectional transport of spin waves via the chiral pumping mechanism [7, 10]. This chapter revolves around simulating the magnetic properties of nanogratings, with the goal of investigating how the mutual interaction between adjacent nanowires influences the collective behavior of the array in terms of its magnetostatic properties and spin wave transport characteristics. The knowledge gained can serve as a guide on how different grating design parameters may interfere with using the grating to construct unidirectional spin wave transport devices. For this purpose, Sec. 4.1 starts with discussing the differences emerging in ferromagnetic resonance (FMR) spectra for differently spaced but otherwise equal nanogratings, highlighting both the visible changes in the spectra alongside the physical interpretations of the modes. Extending this approach, in Sec. 4.2 we extract datapoints from simulated FMR data to determine the diagonal elements of the demagnetization tensor of the nanograting. This is done by fitting a modified Kittel equation, which can be used to give an estimate for the interaction range of the wires. Sec. 4.3 then discusses the influence of the inter-wire spacing on the spin wave dispersion across the grating, before the findings of this chapter are finally summarized in Sec. 4.4.

4.1 Ferromagnetic resonance

The Kittel mode of the nanogratings plays a central role in the mechanism of chiral pumping (c.f. Sec. 2.5.2), which is used to realize unidirectional spin wave propagation. Therefore, knowing how the Kittel mode changes for nanogratings of varying edge-to-edge spacings between neighboring wires presents vital information to design possible devices. By simulating a broad-band ferromagnetic resonance (FMR) experiment for different nanogratings, one can compare the Kittel modes of the nanogratings with each other and make conclusions about the inter-wire coupling and its impact on the respective Kittel mode. The material system studied in the following is a ferromagnetic $Co_{25}Fe_{75}$ (CoFe) nanograting,

using typical material parameters of $\mu_0 M_\mathrm{s} = 2.258\,\mathrm{T}$, $A_\mathrm{ex} = 2.6 \times 10^{-11}\,\mathrm{J/m}$ and $\alpha = 3.76 \times 10^{-3}$ [13, 66]. For the simulation of the nanogratings we use the "unit cell" shown in Fig. 4.1, with the simulation box (solid, black lines) consisting of infinitely long ferromagnetic wires/cuboids of width $w = 200\,\mathrm{nm}$ and height $h = 35\,\mathrm{nm}$, oriented along the y-direction and arranged periodically along the x-axis with a certain edge-to-edge spacing s_e2e between adjacent wires. The width of the simulation box along the x-axis is chosen such that three wires fit in it, with a respective distance of $s_\mathrm{e2e}/2$ from the outer wires to the borders of the box. In the Damon-Eshbach geometry, we apply a static external magnetic field $\boldsymbol{H}_\mathrm{ext}$ along the y-axis with a 1° offset, to account for experimental uncertainties regarding the exact orientation of $\boldsymbol{H}_\mathrm{ext}$ with respect to the nanograting [14] (for reference see Backward-Volume geometry in Appendix A.1.5). The magnetization of the individual wires is then saturated along the y-axis by the static magnetic field $\boldsymbol{H}_\mathrm{ext}$ (orange), before a dynamic driving magnetic field $\boldsymbol{h}_\mathrm{rf}$ (turquoise) is applied perpendicular to the wire magnetization in x-direction to excite the spin system within the grating. Specifically, a spatially homogeneous excitation field $\mu_0 h_\mathrm{rf}(t) = 1\,\mathrm{mT} \cdot \mathrm{sinc}(2\pi f_\mathrm{c}(t - t_0))$ is used, with a cut-off frequency $f_\mathrm{c} = 100\,\mathrm{GHz}$ and a pulse delay $t_0 = 50\,\mathrm{ps}$ (c.f. Sec. 3.3.3). For each external field value, the system is simulated for a total time of $T = 20\,\mathrm{ns}$, while sampling the (averaged) magnetization in $dt = 5\,\mathrm{ps}$ intervals.
This procedure is repeated for various different edge-to-edge spacings s_e2e to investigate the impact of the wire spacing on the Kittel mode of the nanograting. In Fig. 4.2, the resulting FMR spectrum is shown for six selected values of s_e2e, indicated by the sketch in the lower right-hand corner of each plot. Fig. 4.2 (a) and (b) show the case of $s_\mathrm{e2e} = 100\,\mathrm{nm}$ and $s_\mathrm{e2e} = 150\,\mathrm{nm}$, respectively. The spectra reveal three noticeably strong mode signals: the lowest frequency mode is considered the main mode (mode 0) due to its high intensity, with a slightly weaker second mode (mode 1) closely above it in frequency space. The third mode (mode 2) is separated from the first two by $\approx 10\,\mathrm{GHz}$ at zero magnetic field and is comparable to the second mode in terms of intensity. All three modes continue past the zero field before the wire magnetization switches due to the shape-anisotropy inducing a coercivity of $\mu_0 H_\mathrm{c} = -150\,\mathrm{mT}$. Upon direct comparing Fig. 4.2 (a) and (b), the mode 0 appears to move up to higher frequencies for $s_\mathrm{e2e} = 150\,\mathrm{nm}$ in (b). This trend continues for $s_\mathrm{e2e} = 200\,\mathrm{nm}$ in Fig. 4.2 (c), where the intense mode 0 seems to cross mode 1 in the magnetic field range between $\mu_0 H_\mathrm{ext} = 0\,\mathrm{mT}$ and $\mu_0 H_\mathrm{ext} = -75\,\mathrm{mT}$. This is especially visible upon comparing the spectra in Fig. 4.2 (a), (b) and (c) at field values $\mu_0 H_\mathrm{ext} \approx -145\,\mathrm{mT}$, shortly before the magnetization reversal. When slightly increasing the spacing to $s_\mathrm{e2e} = 250\,\mathrm{nm}$ in Fig. 4.2 (d), mode 0 continues to push upwards in frequency, while mode 1 remains fixed. Further enlarging s_e2e in bigger steps to $s_\mathrm{e2e} = 450\,\mathrm{nm}$ in Fig. 4.2 (e) and $s_\mathrm{e2e} = 900\,\mathrm{nm}$ in (f)

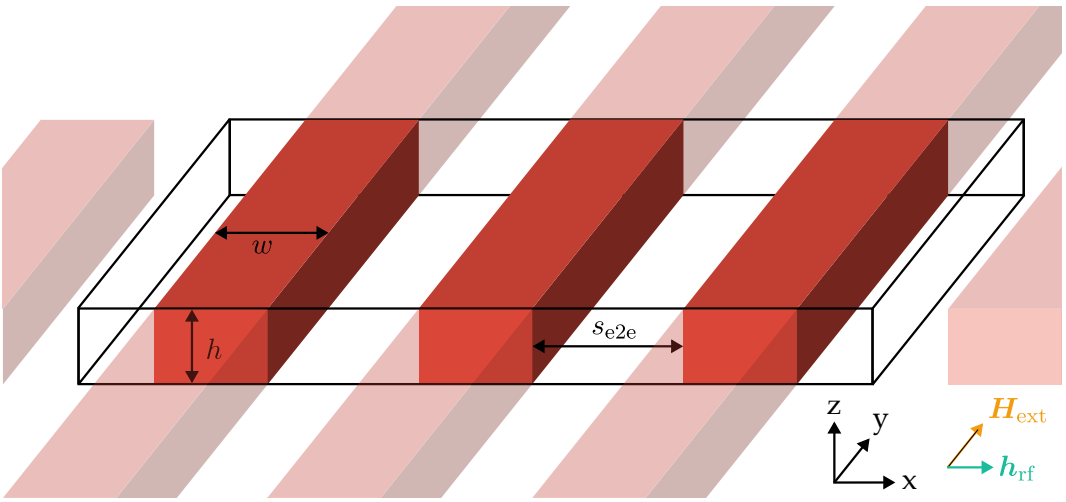

Figure 4.1: Schematic illustration of a model system simulating the ferromagnetic resonance (FMR) response of a nanograting. The simulation box (black lines) is designed as a "unit cell", meaning it can be extended easily to simulate larger samples by using periodic boundary conditions (pale red wires) in the in-plane directions x and y. In the box, three ferromagnetic wires of width w and height h are arranged in a grating along the y-axis, with an edge-to-edge spacing s_{e2e} between neighboring wires. The width of the simulation box along the x-axis is chosen such that three wires fit in it with a distance of $s_{e2e}/2$ from the outer wires to the boundary of the box. The height of the simulation box is always simply given by the height of the grating to avoid unnecessary computation cost. To saturate the ferromagnetic sample, a static external magnetic field $\boldsymbol{H}_{ext}$ (orange) is applied along the y-axis with a 1°-offset to account for experimental uncertainties. Excitation is provided via the dynamic driving magnetic field $\boldsymbol{h}_{rf}$ (turquoise) applied along the x-axis.

shows that the shift to higher frequencies of mode 0 saturates, as both spectra show almost no visible difference amongst each other. All in all, the results in Fig. 4.2 suggest that for edge-to-edge spacings smaller than the width of the individual wires, i.e., $s_{e2e} < w$, the main mode (mode 0) pushes upwards in frequency. For spacings comparable to the wire width ($s_{e2e} \approx w$), mode 0 appears to cross the first higher mode (mode 1). This upwards trend, however, ceases for spacings larger than the width ($s_{e2e} > w$) with only small differences visible between $s_{e2e} = 250\,\text{nm}$ and $s_{e2e} = 450\,\text{nm}$ and no visible differences between $s_{e2e} = 450\,\text{nm}$ and $s_{e2e} = 900\,\text{nm}$.

In order to further discuss the results of Fig. 4.2, it is vital to understand the physical interpretation of the modes visible in the spectra. This allows to confirm the apparent mode crossing and rule out alternative scenarios, e.g., an anti-crossing or avoided crossing of the modes. This can be done by visualizing the spatial mode profile for each mode at a given external field strength. Fig. 4.3 shows the spatial profile of the three modes of interest for $s_{e2e} = 100\,\text{nm}$ at

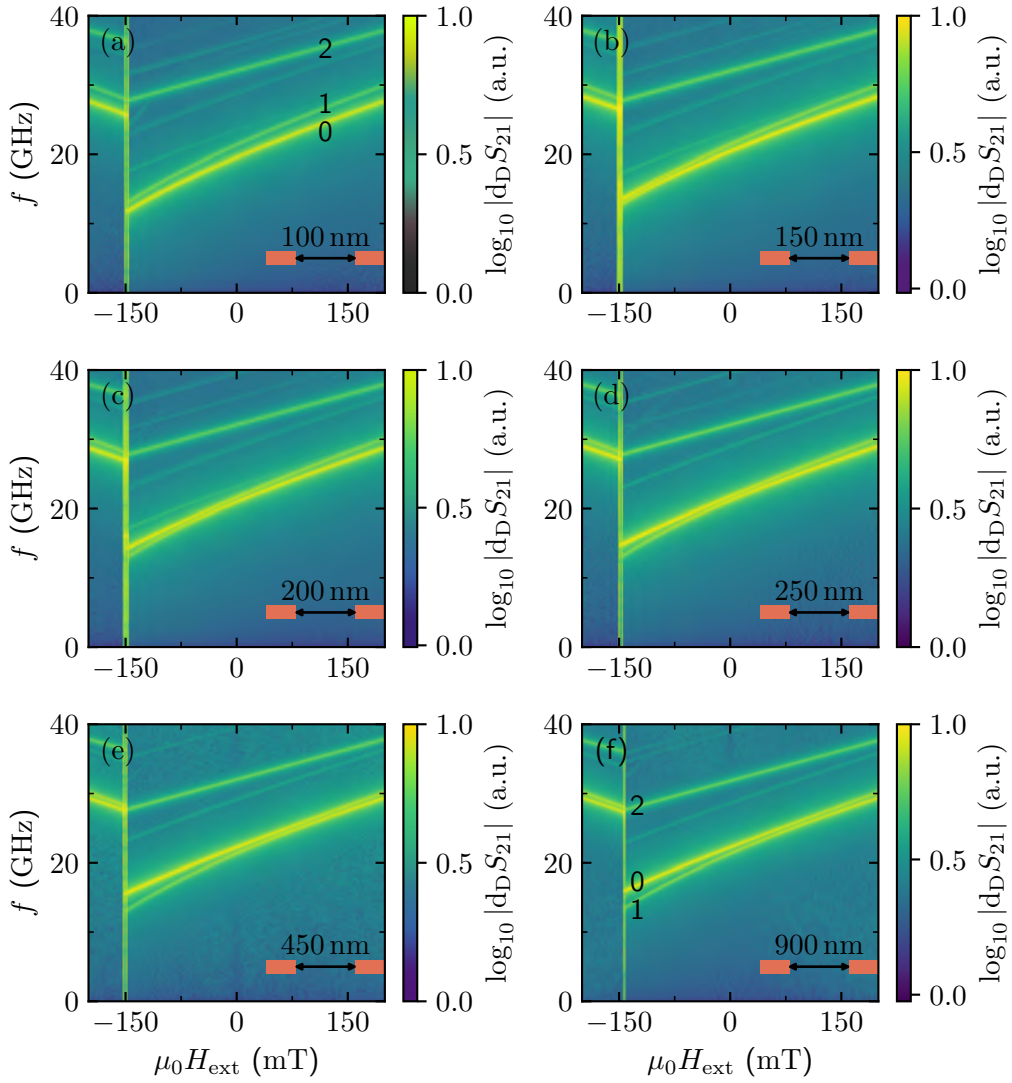

Figure 4.2: Results of the ferromagnetic resonance (FMR) simulation of nanogratings consisting of wires of width $w = 200\,\mathrm{nm}$ and height $h = 35\,\mathrm{nm}$ for various edge-to-edge spacings s_{e2e} (indicated by the sketch in the lower right-hand corner of the respective spectrum). In all spectra, three modes are of interest: the high intensity mode 0 and two less intense higher frequency modes (mode 1 and mode 2), as labeled in (a) and (f). **(a) - (b)** For cases $s_{\mathrm{e2e}} < w$, the main mode (mode 0) is below mode 1 in frequency but appears to be shifting upwards in frequency for increasing s_{e2e}. In **(c)** and **(d)**, mode 0 appears to cross mode 1 in the magnetic field range from $\mu_0 H_{\mathrm{ext}} = -75\,\mathrm{mT}$ to $\mu_0 H_{\mathrm{ext}} = 0\,\mathrm{mT}$. For larger spacings, shown in **(e)** and **(f)**, the spectra differ only marginally, indicating that the frequency shift of the main mode (mode 0) saturates for grid spacings larger than the wire width ($s_{\mathrm{e2e}} > w$).

$\mu_0 H_{\text{ext}} = -75\,\text{mT}$. In Fig. 4.3 (a), the three fitted mode peaks are indicated by cross marks in the FMR spectrum. Fig. 4.3 (b)-(d) then show the spatial mode profiles from a top-down (color spectrum) and a front view (inset) of the sample in order of increasing frequencies. The color coding allows to connect (b)-(d) to the marked fitting points in the FMR data presented in (a). It can be seen that the high intensity mode (mode 0), located at $f_0 = (16.1300 \pm 0.0004)\,\text{GHz}$ (orange) in Fig. 4.3 (b), has a quasi-uniform profile across the wires, only falling off at the wire edges. This allows mode 0 to be identified as the Kittel mode of the nanograting. The observed fall off in intensity upon approaching the wire edges can be explained by the stray fields at the edges locally preventing uniform precession [14]. The power spectra of mode 1 and mode 2 located at $f_1 = (17.740 \pm 0.025)\,\text{GHz}$ (purple) and at $f_2 = (30.04 \pm 0.04)\,\text{GHz}$ (dark blue) are shown in Fig. 4.3 (c) and (d), respectively Both exhibit a non-uniform mode profile across the wires. Examining the front view of the structure (insets) reveals that both modes are Damon-Eshbach modes of different orders, as their wave vectors are perpendicular to the magnetization, which is oriented along the wires. Furthermore, both modes possess odd wave numbers, as overall only odd wave numbers appear in this simulation due to the spatially uniform excitation field [14]. The analysis of the spatial mode profiles in Fig. 4.3 subsequently reveals that the highest intensity mode (mode 0) is the nanogratings Kittel mode, whereas the higher order modes (mode 1 and mode 2) are Damon-Eshbach modes with odd wave numbers.

Furthermore, the findings of Fig. 4.3 are now compared to the exact same mode profile analysis applied to a larger spacing $s_{\text{e2e}} = 250\,\text{nm}$ in Fig. 4.4. This comparison confirms the previously made assumption of a mode crossing between the nanogratings Kittel mode (mode 0) and the lowest order Damon-Eshbach mode (mode 1). The quasi-uniform Kittel mode in Fig. 4.4 (c) is located at a higher frequency $f_0' = (18.4500 \pm 0.0004)\,\text{GHz}$ than the Damon-Eshbach mode in (b) at $f_1' = (17.560 \pm 0.004)\,\text{GHz}$ contrary to the previous findings for a smaller grating spacing in Fig. 4.3. This is proof that the modes cross for smaller s_{e2e} distances with $s_{\text{e2e}} = 100\,\text{nm} < w$ in Fig. 4.2 (a) and $s_{\text{e2e}} = 250\,\text{nm} > w$ in Fig. 4.2 (d). Consequently, in the negative field range, where chiral pumping is expected, the Kittel mode is not necessarily the lowest frequency excitation of the grating.

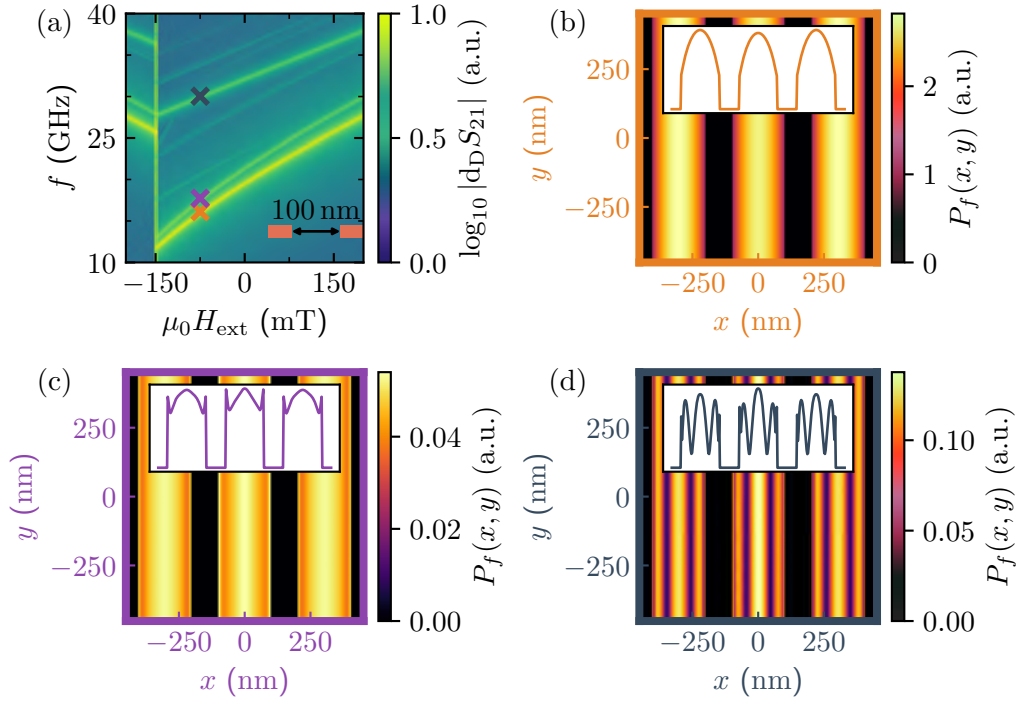

Figure 4.3: Spatial mode profiles for a ferromagnetic resonance (FMR) simulation of a nanograting consisting of wires of width $w = 200\,\text{nm}$ and height $h = 35\,\text{nm}$, arranged with an edge-to-edge spacing of $s_{\text{e2e}} = 100\,\text{nm}$. **(a)** FMR spectrum with color-coded cross marks indicating the location of modes fitted at $\mu_0 H_{\text{ext}} = -75\,\text{mT}$. **(b)** The spatial mode profile of the highest intensity mode, fitted at $f_0 = (16.1300 \pm 0.0004)\,\text{GHz}$, shows a quasi-uniform distribution of power across the individual wires, identifying it as the Kittel mode of the nanograting. **(c)** For the less intense second mode at $f_1 = (17.740 \pm 0.025)\,\text{GHz}$, a non-uniform profile across the wires identifies this mode as a Damon-Eshbach mode, due to the wave vector being perpendicular to the wire magnetization. The frontal view in the inset further shows that this mode has an odd wave-number. **(d)** The third mode, located at $f_2 = (30.04 \pm 0.04)\,\text{GHz}$, is classified as the next higher-order Damon-Eshbach mode exhibitin an odd wave number, analogous to (c).

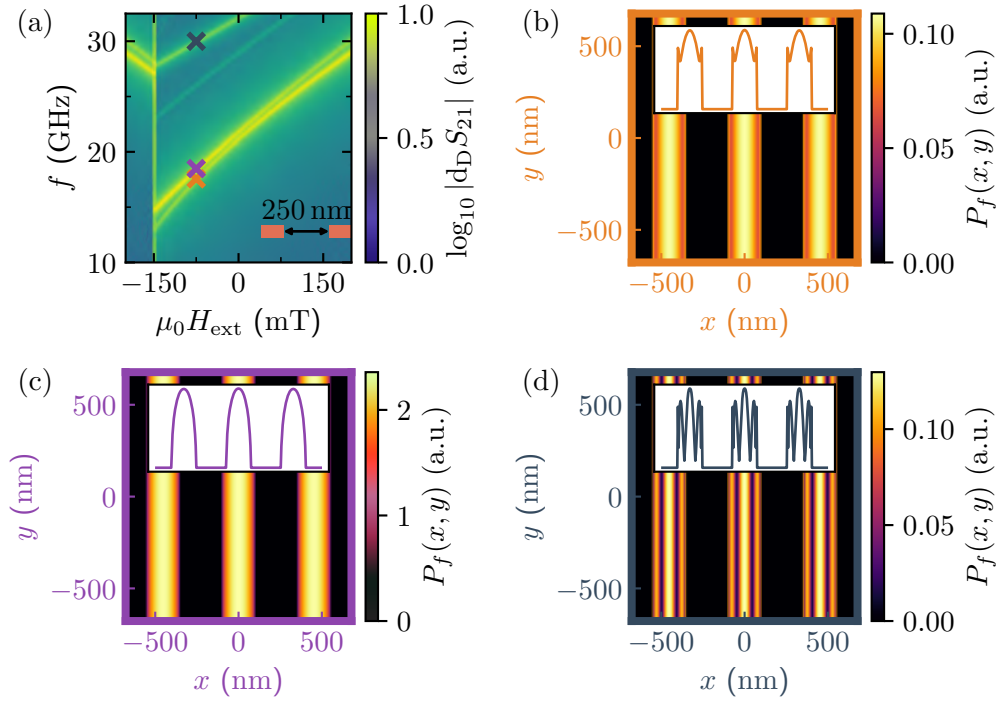

Figure 4.4: Spatial mode profiles for a ferromagnetic resonance (FMR) simulation of a nanograting consisting of wires of width $w = 200\,\mathrm{nm}$ and height $h = 35\,\mathrm{nm}$ arranged with an edge-to-edge spacing of $s_{\mathrm{e2e}} = 250\,\mathrm{nm}$. These mode profiles allow to confirm the mode crossing of the Kittel and the lower order Damon-Eshbach mode of the nanograting, when compared to the smaller spacing $s_{\mathrm{e2e}} = 100\,\mathrm{nm}$ in Fig. 4.3. **(a)** FMR spectrum with color-coded cross marks, indicating the location of modes fitted at $\mu_0 H_{\mathrm{ext}} = -75\,\mathrm{mT}$. **(b)** The spatial non-uniformity of the mode profile allows to identify this mode as a Damon-Eshbach mode with an odd wave number at $f_1' = (17.560 \pm 0.004)\,\mathrm{GHz}$. **(c)** The quasi-uniform Kittel mode of the nanograting is located at a higher frequency $f_0' = (18.4500 \pm 0.0004)\,\mathrm{GHz}$ than the lowest present Damon-Eshbach mode. **(d)** The third mode, next higher-order Damon-Eshbach mode, located at $f_2' = (29.99 \pm 0.18)\,\mathrm{GHz}$ is equivalent to the case of the results of the grating presented in Fig. 4.3 with $s_{\mathrm{e2e}} = 100\,\mathrm{nm}$.

4.2 Influence of wire spacing on inter-wire coupling

Apart from the (visual) differences in the spectra due to the frequency shift of the Kittel mode as a function of the edge-to-edge distance s_{e2e} between the wires discussed in Sec. 4.1, the simulated ferromagnetic resonance (FMR) spectra also allow to quantify the range of the mutual dipole-coupling between individual wires. By gradually increasing s_{e2e} for otherwise fixed grating parameters, the system slowly transitions from a continuous thin film ($s_{\mathrm{e2e}} = 0$) towards the limit of a single, isolated ferromagnetic wire ($s_{\mathrm{e2e}} \to \infty$). Evaluating the Kittel mode and thus the resulting diagonal elements of the demagnetization tensor for each spacing allows us to deduce the coupling regime with regards to s_{e2e}, as we can compare the obtained diagonal demagnetization tensor elements to the analytical solutions for a single wire.
The simulation procedure for each value of s_{e2e} is equal to the model presented in Sec. 4.1: individual wires of fixed width $w = 200\,\mathrm{nm}$ and height $h = 35\,\mathrm{nm}$ are arranged in a three wire unit cell with edge-to-edge spacing s_{e2e}, as illustrated in Fig. 4.1. The collection of FMR spectra evaluated in this section is included in the Appendix A.1.4 In order to compare the Kittel modes beyond visual differences, a finite number of points is extracted from the resulting FMR spectrum, as exemplarily shown for the case of $s_{\mathrm{e2e}} = 150\,\mathrm{nm}$ in Fig. 4.5 (a). By extracting modes from a specified number of line slices along the frequency (f) axis, one can fit each slice as a sum of Lorentzians (c.f. Sec. 2.3). Since it was established in Sec. 4.1 that the dominant mode in the FMR spectra is the Kittel mode of the grating, one simply takes the fitted peak location f_{peak} of the Lorentzian with highest intensity as the Kittel frequency at the current field value. For details of the implementation of fitting a FMR spectrum, see the example code in the Appendix B.2.2. These frequencies f_{peak} are indicated by black markers superimposed over the spectrum in Fig. 4.5 (a). In a second step, one can then fit a modified Kittel equation, given as

$$f'_{\mathrm{res}} = \frac{\gamma\mu_0}{2\pi}\sqrt{[H_{\mathrm{ext}} + a \cdot M_{\mathrm{s}}] \cdot [H_{\mathrm{ext}} + b \cdot M_{\mathrm{s}}]} \tag{4.1}$$

with $a = (N_{xx} - N_{zz})$ and $b = (N_{yy} - N_{zz})$, to the extracted data points, as shown in Fig. 4.5 (b). By utilizing Eq. (2.12), one obtains the fitted demagnetization factors N_{xx}, N_{yy} and N_{zz} for the current spacing s_{e2e} by solving a simple system of equations.

Fig. 4.6 displays the fitted values for N_{xx} (red), N_{yy} (blue) and N_{zz} (green) for increasing edge-to-edge spacing s_{e2e} in units of the wire width w. The analytical values of the demagnetization factors in the limit of a single wire (c.f. Eq. (2.13)) are shown as straight horizontal lines in the corresponding color, with the shaded

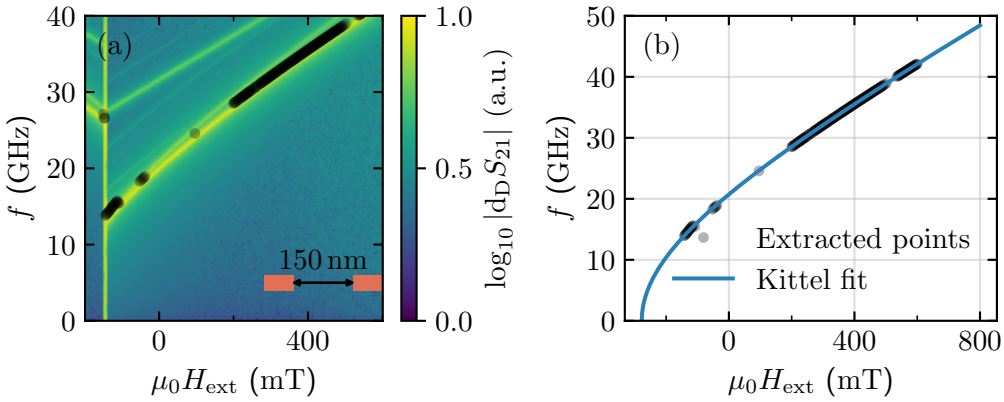

Figure 4.5: Approach for fitting the Kittel equation to a simulated ferromagnetic resonance (FMR) spectrum, exemplarily shown for an edge-to-edge spacing $s_{\mathrm{e2e}} = 150\,\mathrm{nm}$. **(a)** Simulated FMR spectrum with the extracted data points indicated by black dots. The data points are obtained by fitting the amplitude $\mathrm{d_D} S_{21}$ at a fixed magnetic field value $\mu_0 H_{\mathrm{ext}}$ using a sum of Lorentzians. Since the Kittel mode has the strongest intensity, its frequency location is determined as the peak of the Lorentzian with highest magnitude. As visible in the spectrum, this method is not applicable in frequency regions containing mode crossings, as there both modes have approximately the same intensity. **(b)** The data points extracted from (a) are fitted to the Kittel equation. Commonly, a modified version (Eq. (4.1)) is used to increase fitting accuracy by only having two instead of three fitting parameters.

area indicating a 5% deviation as a guide to the eye. For the continuous thin film ($s_{\mathrm{e2e}} = 0$), we recover the expected $N_{zz} = 1$ and $N_{xx} = N_{yy} = 0$. Increasing s_{e2e} in small increments initially shows N_{xx} and N_{yy} converging rather quickly towards the analytical expression of a single wire, however, tapering off between $s_{\mathrm{e2e}} = 1w$ and $s_{\mathrm{e2e}} = 1.5w$. For larger spacings, the fitted values only converge slowly towards the analytical result. At around $s_{\mathrm{e2e}} = 0.85w$, one data point appears to be an outlier, being much closer to the single wire limit than surrounding points. This can be explained by the mode crossing between the Kittel and Damon-Eshbach mode discussed in Sec. 4.1, which is located roughly at this value. At $s_{\mathrm{e2e}} = 6w$, N_{xx} and N_{yy} are steadily within 5% of the single wire limit. N_{zz} on the other hand appears to not converge towards the analytical value at all, remaining at a mean value of $N_{zz} = (0.0026 \pm 0.0050)$. This allows to approximate $N_{zz} \approx 0$. Upon assuming $N_{zz} = 0$ and only using N_{xx} and N_{yy} as free fitting parameters, one recovers the same result as presented in Fig. 4.6 for N_{xx}/N_{yy} as a function of the wire spacing s_{e2e}. All in all, the data in Fig. 4.6 point towards sizable dipole-coupling between the individual wires of the grating for edge-to-edge spacings $s_{\mathrm{e2e}} \leq 1.5w$, leading to collective modes rather than excitations of the individual wires. This result agrees well with previously

established values for the interaction range in literature, determined by both experimental and analytical methods [67–71].

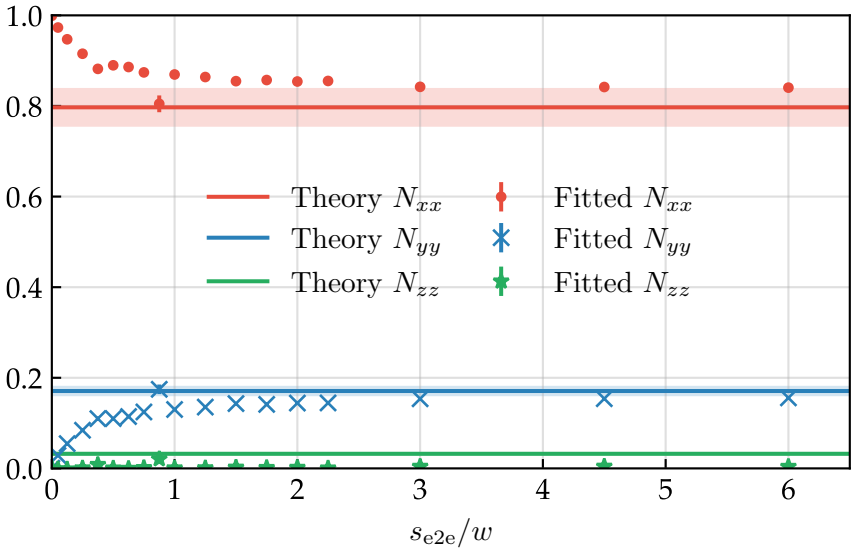

Figure 4.6: Resulting demagnetization factors N_{xx} (red), N_{yy} (blue) and N_{zz} (green) from fitting the modified Kittel equation (4.1) to the simulated ferromagnetic resonance spectra of the nanogratings. This figure partially shows the transition from a continuous thin film ($s_{e2e} = 0$) towards the limit of a single wire ($s_{e2e} \to \infty$). The edge-to-edge spacing s_{e2e} is presented in units of the constant wire width $w = 200\,\text{nm}$. The analytical results for a single ferromagnetic wire are shown as horizontal lines of corresponding color, with the shaded area marking a 5% deviation. For $s_{e2e} = 0$, the expected result for the ferromagnetic thin film is recovered: $N_{zz} = 1$ and $N_{xx} = N_{yy} = 0$. Upon increasing the wire spacing s_{e2e}, the demagnetization factors converge strongly towards the analytical limit, but start to saturate between $s_{e2e} = 1w$ and $s_{e2e} = 1.5w$. For large wire separation $s_{e2e} = 6w$, N_{xx} and N_{yy} are both steadily converged within 5% of the single wire limit, whereas N_{zz} is well approximated as $N_{zz} \approx 0$ without significant impact on the results. Subsequently, for spacings $s_{e2e} \leq 1.5w$ a strong dipole-coupling is present between the wires, inducing a collective mode of the nanograting rather than individual wire modes.

4.3 Spin wave dispersion

Apart from studying the resonant behavior of nanograting structures, one can also investigate their spin wave transport properties by simulating the dispersion relation. For this purpose, a simulation model with a unit cell containing 99 individual nanowires and no periodicity along the x-direction is used. Each wire has a width $w = 200\,\mathrm{nm}$ and height $h = 20\,\mathrm{nm}$. By utilizing this modified simulation box, one can effectively simulate large spin wave travel distances of order $10\,\mu\mathrm{m}$ along the x-direction, while restricting the simulation box in the transverse directions to conserve memory and calculation power. In order to excite spin waves, the system is first relaxed with an external field $\mu_0 H_{\mathrm{ext}} = 50\,\mathrm{mT}$ applied along the wire direction (i.e., the y-axis). Then, a spatially and temporally sinc-shaped excitation field $\mu_0 h_{\mathrm{rf}} = 1\,\mathrm{mT} \cdot \mathrm{sinc}(k_{\mathrm{c}}(x - x_0)) \cdot \mathrm{sinc}(2\pi f_{\mathrm{c}}(t - t_0))$ is applied along the x-axis, transverse to the grating. The excitation parameters are $k_{\mathrm{c}} = 500 \cdot 2\pi/l_x$, $f_{\mathrm{c}} = 100\,\mathrm{GHz}$ and $t_0 = 50\,\mathrm{ps}$, while choosing $x_0 = 0$ to center the excitation in the sample middle. The parameter l_x hereby describes the length of the simulation box along the x-axis (c.f. Fig. 4.1).
In Fig. 4.7, the spin wave dispersion along the x-axis is depicted for several different edge-to-edge spacings s_{e2e}, which in turn leads to varying center-to-center distances $a = s_{\mathrm{e2e}} + w$ (indicated by the sketch in the lower right-hand corner of each plot). Each spectrum was created by interpreting the nanograting as a one-dimensional magnonic crystal, treating the individual wires as lattice sites by considering only their averaged magnetization. Effectively, this computational trick reduces the system to a 1D-chain of lattice sites, separated by the center-to-center spacing a of the wires. Fig. 4.7 (a) depicts the dispersion spectrum of a continuous thin film ($s_{\mathrm{e2e}} = 0\,\mathrm{nm}$). The reduced zone scheme matches the expectation for the excitation of Damon-Eshbach spin waves in a ferromagnetic thin film, as shown by the reasonable agreement to the previously derived Kalinikos-Slavin equation (2.31), which is included in (a) as a red dashed line. Upon introducing a finite spacing $s_{\mathrm{e2e}} = 5\,\mathrm{nm}$ in Fig. 4.7 (b), a gap opens at the Brillouin zone boundaries between the first and second excitation band. Furthermore, the higher bands of the reduced zone scheme already appear to flatten considerably. Increasing the spacing to $s_{\mathrm{e2e}} = 50\,\mathrm{nm}$ and $s_{\mathrm{e2e}} = 150\,\mathrm{nm}$ in Fig. 4.7 (c) and (d), respectively, flattens the lowest band from an initial width of $\approx 14\,\mathrm{GHz}$ in (a) to a respective bandwidth of $\approx 5\,\mathrm{GHz}$ in (c) and $\approx 2\,\mathrm{GHz}$ in (d). In contrast, for even larger spacings $s_{\mathrm{e2e}} = 200\,\mathrm{nm}$ and $s_{\mathrm{e2e}} = 350\,\mathrm{nm}$, presented in Fig. 4.7 (e) and (f), respectively, the lowest band flattens only marginally. In Fig. 4.7 (e), the upper bands appear to be almost horizontal, whereas for the lowest band the bandwidth seems to remain at $\approx 2\,\mathrm{GHz}$.
The results depicted in Fig. 4.7 (b) and (c) suggest that nanogratings exhibit transport properties of one-dimensional magnonic crystals for small edge-to-edge

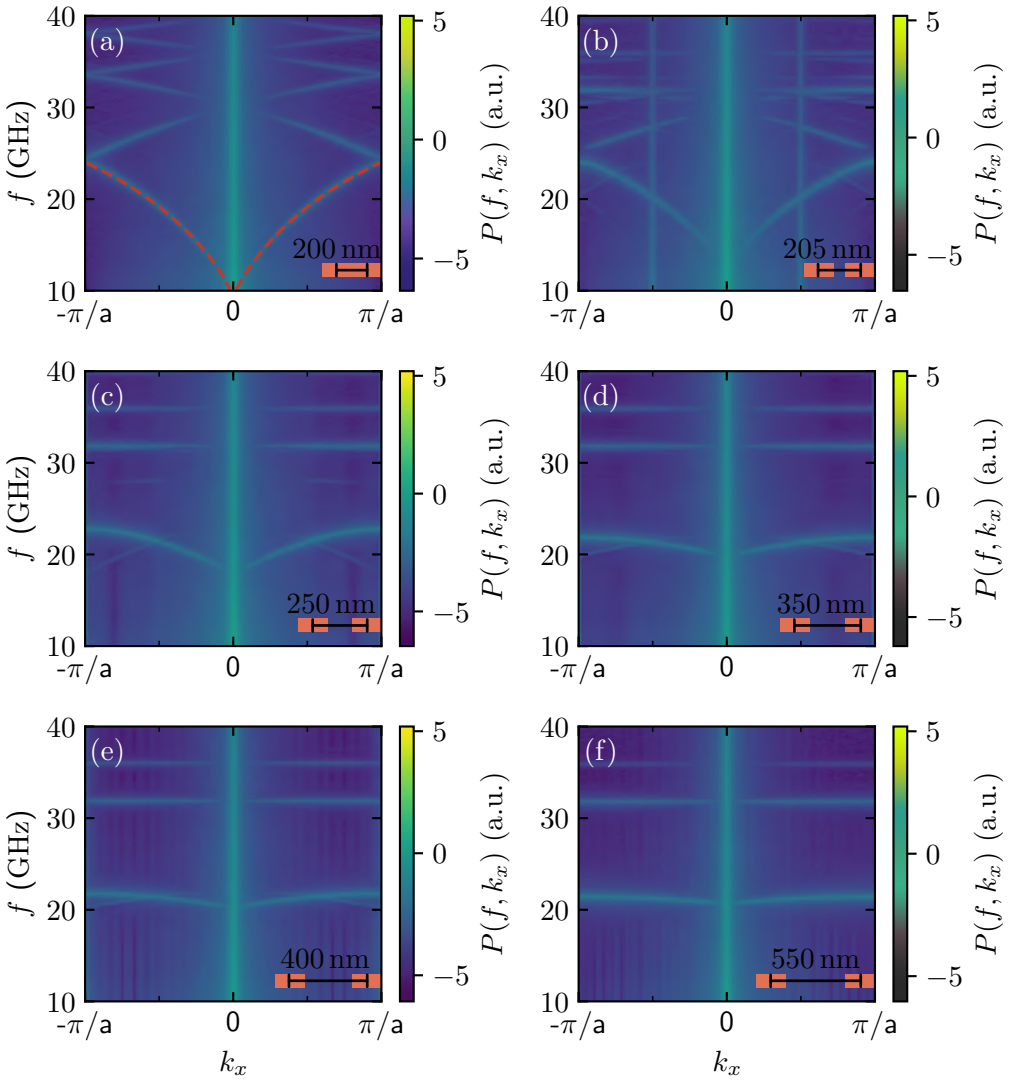

Figure 4.7: Dispersion spectra of CoFe nanogratings of varying edge-to-edge spacing s_{e2e}, resulting in different center-to-center spacings $a = s_{\mathrm{e2e}} + w = s_{\mathrm{e2e}} + 200\,\mathrm{nm}$, as indicated by the sketch in the lower right-hand corner of each spectrum. **(a)** For the case of a continuous thin film ($s_{\mathrm{e2e}} = 0$) the expected reduced zone scheme for the excitation of Damon-Eshbach spin waves is recovered. As a guide to the eye, the analytic result of the Kalinikos-Slavin equation (2.31) is shown as a red dashed line, agreeing well with the simulation data. **(b)** A small inter-wire spacing $s_{\mathrm{e2e}} = 5\,\mathrm{nm}$ opens a band gap at the Brillouin zone boundary between the first and second band, while the higher order bands are already flattened strongly. **(c)** At $s_{\mathrm{e2e}} = 50\,\mathrm{nm}$, the lowest band flattens from a band width of initially $\approx 14\,\mathrm{GHz}$ in (a) to around $\approx 5\,\mathrm{GHz}$. **(d)** - **(f)** For even larger spacings $s_{\mathrm{e2e}} = 150\,\mathrm{nm}$ to $s_{\mathrm{e2e}} = 350\,\mathrm{nm}$ only marginal changes are observed in the dispersion, with the lowest band flattening to a bandwidth of $\approx 2\,\mathrm{GHz}$ in (f).

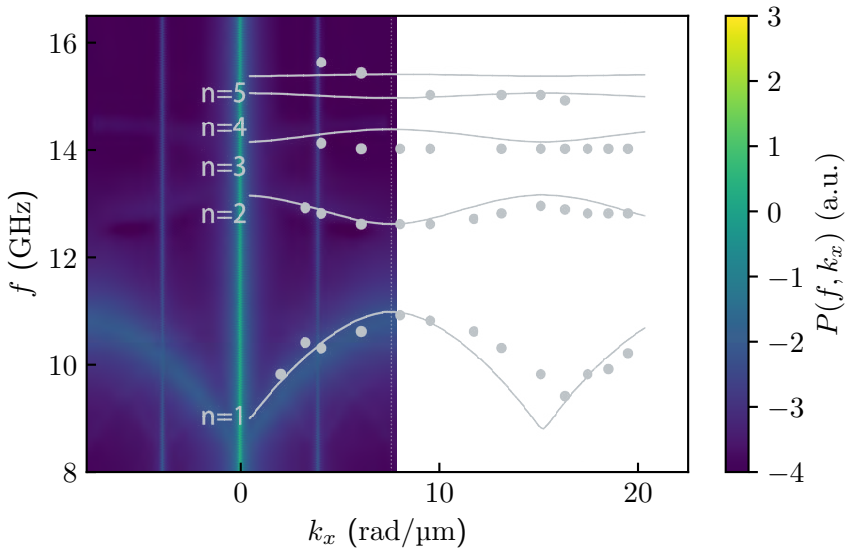

Figure 4.8: Dispersion spectrum of an array of $Ni_{80}Fe_{20}$ nanowires of width $w = 350\,\mathrm{nm}$, height $h = 30\,\mathrm{nm}$ and edge-to-edge spacing $s_{e2e} = 55\,\mathrm{nm}$. The simulation data shown as a colormap is in reasonable agreement to both analytical considerations (gray lines) and experimental data (gray dots) previously published by Giubbotti *et al.* [72]. This confirms the validity of the presented calculation method for the dispersion of nanogratings.

spacings. This finding was first reported by Gubbiotti *et al.* [72] and confirmed using both theoretical and experimental data. In order to validate the approach developed in this section for the simulation of spin wave dispersions, we simulate the material system used in Ref. [72], consisting of an array of $Ni_{80}Fe_{20}$ nanowires ($M_s = 800\,\mathrm{kA/m}$, $A_{ex} = 13\,\mathrm{pJ/m}$ and $\alpha = 0.01$ [14, 55]) of width $w = 350\,\mathrm{nm}$, height $h = 30\,\mathrm{nm}$ and edge-to-edge spacing $s_{e2e} = 55\,\mathrm{nm}$. Fig. 4.8 depicts the simulation results as a color spectrum. Additionally, the analytical (gray lines) and experimental (gray dots) data of Gubbiotti *et al.* [72] is included in Fig. 4.8, showing decent agreement with the simulation.

4.4 Summary

In conclusion, the investigation of ferromagnetic nanogratings (c.f. Fig. 4.1) in this chapter has yielded insight into three main points of consideration with respect to their potential usage as local transducers for chiral pumping. First, the study of the ferromagnetic resonance (FMR) for nanogratings of different wire spacings in Sec. 4.1 showed that for large inter-wire distances the Kittel mode

is no longer the lowest frequency excitation of the grating (c.f. Fig. 4.2). This observation is of particular relevance as the dynamic dipole field induced by the nanogratings Kittel mode is crucial to realize non-reciprocal spin wave transport in the theoretical framework of chiral pumping (c.f. Sec. 2.5.2). Furthermore, analyzing the mutual coupling range via fitting the Kittel equation to the FMR spectra of gratings with various spacings showed an upper bound for the dipole-interaction regime of $s_{\mathrm{e2e}} \leq 1.5w$, where s_{e2e} is the edge-to-edge spacing and w the width of a single wire of the grating (c.f. Fig. 4.6). This observation is in accordance with estimates derived from both analytical calculations and experiments. Since the theoretical description of chiral pumping is based on the assumption of negligible inter-wire dipole-interactions, this bound serves as an important design parameter for experimental realizations. Finally, by analyzing the spin wave dispersion of Damon-Eshbach modes traveling across the nanograting in Sec. 4.3, two conclusions can be made. Firstly, the nanograting can be treated as a one-dimensional magnonic crystal, which allows for precise calculations of the dispersion relation and is confirmed by its agreement with both experimental and analytical dispersions of nanogratings (c.f. Fig. 4.8). Secondly, the dispersion is flattened by increasing the inter-wire edge-to-edge spacing s_{e2e}, leading to an opening of band gaps at the Brillouin-zone boundaries (c.f. Fig. 4.7). This showed that for small wire spacings a considerable spin wave transport is possible across the grating without an adjacent spin wave medium.

Chapter 5

Anti-ferromagnetic order in alternating ferromagnetic nanogratings

Apart from the so-far discussed homogeneous nanogratings, alternating nanowire arrays have gained attention in literature due to several peculiarities. Initially, it has been found that in arrays of alternating Co/$Ni_{80}Fe_{20}$ nanowires, the hysteresis curve of the grating displays two distinct switching fields, caused by the different magnetic coercive fields of the different material compositions [73]. This results in a state of anti-parallel alignment or anti-ferromagnetic order (AFO) between the two wire type sub-lattices in a specific magnetic field range [73]. Apart from the wire material, i.e., the saturation magnetization, also the physical dimensions of the wires influence their magnetic coercive fields via the shape anisotropy (see Sec. 2.2.1). Therefore, by alternating not the wire material but the width of adjacent wires, it has been found that the two-step magnetization reversal is also visible in hysteresis curves recorded for material-wise uniform $Ni_{80}Fe_{20}$ nanogratings with alternating wire widths [67, 74]. In magnetostatically coupled alternating width nanowire arrays (AWNAs), the desired magnetic state of the grating (anti- or ferromagnetic alignment of adjacent wire magnetizations) can, therefore, be realized by sweeping the external magnetic field from a fully polarized state with parallel magnetizations towards the magnetic switching field [67]. The (anti-)ferromagnetic alignment of the two sub-lattices is furthermore revealed in ferromagnetic resonance (FMR) experiments of the respective structure, due to a discontinuous mode spectrum [67]. These substantial differences in the behavior of a homogeneous grating merit a separate investigation of AWNAs in this chapter. Specifically, the following analysis conducted in Sec. 5.1 is in analogy to the discussion of the homogeneous nanogratings (c.f. Sec. 4.1), particularly focusing on the impact of the edge-to-edge wire spacing on the collective ferromagnetic resonance behavior. Additionally, special focus is again put on the Kittel mode of the structure as a possible mediator

for chiral pumping. We then close this chapter by summarizing our findings in Sec. 5.2.

5.1 Ferromagnetic resonance

In Fig. 5.1, the adjusted simulation unit cell for an alternating width nanowire array (AWNA) is depicted schematically. Two infinitely long wires of different widths w_1 and w_2 are periodically aligned along the x-direction in an alternating array, where the respective sub-array containing the wires of width w_1 and w_2 can be interpreted as a sub-lattice of the structure. Both sub-lattices are otherwise identical with regards to wire height h, length and material composition. The grating is formed with a homogeneous edge-to-edge spacing s_{e2e} between adjacent wires. To align the wire magnetizations, a homogeneous static external magnetic field H_{ext} is applied along the wire direction (y-axis). A weak external driving field $\mu_0 h_{\mathrm{rf}}(t) = 1\,\mathrm{mT} \cdot \mathrm{sinc}(2\pi f_{\mathrm{c}}(t - t_0))$ is used with a cut-off frequency $f_{\mathrm{c}} = 100\,\mathrm{GHz}$ and a pulse delay $t_0 = 50\,\mathrm{ps}$, applied perpendicular to the grating along the x-axis to excite ferromagnetic resonance in the magnetic wires.

In order to investigate the impact of the edge-to-edge spacing s_{e2e} and thus the strength of the dipolar coupling on the AWNAs, a ferromagnetic resonance (FMR) simulation is performed for systems with varying values of s_{e2e} but otherwise constant system parameters, akin to the homogeneous nanogratings presented in Sec. 4.1. In Fig. 5.2, the resulting data of AWNAs consisting of CoFe wires with widths $w_1 = 200\,\mathrm{nm}$, $w_2 = 800\,\mathrm{nm}$ and height $h = 20\,\mathrm{nm}$ is shown. We use the material parameters $\mu_0 M_{\mathrm{s}} = 2.258\,\mathrm{T}$, $A_{\mathrm{ex}} = 2.6 \times 10^{-11}\,\mathrm{J/m}$ and $\alpha = 3.76 \times 10^{-3}$ for CoFe [13, 66]. For all spacings s_{e2e}, which are indicated in the respective lower right-hand corners in the plots of Fig. 5.2, a multitude of modes is observed. The discontinuities of these modes allow to discern the external magnetic field range, in which anti-ferromagnetic order (AFO) is established in the AWNA, here approximately from $\mu_0 H_{\mathrm{ext}} = -130\,\mathrm{mT}$ to $\mu_0 H_{\mathrm{ext}} = -30\,\mathrm{mT}$. Furthermore, it is noteworthy that the magnetic field range of the AFO state is independent of s_{e2e}. Starting with a small spacing of $s_{\mathrm{e2e}} = 50\,\mathrm{nm}$ in Fig. 5.2 (a), the spectrum generally agrees with the expectation of a superposition of two spectra of non-alternating, homogeneous nanogratings (c.f. Fig. 4.2) in the positive magnetic field range. Two high intensity modes at low frequencies and a multitude of higher order Damon-Eshbach modes are visible, which both can be attributed to the two different kinds of wire sub-lattices being present. Upon comparing these results with those in Sec. 4.1, it is therefore reasonable to assume that the two lowest frequency modes of high intensity in Fig. 5.2 (a) are the Kittel modes of the respective sub-lattices of the

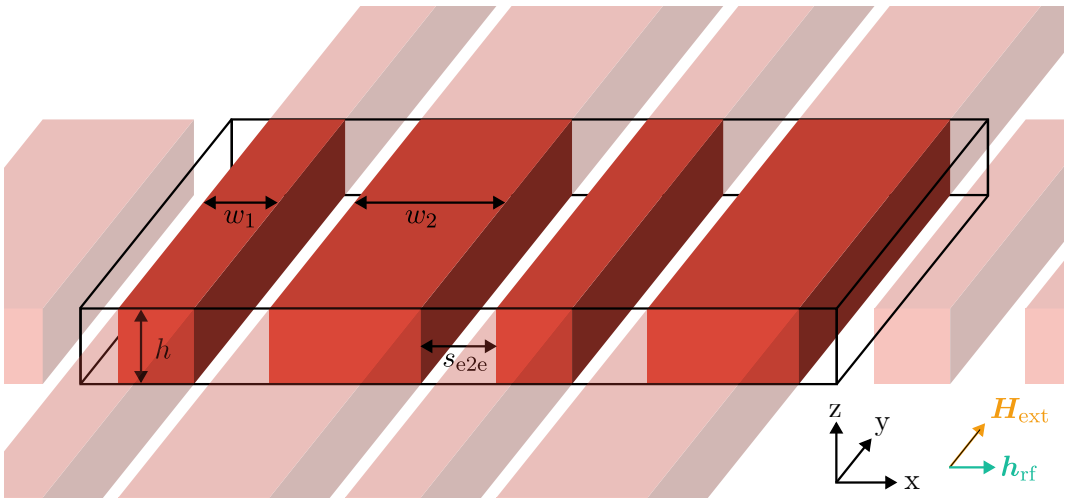

Figure 5.1: Schematic depiction of the model system for alternating width nanowire arrays (AWNAs). The simulation box (black lines) contains two "sub-lattices" of the AWNA, each being a regular array of nanowires with height h but different widths w_1 and w_2. These two different wire types of widths w_1 and w_2 are alternatingly aligned along the x-axis, with an edge-to-edge spacing s_{e2e} between neighboring wires. The width of the simulation box along the x-axis is chosen such that each wire width is represented twice, giving a total of four wires. By choosing a non-wire-centric layout of the simulation box, different wire types are present at the respective left and right border of the simulation box, allowing the use of periodic boundary conditions (indicated by pale red wires) to simulate realistic system proportions. To saturate the structure and control the (anti-)ferromagnetic order of the two sub-lattices, an external static magnetic field $\boldsymbol{H}_{ext}$ (orange) is applied along the wire axis in y-direction with again a 1°-offset to account for experimental uncertainties. After saturation, the array is excited using an oscillating driving magnetic field $\boldsymbol{h}_{rf}$ (turquoise), applied perpendicular to the wires along the x-direction.

AWNA. In the AFO-state, the mode spectrum clearly changes, as the lowest two modes now show a strong curvature over the rather small window of external field strengths. More precisely, it appears that an avoided- or anti-crossing is present between the two lowest modes in the spectrum. When increasing the wire spacing, starting from $s_{e2e} = 100\,\text{nm}$ in Fig. 5.2 (b) over $s_{e2e} = 200\,\text{nm}$ in (c) to $s_{e2e} = 300\,\text{nm}$ in (d), the spectrum appears mostly unaffected by the spacing in both ferromagnetic (FO) and anti-ferromagnetic (AFO) alignments. An exception are the two lowest modes of the AFO-state, as the first mode shifts upwards in frequency.Further increasing the spacing to $s_{e2e} = 900\,\text{nm}$ in Fig. 5.2 (e) shows a mode crossing between the two lowest modes of the AFO state, where the lowest mode at the left boundary of the AFO state ($\mu_0 H_{ext} \approx -130\,\text{mT}$) is now continuous with the mode in ferromagnetic ordered (FO) state in the positive magnetic field range. Contrarily, the first higher

mode at $\mu_0 H_{\text{ext}} \approx -130\,\text{mT}$ appears continuous with the ferromagnetic state present for negative external magnetic fields. Finally, increasing the spacing to $s_{\text{e2e}} = 1600\,\text{nm}$ (c.f. Fig. 5.2 (f)) shows no observable difference to the case of $s_{\text{e2e}} = 900\,\text{nm}$ (c.f. Fig. 5.2 (e)).
In Fig. 5.2, a general distinction can be made between a possibly coupled state of the AWNA, showing apparent anti-crossing between the two lowest modes for the spacings $s_{\text{e2e}} \leq 300\,\text{nm}$ (Fig. 5.2 (a)-(d)), and an uncoupled state, where the two lowest modes cross for large spacings $s_{\text{e2e}} \geq 900\,\text{nm}$ (Fig. 5.2 (e)-(f)). In the coupled state, we assume that the dipole-interaction between the two sub-lattices mediates coupled modes of both wire types if the system is in the AFO state. Since the dipole-interaction dominates in the long wavelength limit (c.f. Sec. 2.4), it is reasonable that this mode coupling mainly affects the Kittel modes of the respective sub-lattices. This is further supported by the dependence of the two lowest modes in Fig. 5.2 as a function of the wire spacing. For large spacings, the dipole-interaction is too weak to mediate any coupling between modes (see Fig. 5.2 (e)-(f)). Therefore, we interpret these spectra as a simple superposition of the FMR spectra of the respective (isolated) sub-lattices, with the different coercivity, i.e., shape anisotropy, causing different switching fields and frequencies of the modes.This interpretation is consistent with both the experimental finding by Goolaup *et al.* [74] that the dipole fields are dominated by the thicker wire, as well as consistent with the coupling range for nanogratings $s_{\text{e2e}} \leq 1.5$ determined in Sec. 4.2, as the mode crossing appears in Fig. 5.2 (e) at $s_{\text{e2e}} = 900\,\text{nm} = 1.125 w_2$.

In order to verify the interpretation of the FMR spectra for different values of s_{e2e} in Fig. 5.2, the spatial mode profiles can be used to determine the physical nature of each mode in the spectrum, which allows insight into the coupling of modes in the AFO-state for small spacings. In Fig. 5.3, the spatial mode profile is analyzed for three selected modes in the AFO-ordered state in the regime of strong dipole-coupling, at an edge-to-edge spacing of $s_{\text{e2e}} = 50\,\text{nm}$. Three markers in the FMR spectrum shown in Fig. 5.3 (a) symbolize the location of the selected modes at an external field value of $\mu_0 H_{\text{ext}} = -40\,\text{mT}$, located shortly after the transition from a fully saturated into an anti-ferromagnetically orderd (AFO) state. The lowest mode in Fig. 5.3 (a) exhibits the highest intensity at a frequency of $f_0 = (11.1054 \pm 0.0014)\,\text{GHz}$, indicated by the orange marker. Visualizing its mode profile in Fig. 5.3 (b) reveals that this mode is in fact a coupled Kittel mode of the two sub-lattices of the AWNA, as the spatial power distribution is quasi-uniform across both wire types. The intensity of this coupled Kittel mode is furthermore approximately equal for both wire species. The next higher mode, also strongly affected by the coupling, is located at $f_1 = (17.13 \pm 4.60)\,\text{GHz}$ and is indicated by a purple marker in the spectrum.

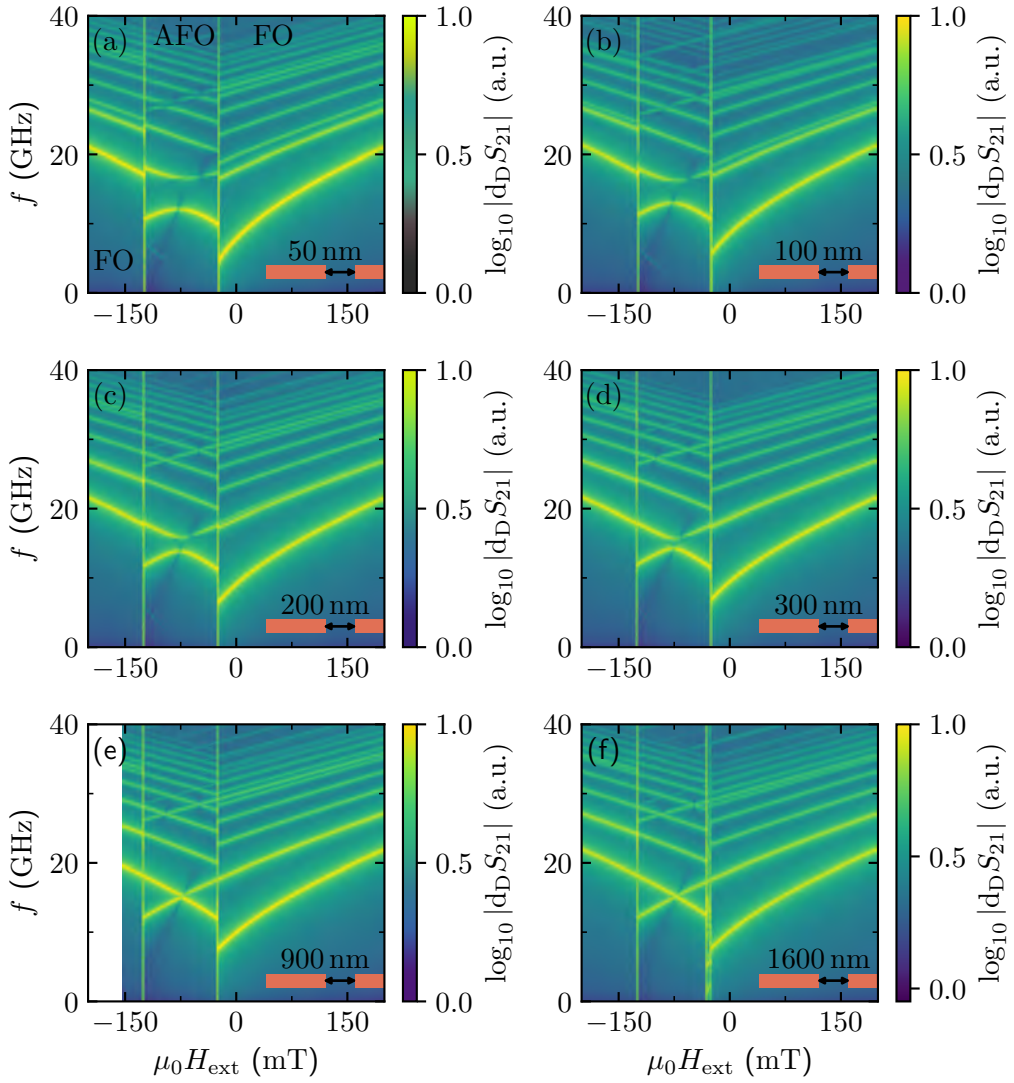

Figure 5.2: Results of the ferromagnetic resonance (FMR) simulation for a CoFe alternating width nanowire array (AWNA), consisting of two sets of wire widths $w_1 = 200\,\mathrm{nm}$ and $w_2 = 800\,\mathrm{nm}$ arranged with various edge-to-edge spacings s_{e2e} (indicated by the sketch in the respective lower right-hand corner). The mode discontinuities at $\mu_0 H_{\mathrm{ext}} \approx -130\,\mathrm{mT}$ and $\mu_0 H_{\mathrm{ext}} \approx -30\,\mathrm{mT}$ separate the anti-ferromagnetically ordered (AFO) from the ferromagnetically ordered (FO) state of the AWNA. **(a)** For $s_{\mathrm{e2e}} = 50\,\mathrm{nm}$, the two lowest modes in the spectrum presumably couple via the dipole-interaction and display an anti-crossing in the AFO region.**(b)-(d)** Increasing the spacing to values $s_{\mathrm{e2e}} \leq 300\,\mathrm{nm}$ reveals that the coupled modes of the anti-crossing approach each other in frequency space, due to a frequency upshift of the lower mode. **(e)-(f)** The result of large spacings $s_{\mathrm{e2e}} \geq 900\,\mathrm{nm}$ show a direct mode crossing due to decoupled modes in the AFO state, caused by a strongly reduced dipole-interaction. For such large values, the FMR spectrum is presumably simply the overlay of the FMR spectra of the two sub-lattices of the AWNA.

The mode profile in Fig. 5.3 (c) shows that this mode appears to be a coupling of the Kittel mode of the thinner wire sub-lattice with a low order Damon-Eshbach mode in the ticker wire sub-lattice, as deduced from the quasi-uniform power distribution in the thinner wire contrasted by the standing wave appearance in the thicker wire. Moreover, the latter shows a concentration of intensity towards the middle of the thicker wire, but it is dominated by the Kittel mode of the thinner wire. Lastly, the third mode influenced by the spacing is $f_2 = (21.23 \pm 0.17)\,\mathrm{GHz}$, shown as a dark blue marker in the FMR spectrum. Its mode profile visualized in Fig. 5.3 (d) reveals that it is again a coupling of the Kittel mode of the thin wire with a Damon-Eshbach mode of the thick wire, however, in contrast to (c) the Damon-Eshbach mode is now of a higher order and of higher intensity than the Kittel mode and thus dominates over the thin wire mode.
All in all, the spatial mode profiles presented in Fig. 5.3 confirm the assumption of a coupling of the Kittel modes of the two wire type sub-lattices, mediated by the strong dipole-interactions of the Kittel modes. Additionally, the close proximity in frequency between the Kittel mode of the thinner wire with the first two odd orders of Damon-Eshbach modes in the thicker wire leads to an additional hybridization of two coupled modes. For the lower order Damon-Eshbach mode of the thick wire the Kittel mode of the thin wire dominates, which is reversed for the higher order Damon-Eshbach mode. We assume that this multitude of couplings of the thin wire Kittel mode gives rise to the anti-crossing between the two lowest modes.

To contrast the findings in the strong dipole-interaction regime shown in Fig. 5.3, the spatial mode profiles are also analyzed for the case of negligible inter-wire coupling. The results for an edge-to-edge spacing of $s_{\mathrm{e2e}} = 1600\,\mathrm{nm}$ are shown in Fig. 5.4.Fig. 5.4 (a) displays the corresponding FMR spectrum alongside three markers indicating the extracted modes at an external magnetic field $\mu_0 H_{\mathrm{ext}} = -120\,\mathrm{mT}$, which is shortly before the array switches back into a fully polarized state. The lowest mode at $f_0' = (12.650 \pm 0.004)\,\mathrm{GHz}$ (orange marker) is shown in Fig. 5.4 (b) and has a quasi-uniform power distribution across the thinner wires with no visible power from the thick wires, which points towards a fully independent Kittel mode of the thin wire sub-lattice. The contrary case is present for the mode at $f_1' = (18.214 \pm 0.002)\,\mathrm{GHz}$ (purple marker), Fig. 5.4 (c), where the power is quasi-uniformly distributed only across the thick wires, indicating to be the independent Kittel mode of the thick wire sub-lattice. Finally, the third mode at $f_2' = (24.28 \pm 0.03)\,\mathrm{GHz}$, which is also affected by the dipole-interaction for smaller s_{e2e} values (c.f. Fig. 5.3), is depicted in Fig. 5.4 (d), showing only a low order Damon-Eshbach mode in the thick wire.
Subsequently, the mode profiles for the non-interacting wires presented in Fig. 5.4

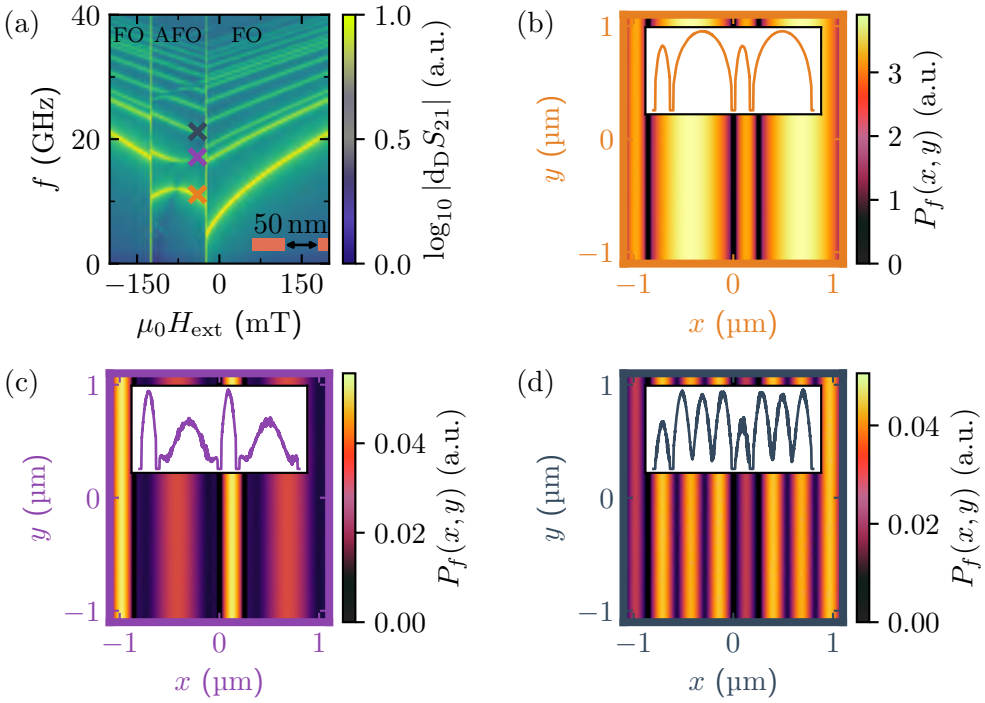

Figure 5.3: Selected spatial mode profiles for the FMR simulation of an alternating CoFe nanograting, consisting of wires with widths $w_1 = 200\,\mathrm{nm}$, $w_2 = 800\,\mathrm{nm}$ and height $h = 20\,\mathrm{nm}$, arranged with an edge-to-edge spacing $s_{\mathrm{e2e}} = 50\,\mathrm{nm}$. The mode profiles confirm the assumption of coupled Kittel modes of the two wire types, mediated by the dipole-interaction in the anti-ferromagnetically ordered (AFO) state. **(a)** FMR spectrum depicting the selected modes at $\mu_0 H_{\mathrm{ext}} = -40\,\mathrm{mT}$, shortly after the transition into the AFO-state. **(b)** The lowest frequency, highest intensity mode at $f_0 = (11.1054 \pm 0.0014)\,\mathrm{GHz}$ (orange) shows a quasi-uniform distribution in both wire types, and therefore represents a coupling of the Kittel modes of the individual wires. **(c)** The second lowest frequency mode at $f_1 = (17.13 \pm 4.60)\,\mathrm{GHz}$ (purple) also features a quasi-uniform distribution across the thinner wire, whereas a low order Damon-Eshbach mode is present in the thicker wire. Therefore, the Kittel mode of the thin wire additionally couples to a Damon-Eshbach mode of the thick wire due to the close proximity of the modes in frequency space. **(d)** The next higher mode lies at $f_2 = (21.23 \pm 0.17)\,\mathrm{GHz}$ (dark blue), and represents a coupling of the thin wire Kittel mode to a thick wire Damon-Eshbach mode similarly to (c), however, with a higher order of the thick wire Damon-Eshbach mode.

confirm the interpretation of the FMR spectrum for different spacings presented in Fig. 5.2, where the anti-crossing of modes in the AFO-state is attributed to a mode coupling between the respective Kittel modes of the sub-lattices and adjacent low-frequency modes. This coupling vanishes for larger spacings, as the dipole-interaction becomes too weak for spacings $w_1 < w_2 \leq s_{\mathrm{e2e}}$, which leads to a simple superposition of the FMR spectra of the respective sub-lattices.

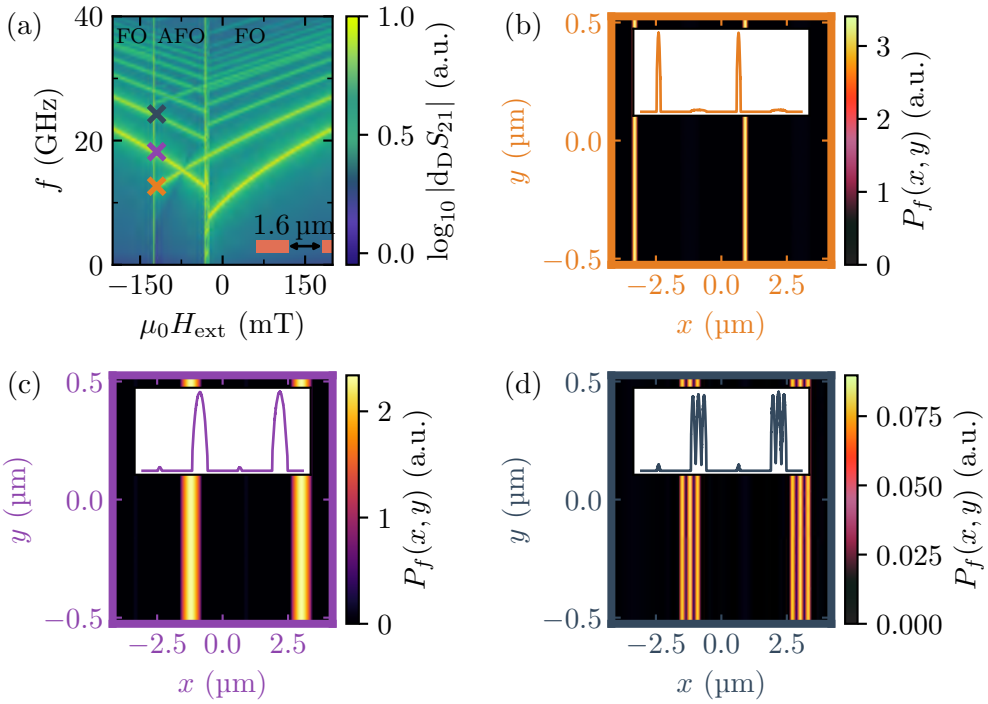

Figure 5.4: Selected spatial mode profiles for the FMR simulation of an alternating CoFe nanograting, consisting of wires with widths $w_1 = 200\,\mathrm{nm}$, $w_2 = 800\,\mathrm{nm}$ and height $h = 20\,\mathrm{nm}$, arranged with an edge-to-edge spacing $s_{\mathrm{e2e}} = 1600\,\mathrm{nm}$. The absence of coupled modes for larger spacings confirms that these FMR spectra may be seen as a simple superposition of the spectra of the respective sub-lattices. This is due to the negligibly small dipole-interaction at this length scale. **(a)** FMR spectrum depicting the selected modes at $\mu_0 H_{\mathrm{ext}} = -120\,\mathrm{mT}$, shortly before the transition back to the fully polarized array. **(b)** The lowest frequency mode at $f_0' = (12.650 \pm 0.004)\,\mathrm{GHz}$ (orange) shows a quasi-uniform distribution only in the thin wires, and is thus interpreted as the isolated Kittel mode of the thin wire sub-lattice. **(c)** The second lowest frequency mode at $f_1' = (18.214 \pm 0.002)\,\mathrm{GHz}$ (purple) features a quasi-uniform distribution across the thicker wire, therefore representing the isolated Kittel mode of the thick wire sub-lattice. **(d)** The third lowest frequency mode, located at $f_2' = (24.28 \pm 0.03)\,\mathrm{GHz}$ (dark blue), shows an isolated Damon-Eshbach mode of third order in the thicker wire sub-lattice.

5.2 Summary

The study of the ferromagnetic resonance response of alternating width nanowire arrays (AWNAs) (c.f. Fig. 5.1) can be summarized into two main takeaways. Firstly, we find that the different coercivities of the two wires species, induced by different shape anisotropies, result in a stable state of anti-ferromagnetic orientation (AFO) of adjacent wires. This AFO state is hereby only bound by the respective coercive magnetic fields of the two wire types, and thus both controllable via the external magnetic field and independent of the inter-wire spacing (c.f. Fig. 5.2). We further find that the edge-to-edge spacing s_{e2e} mainly affects modes in the AFO state. For small values of s_{e2e} the dipole-interaction between neighboring wires mediates a coupling of the Kittel mode of the thin wires with both the Kittel mode and low order Damon-Eshbach modes of the thick wires (c.f. Fig. 5.3). This hybridization of the thin wire Kittel mode subsequently results in an anti-crossing of the coupled modes in the AFO state. In contrast, for wire spacings $s_{\mathrm{e2e}} \geq w_2$, with w_2 the width of the thicker wire, the dipole-interaction is too weak to form a mode coupling, resulting in a mode crossing of the isolated Kittel modes of the respective wire types (c.f. Fig. 5.4).
In total, the findings for AWNAs allow for intriguing speculation towards their possible usage as mediators of chiral pumping (c.f. Sec. 2.5.2) to induce non-reciprocal spin waves. The relative orientation of the nanograting and thin film magnetizations is a crucial aspect in the realization of a chiral coupling between the gratings Kittel mode and the thin film spin waves. Since for dipole-coupled AWNAs the relative orientation of the two sub-lattices can be controlled via the external field, one possible proposition is an externally switchable device: for the fully polarized grating, both sub-lattices are expected to exhibit a chiral coupling to a certain momentum direction $+\boldsymbol{k}$, whereas in the AFO state the thicker nanowires (with now anti-parallel magnetization direction) are coupling chirally to spin waves travelling in the opposite direction $-\boldsymbol{k}$, therefore reducing the overall unidirectionality. For first simulation results of systems of AWNAs on top of YIG thin films, we refer to the Appendix A.2.

Chapter 6

Heterostructures of ferromagnetic nanogratings and thin films

As initially discussed in Sec. 2.5.2, the core mechanism of chiral pumping is based on the interaction between the Kittel mode of a ferromagnetic nanograting with spin waves traveling in the low-damping ferri- or ferromagnetic thin film underneath the grating. Specifically, Chen *et al.* [10] used a ferromagnetic Co nanograting placed on an insulating, ferrimagnetic thin film made of $Y_3Fe_5O_{12}$ (YIG) for their experimental realization. This section now aims to investigate how the interaction with the thin film changes the results obtained for isolated nanogratings in Ch. 4. To this end, we start with a discussion of the ferromagnetic resonance (FMR) response of a stacked system modeled according to the experimental device of Chen *et al.* [10] in Sec. 6.1, before comparing our findings to their reported experimental results. To then quantify whether this system realizes unidirectional spin waves induced via chiral pumping, we focus on its spin wave transport properties in Sec. 6.2. Finally, we end this chapter by summarizing our findings in Sec. 6.3.

6.1 Ferromagnetic resonance

Starting with simulating the ferromagnetic resonance (FMR) for bilayered systems of nanogratings and thin films, the simulation box must be adjusted. In Fig. 6.1, the updated "unit cell" of the simulation (solid, black lines) is depicted schematically. The base is given by an either ferri- or ferromagnetic thin film (blue) with low magnetic damping, parameterized by its thickness t_{TF}. It is positioned at the bottom of the simulation box with respect to the z-axis. Three ferromagnetic wires (red) of width w and height h are oriented along the y-direction and positioned directly on top of the thin film to provide optimal conditions for (magnetic) dipole-interactions between the wires and the thin film. The grating formed by the wires is characterized by the edge-to-edge spacing s_{e2e} between adjacent wires. In order to simulate realistic sample proportions, periodic boundary conditions are used in both the x- and the

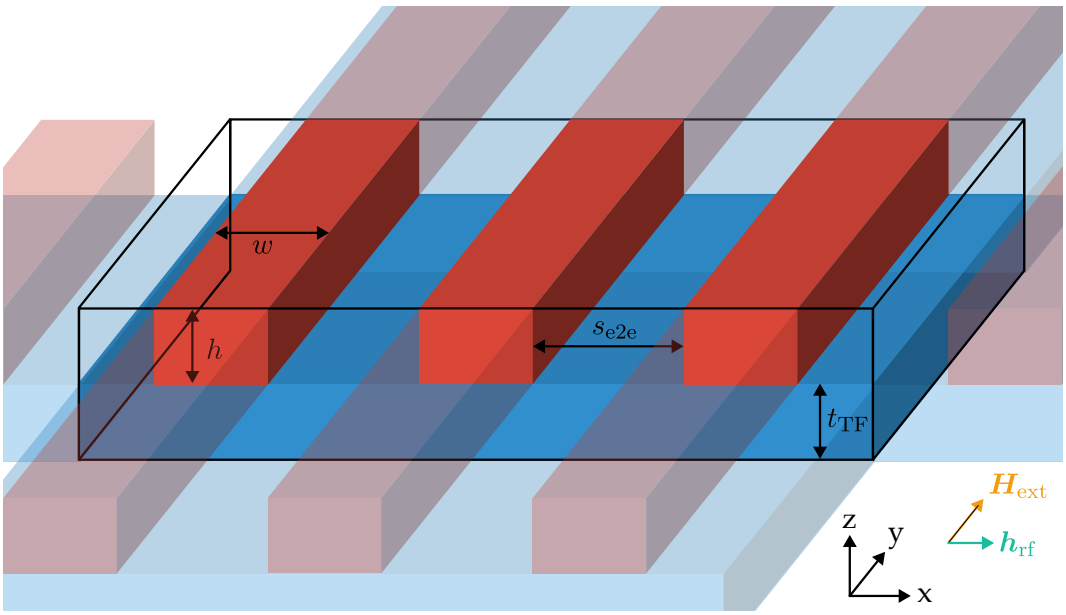

Figure 6.1: Simulation box designed for simulating bilayered systems consisting of a nanograting on top of a continuous thin film. Three (ferromagnetic) wires of width w and height h form the nanograting (red) at the top of the simulation box (positive z-direction), by aligning them along the y-axis with an edge-to-edge spacing s_{e2e}. The bottom of the simulation box is then filled by a (ferri-/ferromagnetic) thin film (blue), characterized by its thickness t_{TF}. In order to simulate sensible sample sizes for comparisons to experiments, periodic boundary conditions (pale color) are used in the in-plane x- and y-directions. To saturate the sample a static external magnetic field $\mu_0 H_{ext}$ (orange) is applied along the grating in y-direction. To provide excitation of the magnetic system, an oscillating driving magnetic field $\mu_0 h_{rf}$ (turquoise) is added perpendicular to the grating along the x-axis.

y-direction (pale colors). The sample is saturated by a static magnetic field $\boldsymbol{H}_{ext}$ (orange) applied along the y-direction, before the spin system is excited via an oscillating driving magnetic field $\boldsymbol{h}_{rf}$ (turquoise) applied perpendicular to the grating, along the x-axis. In this context, a spatially homogeneous excitation field $\mu_0 h_{rf}(t) = 1\,\mathrm{mT} \cdot \mathrm{sinc}(2\pi f_c(t - t_0))$ is used with a cut-off frequency $f_c = 100\,\mathrm{GHz}$ and a pulse delay $t_0 = 50\,\mathrm{ps}$. For each value of $\mu_0 H_{ext}$, the total propagation time is set to $T = 20\,\mathrm{ns}$, while sampling the (averaged) magnetization in $dt = 5\,\mathrm{ps}$ intervals.

The material system studied in the following is modeled according to the experimental device studied by Chen *et al.* [10]. A nanograting is constructed with infinitely long Co wires, measuring a width $w = 110\,\mathrm{nm}$ and height $h = 20\,\mathrm{nm}$. They are arranged periodically along the x-axis, with a center-to-center period

$a = 600\,\mathrm{nm}$ or equivalently an edge-to-edge spacing of $s_{\mathrm{e2e}} = 490\,\mathrm{nm}$. The material parameters for the Co grating are $M_{\mathrm{s}}^{\mathrm{Co}} = 1430\,\mathrm{kA/m}$, $A_{\mathrm{ex}}^{\mathrm{Co}} = 13 \times 10^{-12}\,\mathrm{J/m}$ and $\alpha^{\mathrm{Co}} = 0.01$ [10]. Due to its rather large wire spacing $s_{\mathrm{e2e}} \approx 4.45w$, the Co nanograting falls firmly in the previously determined (c.f. Sec. 4.2) non-interacting regime, as the dipole-interactions become negligibly small for large inter-wire distances. This grating is positioned on top of a $Y_3Fe_5O_{12}$ (YIG) thin film with thickness $t_{\mathrm{TF}} = 20\,\mathrm{nm}$, which is modeled using the material parameters $M_{\mathrm{s}}^{\mathrm{YIG}} = 140\,\mathrm{kA/m}$, $A_{\mathrm{ex}}^{\mathrm{YIG}} = 3 \times 10^{-12}\,\mathrm{J/m}$ and $\alpha^{\mathrm{YIG}} = 8 \times 10^{-5}$ [10].

In Fig. 6.2, the resulting FMR spectrum is shown for (a) a Co grating on top of a YIG layer and (b) an isolated Co grating without a thin film underneath. The direct comparison between Fig. 6.2 (a) and (b) provides insights on the impact of the YIG film on the FMR spectrum of the nanograting. In Fig. 6.2 (a), two different coercivities of the bilayered system are visible as mode discontinuities, which allows to differentiate the modes stemming from the Co grating from those stemming from the YIG layer. For one, a first switching field is observed at $\mu_0 H_{\mathrm{c}}^{\mathrm{YIG}} \approx -4\,\mathrm{mT}$, which is identified as the point of magnetization reversal, i.e., the coercive magnetic field, of the YIG thin film, as it it close to the zero field due to the vanishing in-plane shape anisotropy. Several modes in the spectrum are discontinuous at $\mu_0 H_{\mathrm{c}}^{\mathrm{YIG}}$, most notably the highest intensity mode, labeled mode 0, at low frequency. Subsequently, we assume that mode 0 is the Kittel mode of the YIG film. Furthermore, higher frequency modes of low intensity also appear to switch at $\mu_0 H_{\mathrm{c}}^{\mathrm{YIG}}$, and are are presumably Damon-Eshbach modes of the film. A second point of mode discontinuities can be seen at $\mu_0 H_{\mathrm{c}}^{\mathrm{Co}} \approx -145\,\mathrm{mT}$, the coercive magnetic field of the Co nanograting. Subsequently, the two visible coercivities $\mu_0 H_{\mathrm{c}}^{\mathrm{Co}} \approx -145\,\mathrm{mT}$ and $\mu_0 H_{\mathrm{c}}^{\mathrm{YIG}} \approx -4\,\mathrm{mT}$ restrict the magnetic field range, where the nanograting and the thin film magnetizations are anti-parallel (AP) aligned to each other. Fig. 6.2 (a) further reveals that only two additional modes have a comparable intensity to mode 0. These modes are labeled as mode 1 and mode 2, respectively, and are crossing $\mu_0 H_{\mathrm{c}}^{\mathrm{YIG}}$ before showing discontinuous behavior at $\mu_0 H_{\mathrm{c}}^{\mathrm{Co}}$. Specifically, mode 1 crosses the zero field at $f \approx 8\,\mathrm{GHz}$, and continues into the AP state as a mode with strongly reduced intensity. Conversely, mode 2 passes the zero field at $f \approx 19\,\mathrm{GHz}$, almost preserving its intensity upon entering the AP region. Going forward, we focus on the modes 0, 1 and 2, neglecting higher frequency modes with low intensity crossing $\mu_0 H_{\mathrm{c}}^{\mathrm{YIG}}$, as we expect these modes to exhibit only weak dipole-interaction.
The FMR spectrum of the isolated nanograting shown in Fig. 6.2 (b) reveals an increased coercivity of $\mu_0 H_{\mathrm{c}}^{\mathrm{NG}} \approx -170\,\mathrm{mT}$. The five visible modes in the spectrum are explained as the high intensity Kittel mode of the Co nanograting,

accompanied by 4 orders of odd wave number Damon-Eshbach modes in the grating (see discussion in Sec. 4.1 for details).
Comparing now the FMR spectrum of the Co nanograting placed on the YIG thin film in Fig. 6.2 (a) with that of the isolated Co nanograting in Fig. 6.2 (b), several interesting differences can be observed. For one, a non-negligible decrease in the coercivity of the Co nanograting, reducing from $\mu_0 H_c^{\mathrm{NG}} \approx -170\,\mathrm{mT}$ in the isolated case to $\mu_0 H_c^{\mathrm{Co}} \approx -145\,\mathrm{mT}$ when placed on the YIG thin film, is observed. Secondly, it appears that mode 2 in Fig. 6.2 (a) corresponds to the Kittel mode of the Co nanograting upon comparison to Fig. 6.2 (b). This raises questions about the physical interpretation of the weak mode 1 in Fig. 6.2 (a), as there should be no excitation of the grating with frequencies lower than its Kittel mode.

To discern the physical nature of the modes in the FMR spectrum shown Fig. 6.2, the spatial distribution of power for the respective modes can be used. The FMR spectrum for the system in Fig. 6.3 (a) displays three markers indicating the location of the respective modes calculated at an external magnetic field of $\mu_0 H_{\mathrm{ext}} = 50\,\mathrm{mT}$, where the color coding of the markers connects them to the respective spatial profiles. The lowest mode with highest intensity (mode 0) is found at $f_0 = (3.062 \pm 0.009)\,\mathrm{GHz}$ (orange) and is visualized in Fig. 6.3 (b). There, an almost cosine shaped distribution of power is visible in the front view (inset), which could either be attributed to a computational artifact or interactions with the nanograting, as discussed later on. As the minima of the cosine-like signal are located exactly at the positions of the nanowires, the signal shape could be explained by non-resonant nanowires reducing the local intensity when averaging the response over the entire stack of thin film and grating. Following this argument, mode 0 at f_0 can be regarded as spatially uniform across the entire thin film and identified as the Kittel mode of the YIG film, as initially expected from its symmetric shape and high intensity in the spectrum. The power spectrum of the first mode without discontinuity at $\mu_0 H_c^{\mathrm{YIG}}$ (mode 1) is located at $f_1 = (9.460 \pm 0.007)\,\mathrm{GHz}$ (purple), and is depicted in Fig. 6.3 (c). It shows a distinct concentration of power with a quasi-uniform mode profile across the wires, which would identify mode 1 as the Kittel mode of the Co nanograting. Additionally, mode 1 appears to be superpositioned with a lower intensity, high order Damon-Eshbach mode of the YIG thin film. Mode 1 appearing to be the Kittel mode of the grating is unexpected, as the comparison with the isolated nanograting in Fig. 6.2 suggests that mode 2 and not mode 1 is the Kittel mode of the grating. The more intense mode 2 is located at $f_2 = (20.46 \pm 0.03)\,\mathrm{GHz}$ (dark blue) and is visualized in the mode profile depicted in Fig. 6.3 (d). Here, in the front-view on the sample (inset) the mode distribution is complex, as it contains densely spaced higher order modes.

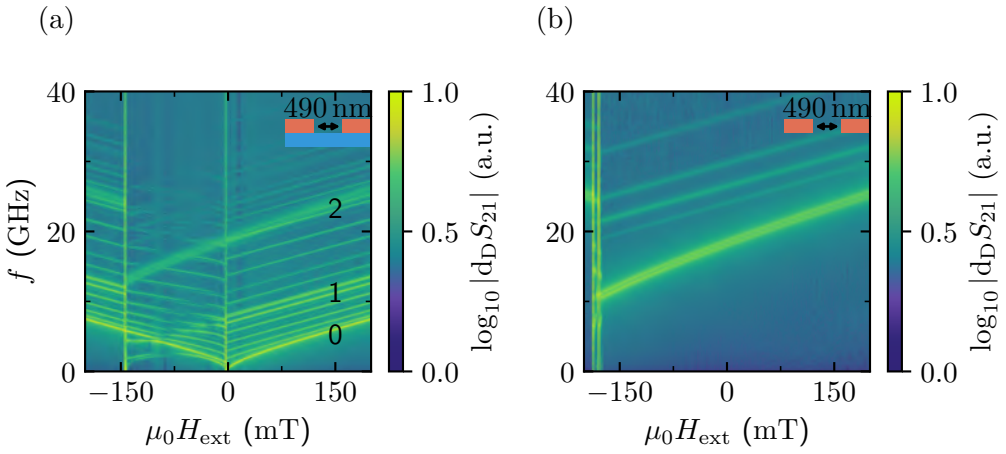

Figure 6.2: Influence of a YIG film of thickness $t_{\mathrm{TF}} = 20\,\mathrm{nm}$ on the ferromagnetic resonance (FMR) spectrum of a Co nanograting. The nanograting consists of wires of width $w = 110\,\mathrm{nm}$ and height $h = 20\,\mathrm{nm}$, arranged periodically with an edge-to-edge spacing of $s_{\mathrm{e2e}} = 490\,\mathrm{nm}$. **(a)** The grating on top of the thin film results in a rich mode spectrum, featuring two separate coercivities visible in the spectrum due to the different shape anisotropy of the grating wires and the thin film. In the magnetic field range between the coercivities $\mu_0 H_{\mathrm{c}}^{\mathrm{Co}} \approx -145\,\mathrm{mT}$ and $\mu_0 H_{\mathrm{c}}^{\mathrm{YIG}} \approx -4\,\mathrm{mT}$ the magnetizations of thin film and grating are anti-parallel (AP) aligned. The highest intensity mode (mode 0), is attributed to the Kittel mode of the YIG film, due to its symmetry with regards to $\mu_0 H_{\mathrm{c}}^{\mathrm{YIG}}$. At higher frequencies, the modes 1 and 2 with low and high intensity, respectively, do not show any discontinuity at $\mu_0 H_{\mathrm{c}}^{\mathrm{YIG}}$ and are therefore attributed to the Co nanograting. **(b)** For the isolated grating without the YIG thin film, an increased grating coercivity $\mu_0 H_{\mathrm{c}}^{\mathrm{NG}} \approx -170\,\mathrm{mT}$ is observed. The high intensity mode stems from the Kittel mode of the nanograting and is equivalent to mode 2 in (a). The higher modes in (b) are Damon-Eshbach modes of the nanograting.

However, from the top view in the spectrum it appears that mode 2 may be consisting of a Damon-Eshbach mode in both the thin film and the grating.
The unexpected discrepancies between the mode profiles in Fig. 6.3 and the frequency position of the modes in the spectrum may be explained by interactions between the Co nanograting and the YIG thin film. In the case of mode 0, shown in Fig. 6.3 (b), a cosine-like profile of the mode instead of a quasi-uniform one can be seen. A possible explanation beyond numerical artifacts could be magnetization pinning effects of the magnetically much harder Co nanowires acting on the YIG film. Specifically, we assume that the stray fields of the nanowires dampen the uniform precession below themselves, i.e., inducing a reduced amplitude of the Kittel mode of the YIG film directly below the nanowires. Subsequently, this would cause local dips in the mode intensity, just

as observed in Fig. 6.3 (b). A more involved question is why mode 1 appears to be the Kittel mode of the grating with a quasi-uniform intensity across the wires, as visible in Fig. 6.3 (c). Assuming again magnetization pinning caused by the magnetically hard Co wires, we deduce that the regions in the YIG film directly below the wires may be subject to strong interactions with the Co stray fields, creating magnetic domains in the continuous YIG film. To verify this claim, we inspect the spatial magnetization orientation of the thin film in Fig. 6.4. There, it can be seen that the stray field caused by Co wires influences the thin film so strong that their location is visible in the magnetic texture of the thin film, even when inspecting the sample from the opposite side. Subsequently, Fig. 6.4 verifies our assumption of magnetization pinning by the Co grating leading to the formation of magnetic domains in the YIG thin film. In this picture, the thin film can thus be treated as a one-dimensional magnonic crystal, composed of alternating regions located below the Co wires and below the vacant spaces of the grating. This leads us to the interpretation that mode 1 may be the Kittel mode of the YIG domains directly below the wires, rather than stemming from the wires themselves. This argument can further be extended to mode 2 in Fig. 6.3 (d). Here, we interpret the Damon-Eshbach mode profile visible also across the wires as modes belonging to the YIG regions below the wires, however, superimposed with the Kittel mode of the Co wires above it. The distinct difference in intensity between the wire locations and vacant spaces in Fig. 6.3 (d) is seen as support of this interpretation.

After understanding the nature of the modes labeled in the FMR spectrum shown in Fig. 6.2, a direct comparison can be made between the findings of the micromagnetic simulation and the experimental results reported by Chen *et al.* [10], which are depicted in Fig. 6.5. Fig. 6.5 (a) shows the simulated ferromagnetic resonance (FMR) spectrum for the system, following the experimental specifications and material parameters taken from Ref. [10]. The experimentally determined FMR spectrum of Chen *et al.* [10] is given for comparison in Fig. 6.5 (b). The first striking visual difference between the two spectra is the large difference in the number of visible modes. The simulated spectrum in Fig. 6.5 (a) exhibits a much richer spectrum with a multitude of higher order modes. In contrast, the experimental data in Fig. 6.5 (b) shows only two visible modes: a dominating upper mode and an almost vanishing lower mode. A detailed comparison between Fig. 6.5 (a) and (b) reveals that the high intensity mode in the experiment corresponds to mode 2 (Kittel mode of the nanograting) in the simulation, whereas the low intensity mode of the experimental data is represented by mode 0 (Kittel mode of the thin film) in the simulation. Strikingly, the intensity of mode 2 in the experiment is far larger than that of mode 0 (see Fig. 6.5 (b)). In the simulated data shown in Fig. 6.5 (a), mode 0 contrastingly shows an intensity at

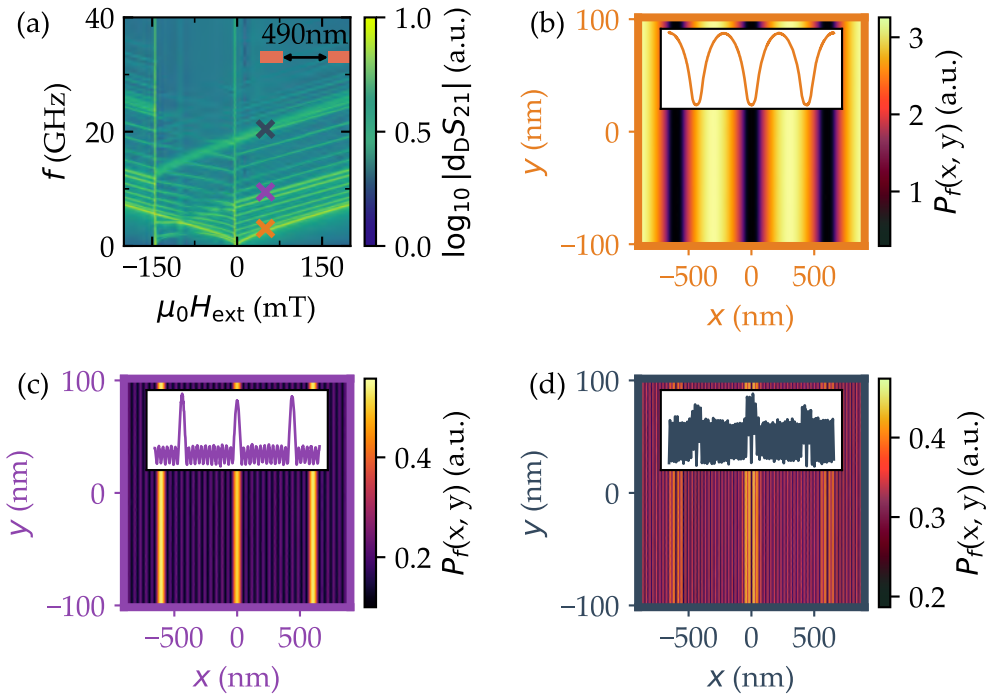

Figure 6.3: Spatial mode profiles for the ferromagnetic resonance (FMR) simulation of a Co nanograting consisting of wires of width $w = 110\,\text{nm}$ and height $h = 20\,\text{nm}$, arranged with an edge-to-edge spacing $s_{\text{e2e}} = 490\,\text{nm}$ on a YIG film of thickness $t_{\text{TF}} = 20\,\text{nm}$. **(a)** FMR spectrum showing color-coded markers of the three analyzed modes, at an external magnetic field $\mu_0 H_{\text{ext}} = 50\,\text{mT}$. At this magnetic field, the nanograting and thin film magnetizations are ferromagnetically aligned to each other. **(b)** The lowest mode of highest intensity (mode 0) is located at $f_0 = (3.062 \pm 0.009)\,\text{GHz}$ (orange), and shows a cosine-like power distribution in the front view of the sample (inset). Hereby, the magnetically hard Co nanowires could impede the magnetization precession of the YIG film directly below them, due to magnetostatic interactions. Therefore, mode 0 is identified as the Kittel mode of the thin film. **(c)** The first mode continuously passing $\mu_0 H_{\text{c}}^{\text{YIG}}$ into the region of the anti-parallel alignment of thin film and grating magnetization is located at $f_1 = (9.460 \pm 0.007)\,\text{GHz}$ (purple). The mode power is concentrated at the wire positions with quasi-uniform distribution. Therefore, it could be unexpectedly identified as the Kittel mode of the nanograting. However, we assume that this mode possibly stems from Kittel mode excitations of the magnetically pinned regions in the YIG film located directly below the wires, rather than from the grating itself. **(d)** A higher intensity mode can be observed for the mode at $f_2 = (20.46 \pm 0.03)\,\text{GHz}$ (dark blue). The mode profile here contains both a high order Damon-Eshbach modes of the thin film and a (fifth order) Damon-Eshbach mode at the wire locations. We interpret this mode to be a superposition of a Damon-Eshbach mode of the YIG regions below the wires and the Kittel mode of the nanograting, indicated by the increase in intensity across the wire regions.

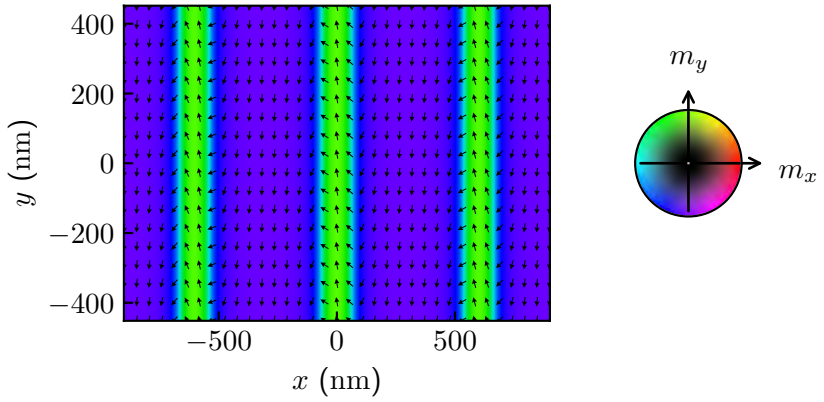

Figure 6.4: Magnetization of the YIG thin film, seen from a bottom-up view on the sample (c.f. Fig. 6.1). The location of the Co nanowires can be seen in the magnetic texture of the thin film. This supports our interpretation of magnetic domains forming in the thin film due to magnetization pinning, which is caused by the magnetically hard Co wires.

least one order of magnitude greater than mode 2. This is especially surprising as our simulations are conducted at a temperature $T = 0\,\mathrm{K}$, therefore we would expect an even weaker Kittel mode of the Co grating in the experimental data (c.f. Appendix A.1.2). Further of interest is the large difference of the coercive fields of the nanogratings between the two spectra: for the simulated data in Fig. 6.5 (a), the coercivity was found to be $\mu_0 H_\mathrm{c}^\mathrm{Co} \approx -145\,\mathrm{mT}$, whereas the experimental data in Fig. 6.5 (b) displays a coercivity of only $\mu_0 H_\mathrm{c}^\mathrm{Co,exp} \approx -80\,\mathrm{mT}$ for the Co nanograting.
In light of the spatial mode profiles discussed in Fig. 6.3, a further interesting result is that mode 1, which is comparable to mode 2 intensity-wise, is not present in the experimental data (c.f. Fig. 6.5 (a)-(b)). This is surprising, as Chen *et al.* [10] did not use a spacer layer between the Co grating and the YIG thin film in their experimental device, similar to the simulated model (c.f. Fig. 6.1). One possibility could be that, again, magnetization pinning effects show an impact on the observed behavior.
Summing up the takeaways from the comparison in Fig. 6.5 in terms of possible unidirectionality induced via chiral pumping, an obvious difference is that the simulated data displayed in Fig. 6.3 (a) predicts a vastly weaker intensity of mode 2 compared to the experimental data shown in Fig. 6.3 (b). This difference is especially striking when considering that the Kittel mode of the YIG film is barely visible in the experimental spectrum, whereas it has an intensity at least one order of magnitude larger than modes 1 and 2 in the simulated data. In the theoretical framework of chiral pumping, the intensity of the Kittel mode

of the nanograting is of central importance to the induced unidirectionality, as it corresponds to the intensity of its dynamic dipole fields mediating the coupling. Consequently, the much weaker Kittel mode of the Co grating in the simulation points towards far less unidirectionality induced via chiral pumping than reported by Chen *et al.* [10].

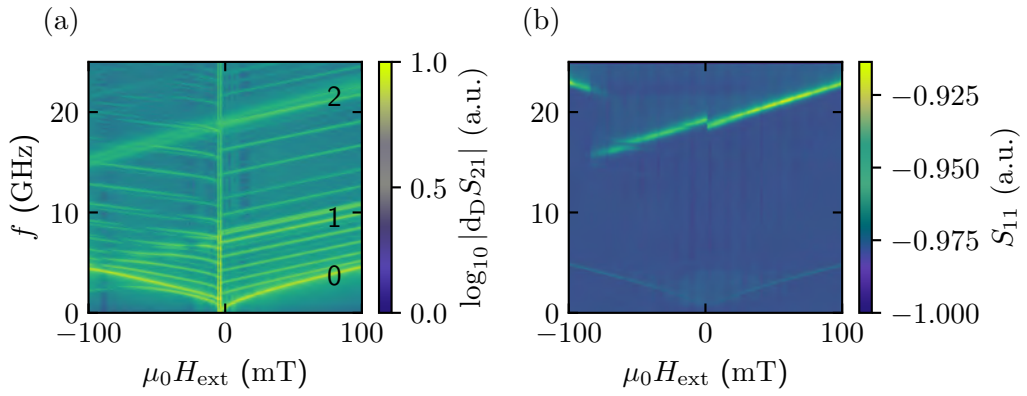

Figure 6.5: Comparison between the simulated data (a) and experimental findings of Chen *et al.* [10] (b) for a device consisting of a Co nanograting placed on a continuous $Y_3O_5Fe_{12}$ (YIG) thin film. The device specifications are $w = 110\,\mathrm{nm}$, $h = 20\,\mathrm{nm}$ and $s_{\mathrm{e2e}} = 490\,\mathrm{nm}$ with $t_{\mathrm{TF}} = 20\,\mathrm{nm}$ (c.f. Fig. 6.1). **(a)** The simulation spectrum displays a variety of modes. Three modes, labeled 0, 1 and 2, are physically interpreted in Fig. 6.3 and are of special interest. Mode 0 is found to be the Kittel mode of the YIG thin film, which also exhibits higher order modes. Mode 1 might stem from magnetic pinning effects in the YIG film caused by magnetoelastic coupling with the Co grating, inducing a magnetic domain structure in the YIG film. Finally, mode 2 is identified as the Kittel mode of the nanograting. Upon comparing their intensities, mode 0 dominates the spectrum, whereas mode 1 and 2 are approximately one order of magnitude less intense than mode 0. **(b)** The experimental data shows only two visible modes. The top mode, corresponding to mode 2 in the simulated spectrum (a), dominates the spectrum with high intensity. Far weaker, the analog to mode 0 in (a) is visible at the bottom of the spectrum.
The coercivities of the Co nanograting in the simulation (a) and experiment(b) differ strongly from each other: $\mu_0 H_c^{\mathrm{Co,sim}} \approx -145\,\mathrm{mT}$ versus $\mu_0 H_c^{\mathrm{Co,exp}} \approx -80\,\mathrm{mT}$. Furthermore, mode 1 from the simulation (a) is missing entirely in the experimental data (b). Finally, the difference in intensities of mode 2 between the two spectra leads to the assumption that the unidirectional spin wave transport properties of the device reported by Chen *et al.* [10] are not present in micromagnetic simulations. Figure (b) was taken from Ref. [10].

6.2 Spin wave dispersion

The discussion of the ferromagnetic resonance response of a bilayered system consisting of a Co nanograting placed on top of a YIG thin film in Sec. 6.1 concluded that only a weak dynamic dipole field is induced by the grating, due to the comparatively low intensity of its Kittel mode. Subsequently, the chiral pumping effect and the thus induced non-reciprocity of spin waves in the YIG film are also assumed to be weak or even negligible. In order to verify this assumption, the spin wave dispersion spectrum of the same device is analyzed. The device parameters are again $w = 110\,\mathrm{nm}$, $h = 20\,\mathrm{nm}$, $s_{\mathrm{e2e}} = 490\,\mathrm{nm}$ and $t_{\mathrm{TF}} = 20\,\mathrm{nm}$ (c.f. Fig. 6.1), in order to allow for comparison with the experimental findings reported by Chen *et al.* [10]. Fig. 6.6 shows the dispersion relation for the YIG thin film (blue) below the Co nanograting (red) in both the parallel (P) and anti-parallel (AP) alignment of the respective thin film and grating magnetizations (see sketches at the top of the figure). To realize the P state, the system is relaxed with an external magnetic field of $\mu_0 H_{\mathrm{ext}} = 50\,\mathrm{mT}$ applied along the y-axis (c.f. Fig. 6.1). Conversely, the AP state is realized by first establishing the P-state, before switching the external magnetic field to $\mu_0 H_{\mathrm{ext}} = -50\,\mathrm{mT}$ and relaxing again. To obtain the dispersion relation, the thin film may be interpreted in two separate ways.
One possibility is to use the previous methodology for one-dimensional magnonic crystals (c.f. Fig. 4.7) for the YIG thin film below the grating. Specifically, the thin film is interpreted as consisting of stripes of regions that are alternatingly located directly below a Co wire and below vacant spaces. For this purpose, a slight modification of the unit cell depicted in Fig. 6.1 is made, where now 99 Co wires are included. This allows to obtain a better resolution in momentum space. In Fig. 6.6 (a) and (b), the results of the magnonic crystal analysis of the thin film dispersion spectrum are shown. In the P state (Fig. 6.6 (a)), the dispersion displays a reduced zone-scheme, with clearly discernible modes visible above a frequency of $\approx 7\,\mathrm{GHz}$. Upon examining small momenta $|k_x| \to 0$, a slight chirality is observed. In detail, a shift of the mode intersections away from $k_x = 0$ and towards negative momenta can be seen, increasing in magnitude for lower frequencies. Upon transferring the system into the AP state (Fig. 6.6 (b)), the spectrum loses contrast, as the modes appear to broaden in frequency and lose intensity. Nonetheless, the slight shift to negative k_x of the dispersion spectrum is also present here. The observations in Fig. 6.6 (a) and (b) allow for important conclusions about whether the chiral pumping mechanism induces non-reciprocity for spin waves traveling in the YIG film. The asymmetry (i.e., the shift to negative momenta) present in the dispersion spectrum for both the P and AP states suggests that a finite chirality is induced in the dispersion spectrum, especially at lower frequencies. However, this chirality is expected to

be reversed upon entering the AP state if it is caused by chiral pumping, favoring then the opposite transport direction [8, 9]. Therefore, one would expect Fig. 6.6 (a) and (b) to be mirrored versions of each other in case in presence of chiral pumping, which is not the case. Consequently, the spin wave dispersion analysis of the YIG thin film as a magnonic crystal in Fig. 6.6 (a) and (b) points towards a finite chirality being present in the film, however, its indifference with regards to the P or AP state do not support the assumption that it is caused by the chiral pumping mechanism.
A different approach to obtaining the spin wave dispersion for the YIG thin film below the Co nanograting is by treating the film as a continuous medium, sampled by the real space discretization into computational cells. The resulting spectra are shown in Fig. 6.6 (c) and (d). In the P state (Fig. 6.6 (c)), the data shows multiple parabolic dispersions. Furthermore, in Fig. 6.6 (c) a multitude of periodic artifacts are visible, which are assumed to root from the real-space sampling inducing an artificial, non-physical Brillouin-zone in the spectrum. Nonetheless, the general shape of the dispersion in the P state shows a momentum-symmetric dispersion relation with no visible chirality. This is also observable in the AP state (Fig. 6.6 (d)), while showing again a decrease in contrast. Consequently, the analysis of the thin film dispersion as a continuous medium shows no impact on the spectrums chirality upon changing from the P to the AP state. This further supports the assumption that the Co grating fails to induce unidirectional spin waves via the chiral pumping mechanism.

In order to further check this interim result, the dispersion spectra shown in Fig. 6.6 may be used to compare the transmission of counter-propagating spin waves. This allows identifying any potential non-reciprocal spin wave transport properties of the YIG thin film, which could be attributed to interactions with the Co grating. Furthermore, a comparison can be made to the experimentally determined transmission rates of spin waves with opposite momenta reported by Chen *et al.* [10]. In Fig. 6.7, the transport properties of counter-propagating spin waves of momenta $|\boldsymbol{k}| = \pm k_x^{(\mathrm{m}=20)} = \pm 20\pi/a = \pm 0.1047\,\mathrm{rad/nm}$ are investigated. Note that for a momentum of this magnitude, only the dispersion spectra of continuous sampling of the YIG thin film (i.e., Fig. 6.6 (c) and (d)) are viable, as the magnonic crystal approach cannot resolve the dispersion in this wave number range. Again, both the parallel (P) and anti-parallel (AP) alignment state of the respective magnetizations of YIG thin film (blue) and Co nanograting (red) are considered, as indicated by the sketch at the top of Fig. 6.7. The first row (Fig. 6.7 (a)-(b)) presents the experimentally determined transmission rates of oppositely orientated spin waves, shown for the P and AP state, respectively [10]. For the P state (Fig. 6.7 (a)), a constant trans-

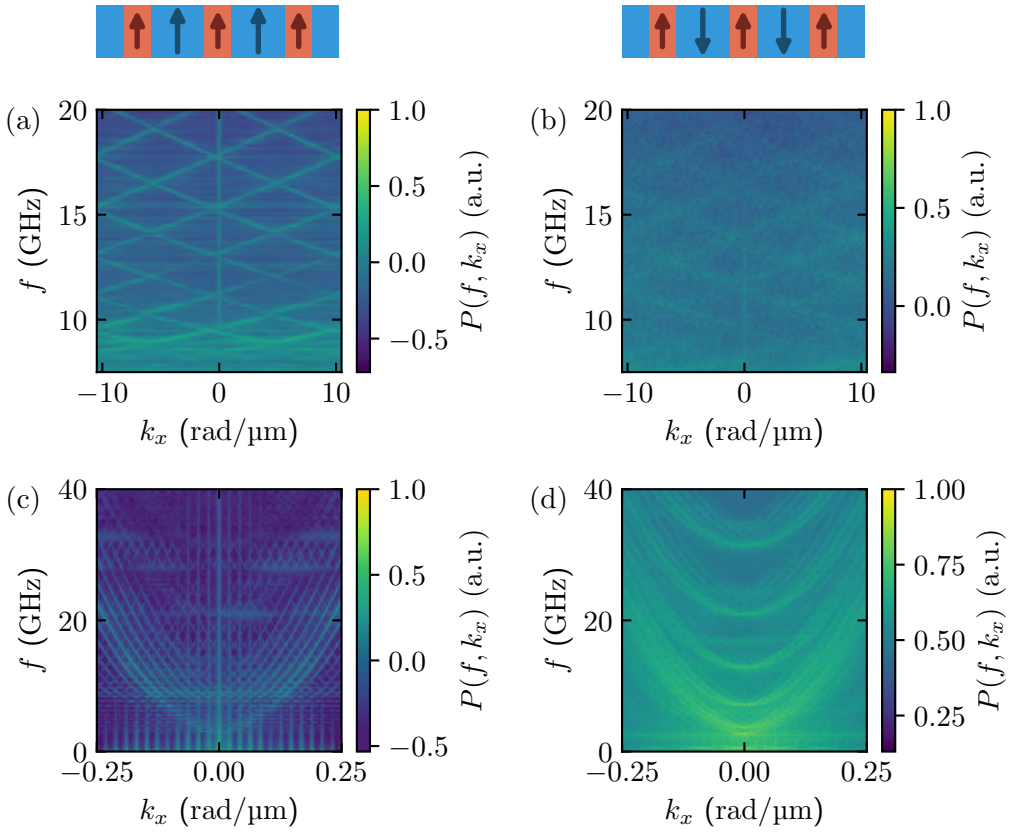

Figure 6.6: Spin wave dispersion spectra for the YIG thin film (blue) below the Co nanograting (red) (c.f. Fig. 6.1) in the parallel (P) and anti-parallel (AP) orientation of the respective magnetizations (sketches at the top of the figure). Two different approaches are used to calculate the dispersion in the YIG film: the top panels (a) and (b) treat the thin film as a magnonic crystal (MC), whereas the bottom panels (c) and (d) as a continuous medium (CM). **(a)** The MC dispersion in the P state shows a reduced zone scheme, with a shift of the visible modes towards negative momenta $-k_x$, obvious especially at mode intersections. The resulting asymmetry points towards an induced chirality in the dispersion of the thin film. **(b)** In the AP state, the MC dispersion loses sharpness, due to an apparent mode broadening. However, the visible modes appear to show the same features as in the P state (a). **(c)** The CM approach in the P state yields a parabolic dispersion. Additionally, the sampling in real-space causes periodic artifacts. Due to the perfect symmetry with regard to momentum, no chirality is observed. **(d)** The AP state in the CM approach also shows a parabolic dispersion with higher orders visible, showing no change in dispersion from the P state.
Overall, the observed indifference of the spin wave dispersion to the P or AP alignment of thin film and nanograting magnetizations is an argument against any unidirectionality induced in the thin film via chiral pumping.

mission rate is observed for $+\boldsymbol{k}$ (purple), whereas the opposite direction $-\boldsymbol{k}$ (turquoise) deviates considerably, showing a strongly increased transmission at around $f \approx 19\,\mathrm{GHz}$. When entering the AP state (Fig. 6.7 (b)), the situation is reversed, with now an almost constant transmission for $-\boldsymbol{k}$ (turquoise) and strong deviations for $+\boldsymbol{k}$ (purple), mostly at around $f \approx 18.5\,\mathrm{GHz}$. The data presented in Fig. 6.7 (a) and (b) is taken from the results of Chen *et al.* [10]. The change in spin wave transmission direction observed upon entering the AP state is in accordance with unidirectional spin wave transport realized via chiral pumping.
In contrast, the simulated transport properties resulting from the calculation of the dispersion in the YIG thin film are presented in Fig. 6.7 (c) and (d). There, in both the P (Fig. 6.7 (c)) and AP (Fig. 6.7 (d)) state, the signal shows no significant deviation between $-\boldsymbol{k}$ (green) and $+\boldsymbol{k}$ (orange). This points towards the thin film not having any preferred transport direction for spin waves of wave number $|\boldsymbol{k}| = \pm k_x^{(\mathrm{m}=20)}$ and subsequently no induced non-reciprocity at this wave number. This is in stark contrast to the experimental findings of Chen *et al.* [10]

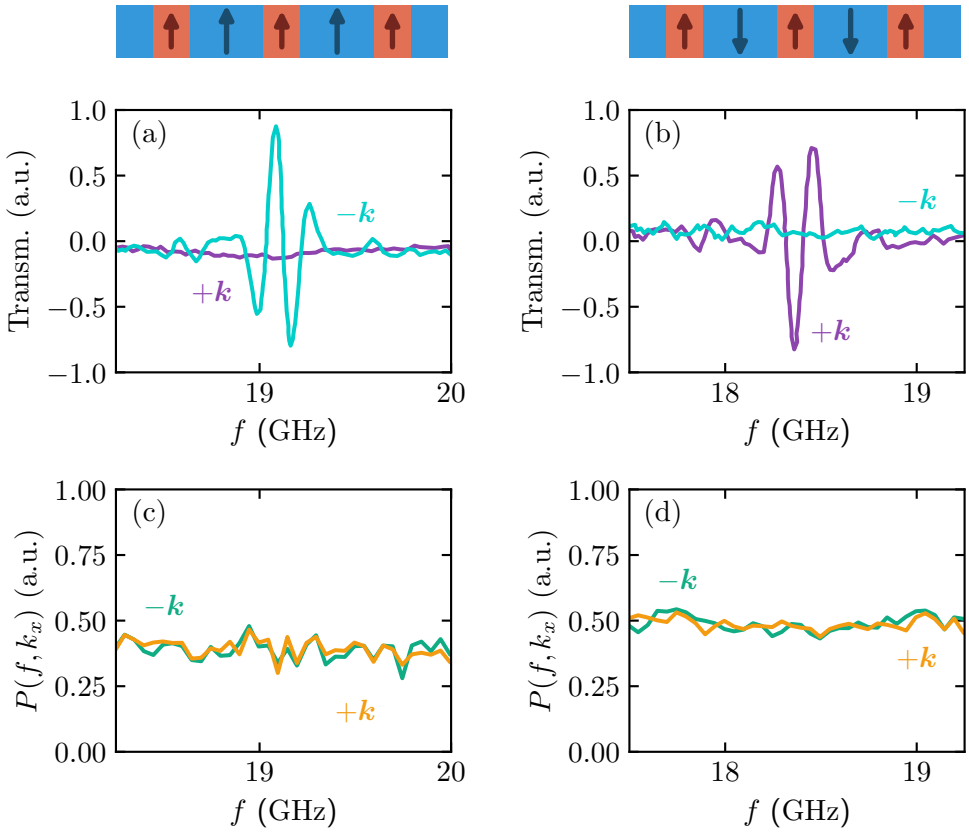

Figure 6.7: Comparison of the experimentally obtained transmission signal by Chen *et al.* [10] to the simulated system dispersion. Both the parallel (P) and anti-parallel (AP) alignment of the thin film (blue) and nanograting (red) magnetizations are considered (sketches at the top of the figure). This allows to check for inverted unidirectionality between the P and AP state, which is an indication of the chiral pumping mechanism. The comparison is made for fixed momenta $|\boldsymbol{k}| = \pm k_x^{(\mathrm{m}=20)} = \pm 20\pi/a = \pm 0.1047\,\mathrm{rad/nm}$, as was done in Ref. [10]. **(a)** The experimental transmission parameters show a preferred transmission of spin waves with $-\boldsymbol{k}$ (turquoise) over $+\boldsymbol{k}$ (purple) in the P state, with the largest deviation at $f \approx 19\,\mathrm{GHz}$. **(b)**In the AP state, this is inverted, with now $+\boldsymbol{k}$ being favored. The present non-reciprocity, coupled with the observed change in the favored transport direction, points towards chiral pumping as the origin of the unidirectionality. The data in both (a) and (b) is taken from Ref. [10]. **(c)-(d)** The line slices of the dispersion show no preferred transport direction in either the P (a) or AP (b) state, as the signal does not differ significantly between $+\boldsymbol{k}$ (orange) and $-\boldsymbol{k}$ (green). Consequently, this points towards no induced unidirectionality in the thin film and therefore also no chiral pumping to be present in the simulation.

6.3 Summary

Our investigation of stacks consisting of ferromagnetic nanogratings placed on low magnetic damping thin films (c.f. Fig. 6.1) yields important takeaways towards their usage as local transducers for chiral pumping.
Starting off, we first focus on the ferromagnetic resonance (FMR) of the stack in Sec. 6.1 to investigate the impact of the added thin film on the spectrum of the nanograting. Comparing the spectra of the stack and the isolated grating, we make two central observations (c.f. Fig. 6.2). For one, we find that the addition of the YIG film lowers the coercive magnetic field of the Co grating by about 15% from $\mu_0 H_c^{\mathrm{Co}} \approx -170\,\mathrm{mT}$ to $\mu_0 H_c^{\mathrm{Co}} \approx -145\,\mathrm{mT}$. Furthermore, we observe that the FMR spectrum of the combined system displays a richer mode spectrum than for the isolated grating. Specifically, the spectrum of the stack displays an additional mode (mode 1 in Fig. 6.2 (a)), which we interpret to stem from magnetization pinning effects caused by the Co grating, which in turn lead to the formation of magnetic domains in the YIG film (c.f. Figs. 6.3-6.4). Comparing our findings in the simulated spectrum to the experimental data reported by Chen *et al.* [10] reveals two key differences (c.f. Fig. 6.5). On one hand, we find the mode previously predicted to be caused by magnetization pinning effects (mode 1) is not present in the experimental data. On the other hand, the intensity of the nanogratings Kittel mode relative to the YIG film Kittel mode is inverted between the two spectra. While the simulated data suggests the Kittel mode of the grating to be about one order of magnitude less intense than the Kittel mode of the YIG film, the experimental data reveals that the Co Kittel mode dominates over all other features (c.f. Fig. 6.5). From the less intense Kittel mode of the nanograting in the simulation, we deduce that correspondingly also its dynamic dipole fields are less intense, leading us to expect only weak chiral coupling effects in the simulation.
To further investigate this assumption, we turn towards the analysis of the spin wave transport spectra of the YIG thin film in Sec. 6.2. There, we use two different approaches to determine the dispersion of the thin film layer, treating it for one as a magnonic crystal and conversely as a continuously sampled medium. In the magnonic crystal approach, the spin wave dispersion yields a small chirality (c.f. Fig. 6.6 (a)-(b)), which was however found to not be sensitive towards the relative orientation of thin film and nanograting magnetizations. On the other hand, obtaining the spin wave dispersion via a sampling of the continuous thin film (c.f. Fig. 6.6 (c)-(d)) showed no chirality present at all. Lastly, we analyze the line slices of the continuously sampled dispersion spectrum to compare them to the experimentally obtained transmission parameters of Chen *et al.* [10] (c.f. Fig. 6.7). We find the simulation data is nearly identical for both momentum directions (c.f. Fig. 6.7 (c)-(d)) with no changes induced by transferring into the

AP state. Subsequently, our data does not agree with the assumption of chiral pumping, as one would expect an inversion of the preferred transport direction upon changing the relative orientation of thin film and nanograting magnetizations.
All in all, we find that the investigation of both, the ferromagnetic resonance (FMR) response in Sec. 6.1 and the spin wave transport spectrum in Sec. 6.2, have not yielded any results in support of the realization of chiral pumping in this system.

Chapter 7

Summary and Outlook

At the end of this thesis, we summarize all results in Sec. 7.1, before discussing promising starting points for further research towards unidirectional magnonic devices in Sec. 7.2.

7.1 Summary

In this thesis, micromagnetic simulations are used to investigate the magnetic properties of ferromagnetic nanogratings with special emphasis on their possible application in devices enabling unidirectional spin wave propagation. Specifically, the theoretical framework of *chiral pumping* predicts an induced non-reciprocity of short wavelength spin waves in hetero-structures of ferromagnetic nanogratings and thin films, caused by the dipole-interactions between the layers [8, 9]. The non-reciprocity is further supported by recent experimental realizations by Chen *et al.* [10], demonstrating that chiral pumping provides a promising approach for nanometer-sized non-reciprocal devices. Nonetheless, in-house experiments conducted in similar material systems by C. Mang [11] were not able to confirm the unidirectionality close to 100% reported by Chen *et al.* [10]. To further investigate these experimental discrepancies, we use micromagnetic simulations to explore the impact of different grating design parameters on their applicability with regards to chiral pumping.

To this end, we started with simulating the ferromagnetic resonance (FMR) response of nanogratings constructed with different edge-to-edge spacings s_{e2e} between adjacent wires. There, we found that the systems Kittel mode shifts upwards in frequency and eventually crosses with the lowest order Damon-Eshbach mode for large separations $s_{\mathrm{e2e}} > w$, where w is the width of a single wire (c.f. Sec. 4.1). Moreover, extracting the demagnetization factors of the structure and comparing them to the analytical prediction for an isolated wire revealed that a sizable dipole-coupling between the wires induces a collective mode of the array for spacings below $s_{\mathrm{e2e}} \leq 1.5w$ (c.f. Sec. 4.2). These findings suggest that the wire spacing s_{e2e} must be chosen carefully, as low values obstruct the

assumption of an uncoupled array, whereas larger values lead to the Kittel mode not being the lowest energy excitation of the grating. Both of these scenarios are highly relevant for the realization of chiral pumping, as according to theory the Kittel mode of the nanograting and the coupling of its dynamical dipole fields is responsible for the unidirectionality of spin waves in adjacent magnetic thin films [8, 9]. Furthermore, we studied the dynamic properties of the gratings with focus on their spin wave dispersion, finding that for small wire separations s_{e2e} the system may be treated as a one-dimensional magnonic crystal (c.f. Sec. 4.3). Therein, we additionally demonstrated that increasing s_{e2e} opens up a band gap at the boundaries of the Brillouin-zone and leads to the flattening of the bands in the spectrum. The dynamical properties of the nanogratings thus show that for small spacings $s_{\mathrm{e2e}} < w$, one must further consider also a non-negligible transport of spin waves via the grating itself and not only the thin film.

Apart from homogeneous nanogratings, arrays of nanowires alternating in, e.g., material composition or geometric properties, have been the subject of several studies in literature [67, 74]. Distinctively, the different coercivities of the wire types induce a stable state of anti-ferromagnetic order (AFO) between the two wire type sub-lattices, which can be controlled via the external magnetic field [67]. By investigating the FMR response of alternating width nanowire arrays (AWNAs), we found that for small edge-to-edge spacings $s_{\mathrm{e2e}} < w_2$, where w_2 is the width of the thick wires, an anti-crossing of the two lowest modes appears in the AFO state (c.f. Sec. 5.1). This is due to the dipole-interactions between the two sub-lattices, as the anti-crossing is a consequence of the mode hybridization of the Kittel mode of the thin wire with both the Kittel mode and lowest order Damon-Eshbach mode of the thick wire. Conversely, for large inter-wire spacing $s_{\mathrm{e2e}} > w_2$, the dipole-coupling is not present and the isolated Kittel modes of the respective wire species cross in the AFO state. These distinctive features of the Kittel modes in AWNAs allow for intriguing speculation about their use as local transducers in the framework of chiral pumping. Concretely, we speculate that for uncoupled AWNAs the two-step magnetization reversal could allow for a device capable of not only one but two fixed values for the unidirectionality of spin waves.

Finally, we studied stacks consisting of ferromagnetic nanogratings deposited onto low magnetic damping thin films. Specifically, we modeled the system used by Chen *et al.* [10], consisting of a Co nanograting on a $Y_3Fe_5O_{12}$ (YIG) thin film. We simulated the ferromagnetic resonance of the stack and found that the simulation does not reproduce the results reported by Chen *et al.* [10], as the intensity of the Co gratings Kittel mode is far weaker than in the experimental data (c.f. Sec. 6.1). This leads us to the assumption that the weaker Kittel mode,

and therefore its weaker dynamic dipole fields, will not induce strong unidirectionality in the simulated system. Furthermore, we found an additional mode that is not featured in the experimental data by Chen *et al.* [10], which we interpreted to stem from magnetization pinning effects caused by the magnetically much harder Co grating acting on the YIG film (c.f. Sec. 6.1). Lastly, to quantify if any spin wave unidirectionality is induced in the thin film via chiral pumping, we analyzed of the spin wave dispersion of the stack (c.f. Sec. 6.2). There, we found that the simulated stack does not exhibit any non-reciprocal behavior at the wavelengths where Chen *et al.* [10] report close to 100% unidirectionality. Consequently, the simulations conducted in this work agree with previous experiments realized by C. Mang [11] and do therefore not support the presence of a chiral coupling between the nanogratings Kittel mode and the spin waves in the YIG thin film.

7.2 Outlook

The results of this thesis do not support chiral pumping as a promising candidate for the realization of unidirectional spin wave propagation in nanometer-sized magnonic devices. Nonetheless, several other physical mechanisms are currently investigated as possible sources of non-reciprocity in the magnonics community [7]. To close this thesis, we discuss two promising approaches that also take advantage of periodically structured magnetic materials, similar to the nanogratings discussed in this thesis.

For example, several approaches exist trying to leverage the Dzyaloshinskii–Moriya-interaction (DMI) to induce unidirectional spin waves. The DMI describes an asymmetric exchange interaction between two (neighboring) spins [75]. A particular type of DMI is the interfacial DMI (iDMI), which is relevant in multilayered structures of ferromagnets and heavy metals (e.g., Pt). [7]. With respect to unidirectionality, the iDMI is relevant as the asymmetric exchange induces an asymmetry in the spin wave dispersion, therefore inducing a non-reciprocity [7]. Micromagnetic simulations and theoretical considerations suggest that, consequently, the iDMI should be able to induce unidirectional spin waves in multi-layer magnetic materials containing heavy metals, with the experimental confirmation of these claims still ongoing [7]. Apart from stacks of continuous films, the iDMI also plays an important role in periodically structured material systems, similar to the nanogratings discussed in this thesis. For one, Gallardo *et al.* [76] have conducted simulations of systems consisting of Pt nanogratings placed on ferromagnetic thin films, finding a controllable band gap and flat bands induced by the periodic iDMI. A similar approach is taken by Flores-

Farías *et al.* [77], who extend this idea to two-dimensional magnonic crystals consisting of Pt square dots deposited on a ferromagnetic thin film. Using the combination of the asymmetric iDMI together with magnonic crystals therefore presents a promising starting point for further research towards unidirectional devices.

Another enticing approach towards realizing non-reciprocal spin waves is utilizing the unidirectionality of topologically protected edge-modes. Realizations of non-reciprocal spin waves via topological effects use the time-reversal symmetry protected edge-states of topological insulators [64]. These modes are located on opposite surfaces of the respective material and are robust towards material defects and back-scattering [64]. Recent studies by Mieszcak *et al.* [78] reported that numerical investigations of planar, one-dimensional magnonic crystals host interface modes located on the respective material boundaries. Another material system proposed by Feilhauer *et al.* [64] is a two-dimensional magnonic crystal built from dipole-coupled Permalloy triangles (c.f. Fig. 7.1 (a)). Up to now, experimental demonstration of 2D topological insulators in magnonic systems is hindered by the complex manufacturing [64]. Intriguingly, this approach reportedly offers a topological phase transition controllable via an external magnetic field, which would allow to invert the directions of the respective edge-modes [64]. We already conducted first simulations of a two-dimensional magnonic crystal built from the simulation cell in Fig. 7.1 (a), measuring 32 cells in x-direction and 8 cells in y-direction, as depicted in Fig. 7.1 (b). To visualize the edge-modes, we calculate the dispersion along the x-direction at the top and bottom edge and the middle of the magnonic crystal, as indicated by the arrows in Fig. 7.1 (b). At the top edge (c.f. Fig. 7.1 (c)) two separate bands can be seen, separated by a gap of $\approx 200\,\mathrm{MHz}$, with a unidirectional edge-mode connecting the two bands by crossing the gap with a negative slope. In contrast, in the sample middle (c.f. Fig. 7.1 (d)) the same two bands are visible, however, here the bands are separated with no mode crossing the gap. Moving now to the sample bottom edge (c.f. Fig. 7.1 (e)), a similar picture is visible. However, the unidirectional edge-mode crossing the gap now has a positive slope and has therefore changed direction. In total, we find two unidirectional, counter-propagating modes crossing the systems band gap at opposite edges of the two-dimensional magnonic crystal. This is in agreement with the results reported Feilhauer *et al.* [64] and therefore highlights the intriguing outlook of studying periodically modulated magnetic systems as hosts of (topological) unidirectional spin wave propagation.

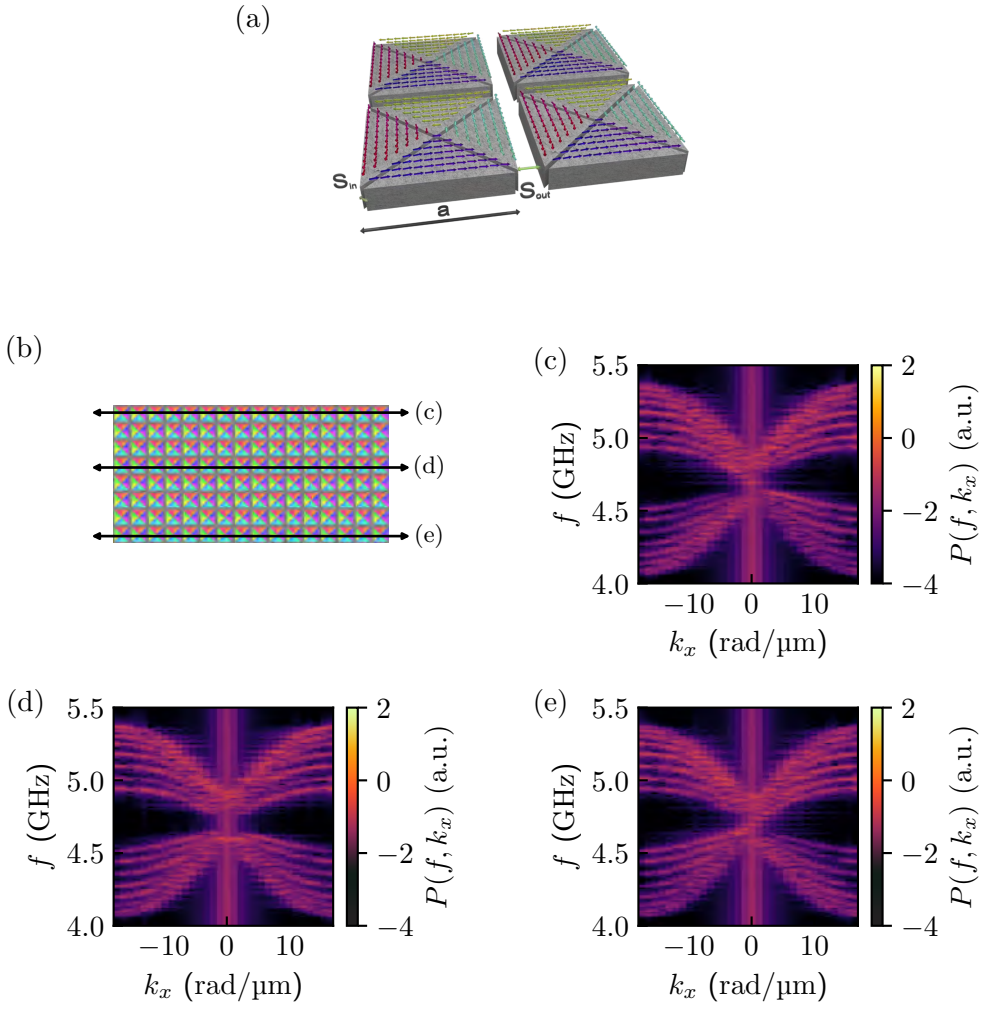

Figure 7.1: Unidirectional, topologically protected edge-modes in the system proposed by Feilhauer *et al.* [64]. **(a)** Visualization of the material system of NiFe triangles, pointing to a common center. Feilhauer *et al.* propose that this structure could be realized by etched X-shaped lines out of a fabricated square. The triangles are modeled to interact via dipole-coupling in the unit cell, but not between separate unit cells. This Figure is taken from Ref. [64]. **(b)** Top-down view on a two-dimensional magnonic crystal constructed from the simulation cells shown in (a). We simulate 32 unit cells in x-direction to enhance the resolution of the dispersion spectra. We study the edge-modes by comparing the dispersion at the top, middle, and bottom of the sample, as indicated by the arrows. **(c)** The dispersion spectrum at the top edge of the sample shows two bands separated by a gap $\approx$ 200 MHz. An edge-mode with a negative slope crosses the gap from the upper to the lower band. **(d)** In the sample middle, the dispersion spectrum shows the same two bands as in (c), however, no modes can be seen to cross the gap. **(e)** At the bottom edge, the gap is crossed by an edge-mode with a positive slope from the lower to the upper band. The counter-propagating edge-modes at the top/bottom edge of the magnonic crystal are hallmarks of a topological insulator. The presence of topological edge-modes in magnonic crystals gives a promising outlook to further engineer these material systems to be feasible for fabrication at larger scales.

Appendix A

Additional simulation data

A.1 FMR of ferromagnetic nanogratings

A.1.1 Influence of colormap scaling

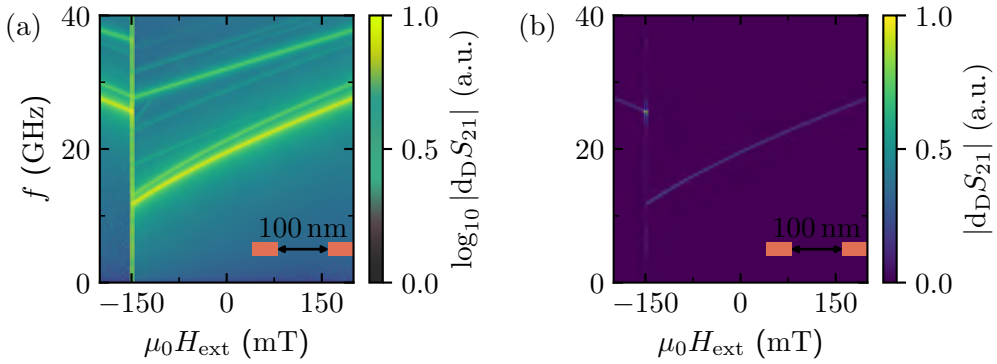

Figure A.1: Influence of the colormap scaling when presenting ferromagnetic resonance spectra (FMR) of micromagnetic simulations. Both figures depict the FMR response of a CoFe nanograting, consisting of infinitely long nanowires of width $w = 200\,\mathrm{nm}$ and height $h = 35\,\mathrm{nm}$ arranged with an edge-to-edge spacing of $s_{\mathrm{e2e}} = 100\,\mathrm{nm}$ (c.f. Fig 4.1). **(a)** Presenting the FMR spectrum using a base 10 logarithmic scaling for the colormap reveals a multitude of visible modes, including less intense higher orders. **(b)** Using a linear scale for the colormap results in the loss of essential features in the spectrum. In comparison to (a), only one mode is faintly visible. In scenarios where many modes are of equal intensity, oftentimes no modes are visible at all.

A.1.2 Finite temperature simulations

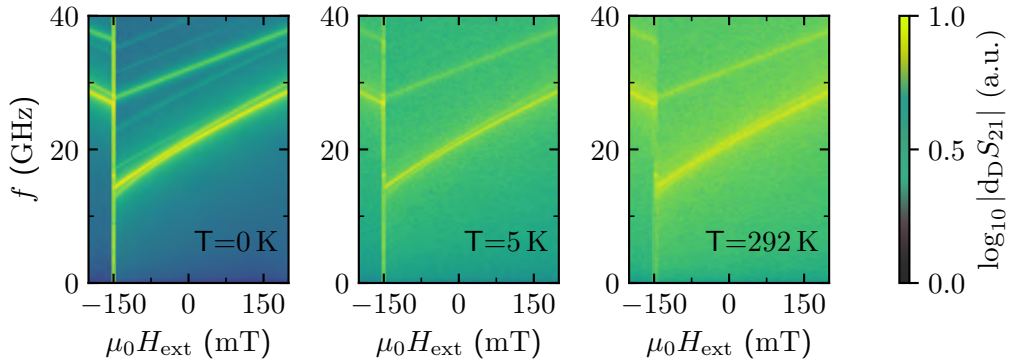

Figure A.2: Simulating structures at finite temperatures does not change the physical nature of the modes or their frequency dependence. Rather, only the relative intensity compared to the background, as well as the width of the mode, is influenced by finite temperature effects. Specifically, this figure shows the simulation of a CoFe nanograting, consisting of infinitely long nanowires of width $w = 200\,\mathrm{nm}$ and height $h = 35\,\mathrm{nm}$ arranged with an edge-to-edge spacing of $s_{\mathrm{e2e}} = 100\,\mathrm{nm}$ (c.f. Fig 4.1). This structure is simulated at three different temperatures: $T = 0\,\mathrm{K}$, which represents the conditions used for all other simulations throughout this thesis, $T = 5\,\mathrm{K}$, and $T = 292\,\mathrm{K}$. We find that increasing the temperature leads to a broadening of the modes and a higher background intensity, both of which is expected as the temperature is accounted for via randomly fluctuating magnetic fields [45].

A.1.3 Increasing inter-wire distance by decreasing wire width

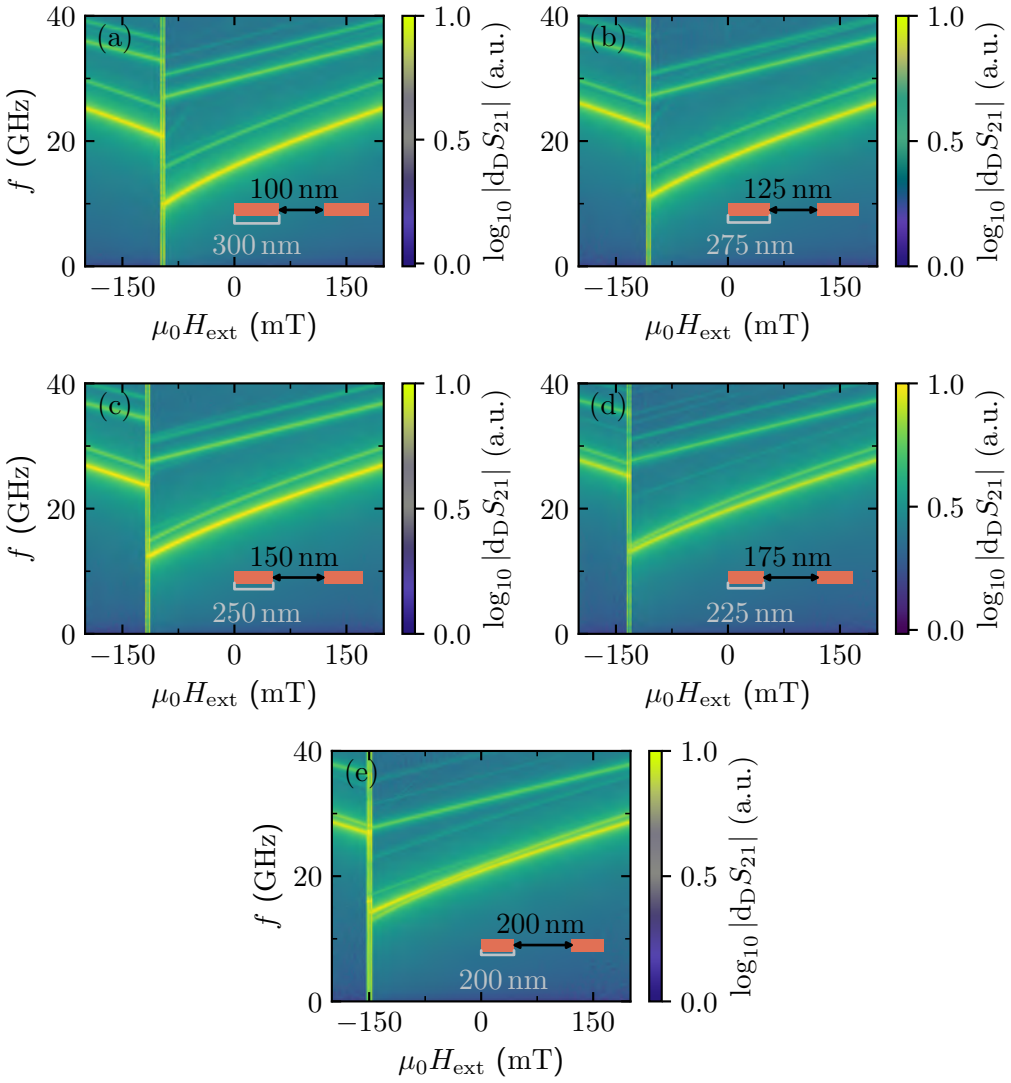

Figure A.3: Apart from simply moving the individual nanowires apart, one can also manipulate the edge-to-edge distance s_{e2e} by fixing the center-to-center distance a and varying the width w of the wires. **(a)-(e)** show the transition from $s_{e2e} = 100\,\text{nm}$ (a) to $s_{e2e} = 200\,\text{nm}$ (e) by decreasing the wire width w (gray sketch) from $w = 300\,\text{nm}$ (a) to $w = 200\,\text{nm}$ (e). Between (a)-(e), the changing coercivity of the individual wires due their change in geometry can be observed by the increasing coercive magnetic field from $\mu_0 H_c \approx -80\,\text{mT}$ (a) to $\mu_0 H_c \approx -150\,\text{mT}$ (e). This approach also results in a crossing of the high intensity Kittel mode with the lowest order Damon-Eshbach mode, as discussed in Sec. 4.1.

A.1.4 Full data for varying edge-to-edge spacing

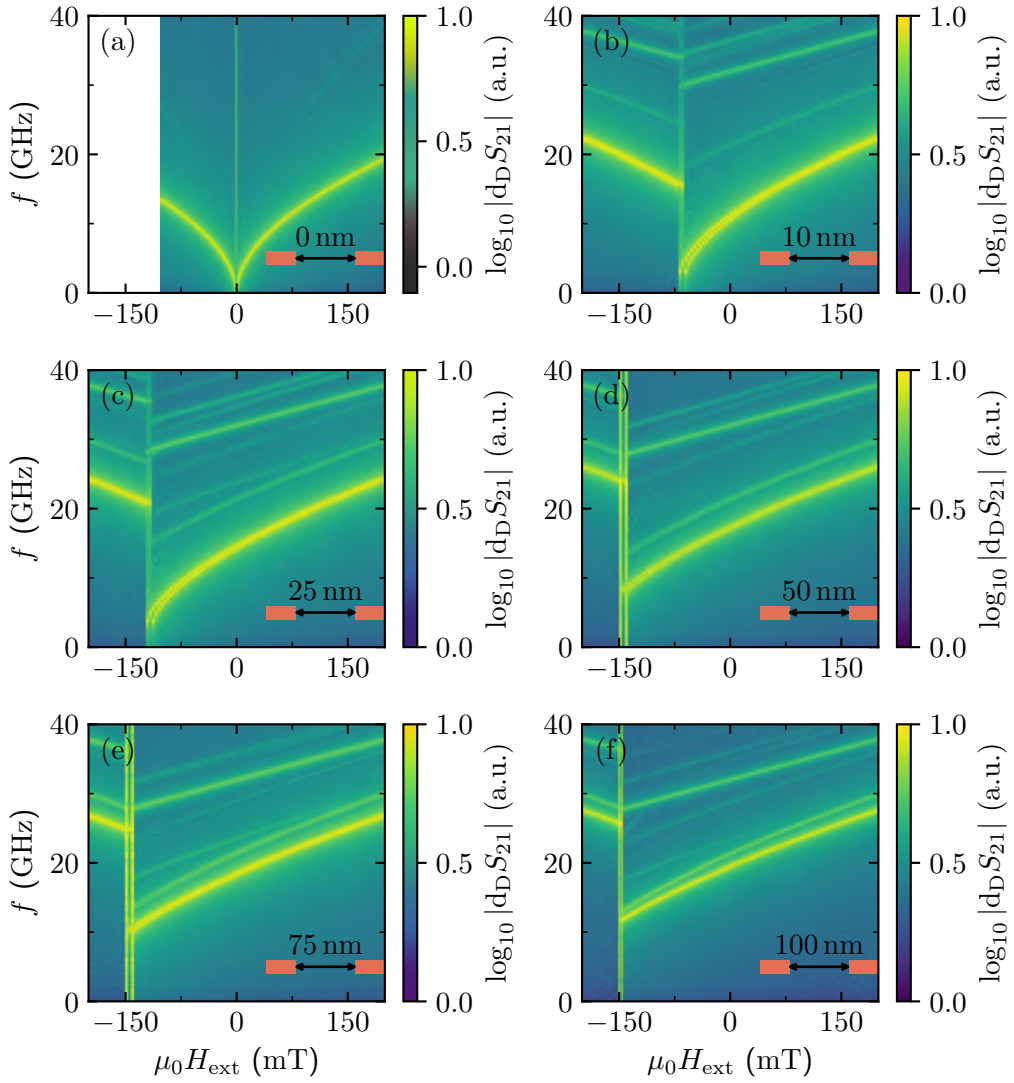

Figure A.4: Results of the ferromagnetic resonance (FMR) simulations for different nanogratings, each consisting of wires with width $w = 200\,\mathrm{nm}$ and height $w = 35\,\mathrm{nm}$, arranged with different edge-to-edge spacings s_{e2e} (c.f. Fig 4.1). This figure specifically shows the FMR spectra for spacing values $s_{\mathrm{e2e}} < w$, starting from a continuous thin film ($s_{\mathrm{e2e}} = 0\,\mathrm{nm}$). For the small spacings depicted in this figure, the strong dipole-interactions between adjacent wires strongly affect the collective response of the grating. This is visible, for example, by the continuous change of the coercive magnetic field for increasing s_{e2e}.

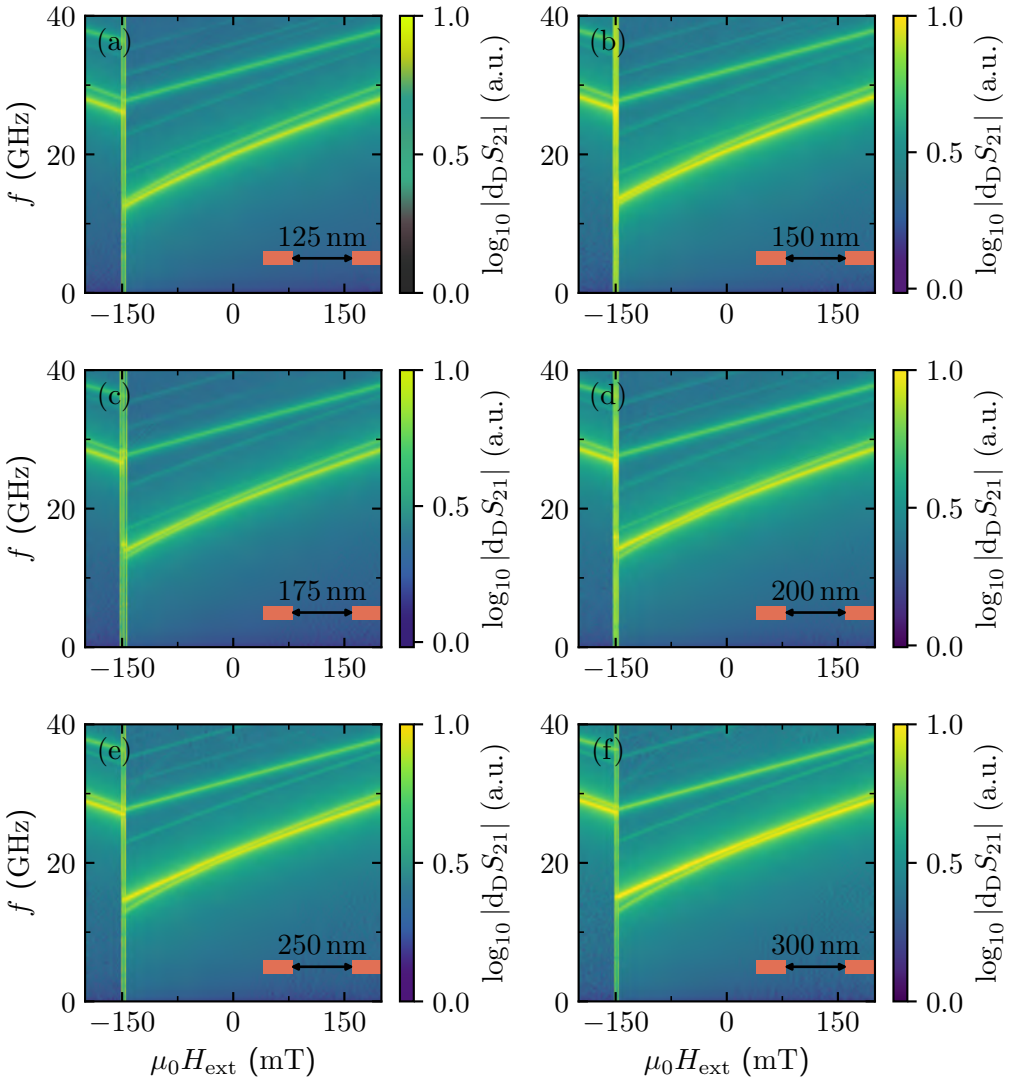

Figure A.5: Results of the ferromagnetic resonance (FMR) simulations for different nanogratings, each consisting of wires with width $w = 200\,\mathrm{nm}$ and height $w = 35\,\mathrm{nm}$, arranged with different edge-to-edge spacings s_{e2e} (c.f. Fig 4.1). This figure shows the FMR spectra for spacing values $s_{\mathrm{e2e}} \approx w$, where the inter-wire dipole-interactions start to lose relevance, as indicated by the almost constant coercive magnetic field in all spectra. Additionally, a mode crossing between the intense Kittel mode of the system and the lowest order Damon-Eshbach mode is observed in the negative field range before the wires switch magnetization, especially visible upon comparing $s_{\mathrm{e2e}} = 125\,\mathrm{nm}$ (a) and $s_{\mathrm{e2e}} = 300\,\mathrm{nm}$ (e).

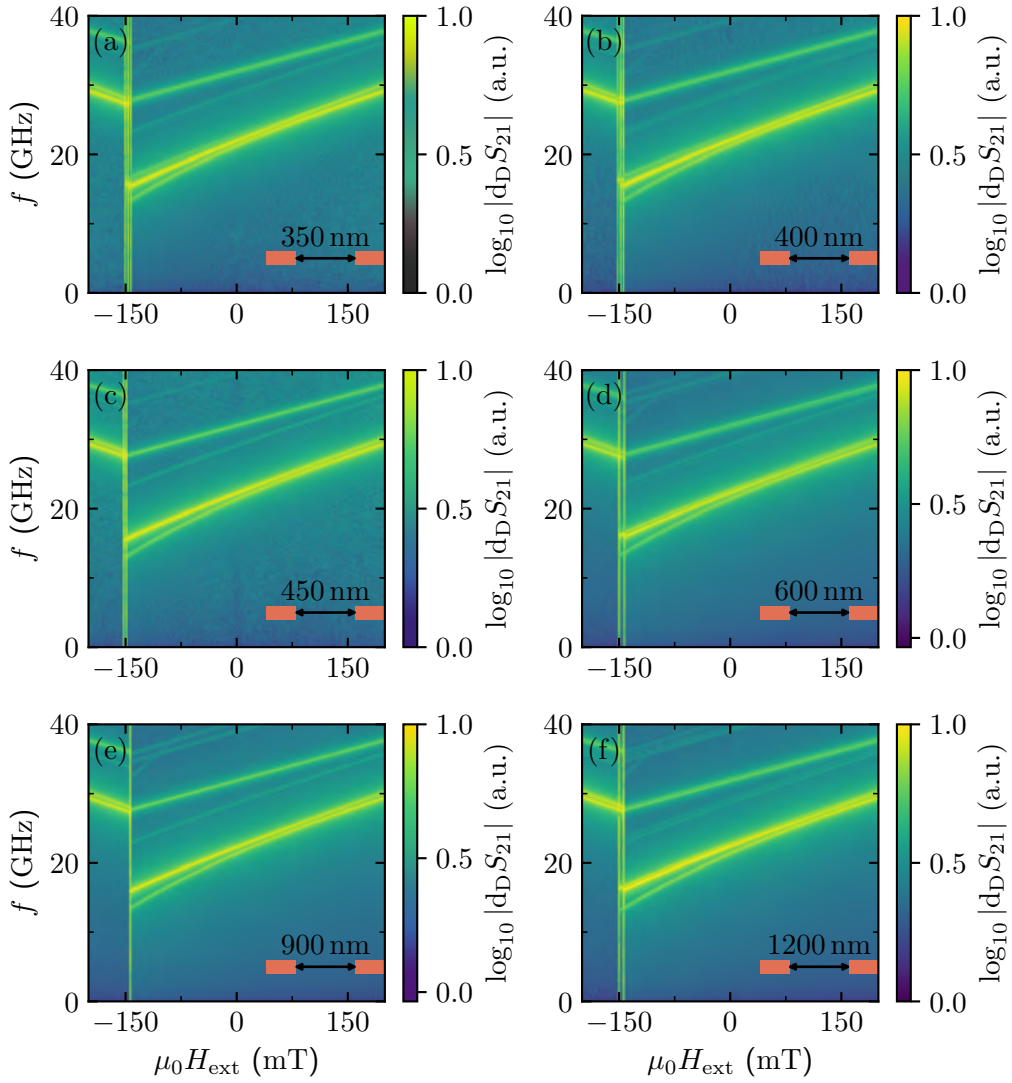

Figure A.6: Results of the ferromagnetic resonance (FMR) simulations for different nanogratings, each consisting of wires with width $w = 200\,\mathrm{nm}$ and height $w = 35\,\mathrm{nm}$, arranged with different edge-to-edge spacings s_{e2e} (c.f. Fig 4.1). This figure depicts the FMR spectra for spacing values $s_{\mathrm{e2e}} > w$. Here, dipole-interactions between neighboring wires are mostly irrelevant, as evident in the figure with no large visual differences between $s_{\mathrm{e2e}} = 350\,\mathrm{nm}$ (a) and $s_{\mathrm{e2e}} = 1200\,\mathrm{nm}$ (e).

A.1.5 FMR with external field perpendicular to the grating

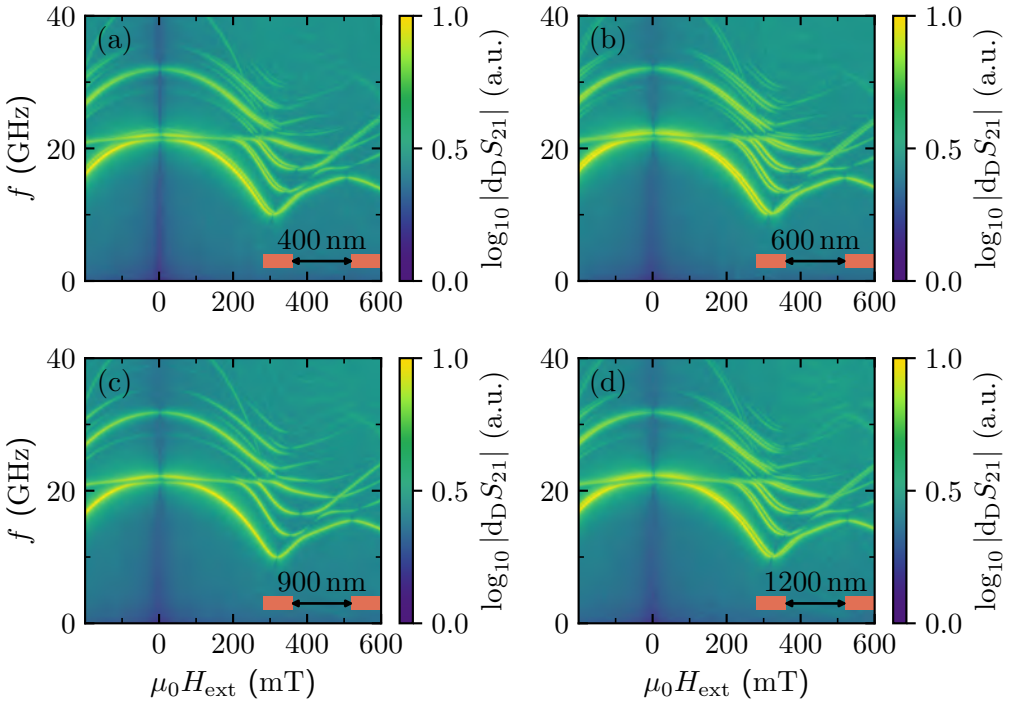

Figure A.7: Results of the ferromagnetic resonance (FMR) simulation for different nanogratings, each consisting of wires with width $w = 200\,\mathrm{nm}$ and height $w = 35\,\mathrm{nm}$, arranged with different edge-to-edge spacings s_{e2e}. Differently to previous simulations, the static magnetic field $\mu_0 H_{\mathrm{ext}}$ is oriented perpendicular to the nanograting, along the x-direction, using the coordinate system as in Fig 4.1). Induced by the shape-anisotropy of the wires, the minima of the systems Kittel mode is now shifted to around $\mu_0 H_{\mathrm{ext}} = 300\,\mathrm{mT}$.

A.2 FMR of heterostructures of alternating nanogratings and thin films

A.2.1 Resonance spectra

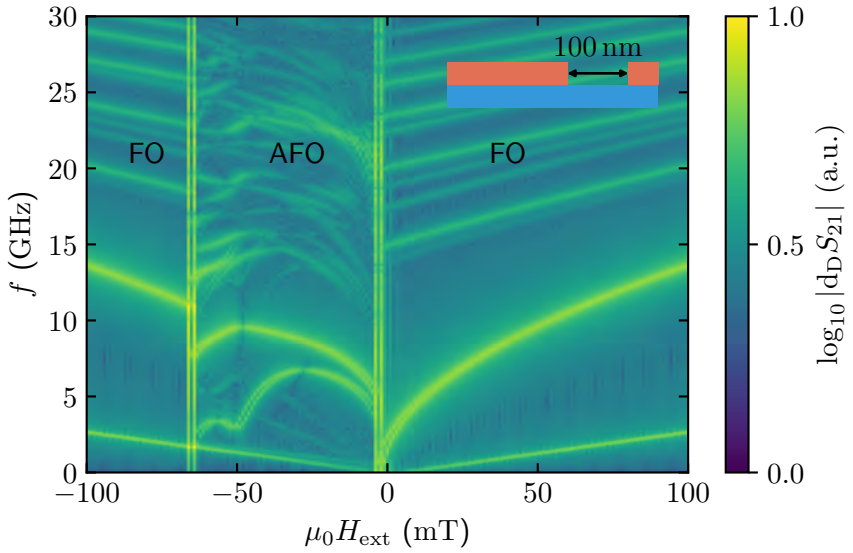

Figure A.8: Simulated ferromagnetic resonance (FMR) spectrum for a CoFe alternating width nanowire array (AWNA) on a YIG thin film in fine resolution around zero magnetic field. The AWNA is composed of wires of widths $w_1 = 200\,\mathrm{nm}$ and $w_2 = 800\,\mathrm{nm}$, arranged with edge-to-edge spacing $s_{\mathrm{e2e}} = 100\,\mathrm{nm}$ (c.f. Fig. 5.1). Both thin film and nanograting have a height $h = 20\,\mathrm{nm}$.
The spectrum clearly depicts regions of ferromagnetic (FO) and anti-ferromagnetic (AFO) order, restricted by the mode discontinuities appearing at the respective coercivity fields.

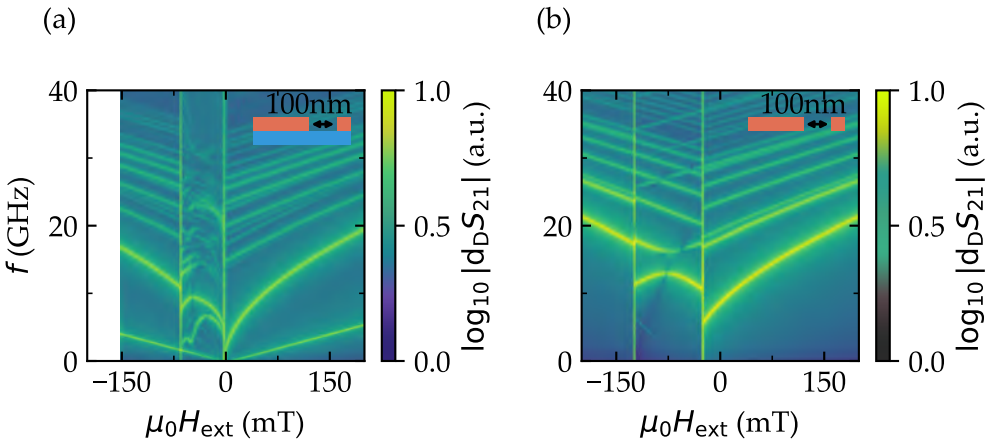

Figure A.9: Impact of a YIG thin film on the ferromagnetic resonance (FMR) spectrum of a CoFe alternating width nanowire array (AWNA), placed on top of the YIG film. The AWNA is composed of wires of widths $w_1 = 200\,\mathrm{nm}$ and $w_2 = 800\,\mathrm{nm}$, arranged with edge-to-edge spacing $s_{\mathrm{e2e}} = 100\,\mathrm{nm}$ (c.f. Fig. 5.1). Both thin film and nanograting have a height $h = 20\,\mathrm{nm}$. **(a)** The FMR spectrum of AWNA on top of the YIG film reveals a clear mode spectrum in the positive magnetic field range, similar to that of an isolated array. In the AFO state, from $\mu_0 H_{\mathrm{ext}} \approx -70\,\mathrm{mT}$ to $\mu_0 H_{\mathrm{ext}} \approx 0\,\mathrm{mT}$, the visible modes become hard to interprete, as the spectrum loses clarity for frequencies above $\approx 10\,\mathrm{GHz}$. **(b)** FMR spectrum for the isolated AWNA shows a distinct mode coupling in the AFO state (for details see Sec. 5.1).

A.2.2 Spatial mode profiles

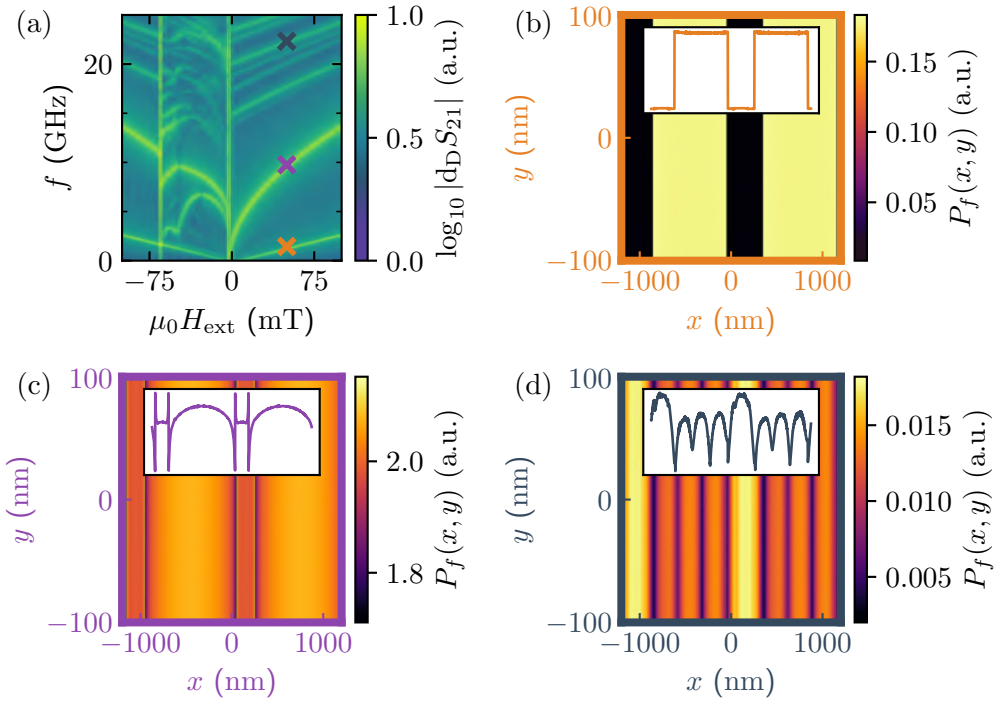

Figure A.10: Spatial mode profiles for a system of a CoFe alternating width nanowire array (AWNA) placed on a YIG thin film in a fully polarized state at $\mu_0 H_{\mathrm{ext}} = 50\,\mathrm{mT}$. The system is the same as in Fig. A.8. **(a)** FMR spectrum of the stack of the AWNA on the thin film with three color-coded markers indicating the frequency location of the modes. **(b)** The mode at $f_0 = (1.44 \pm 0.26)\,\mathrm{GHz}$ (orange) displays a uniform distribution of intensity across the thick nanowires, but no power at all the locations of the thin wires. We assume that magnetization pinning effects of the thin wires are at play, locally hindering the precession of the YIG thin film below them (similar to Fig. 6.3). Since the thicker Co wires have a strongly reduced shape anisotropy compared to the thinner wires, they do not induce magnetization pinning effects of this magnitude, and therefore also do not prevent precession in the YIG film. We therefore interpret this mode as the Kittel mode of the YIG thin film. **(c)** The mode at $f_1 = (9.759 \pm 0.002)\,\mathrm{GHz}$ (purple) shows a quasi-uniform mode profile across the thicker Co wires. Interestingly, in the thin wires an edge-mode appears to form, with sharp peaks of intensity located at the wire edges. No power is present in the vacant spaces, subsequently we classify this mode as a coupling of the Kittel mode of the thick wires with an edge-mode in the thin wires. **(d)** At $f_2 = (22.326 \pm 0.237)\,\mathrm{GHz}$ (dark blue), we find a quasi-uniform mode profile across the thin wires, with a low order Damon-Eshbach mode present in the thick wires.

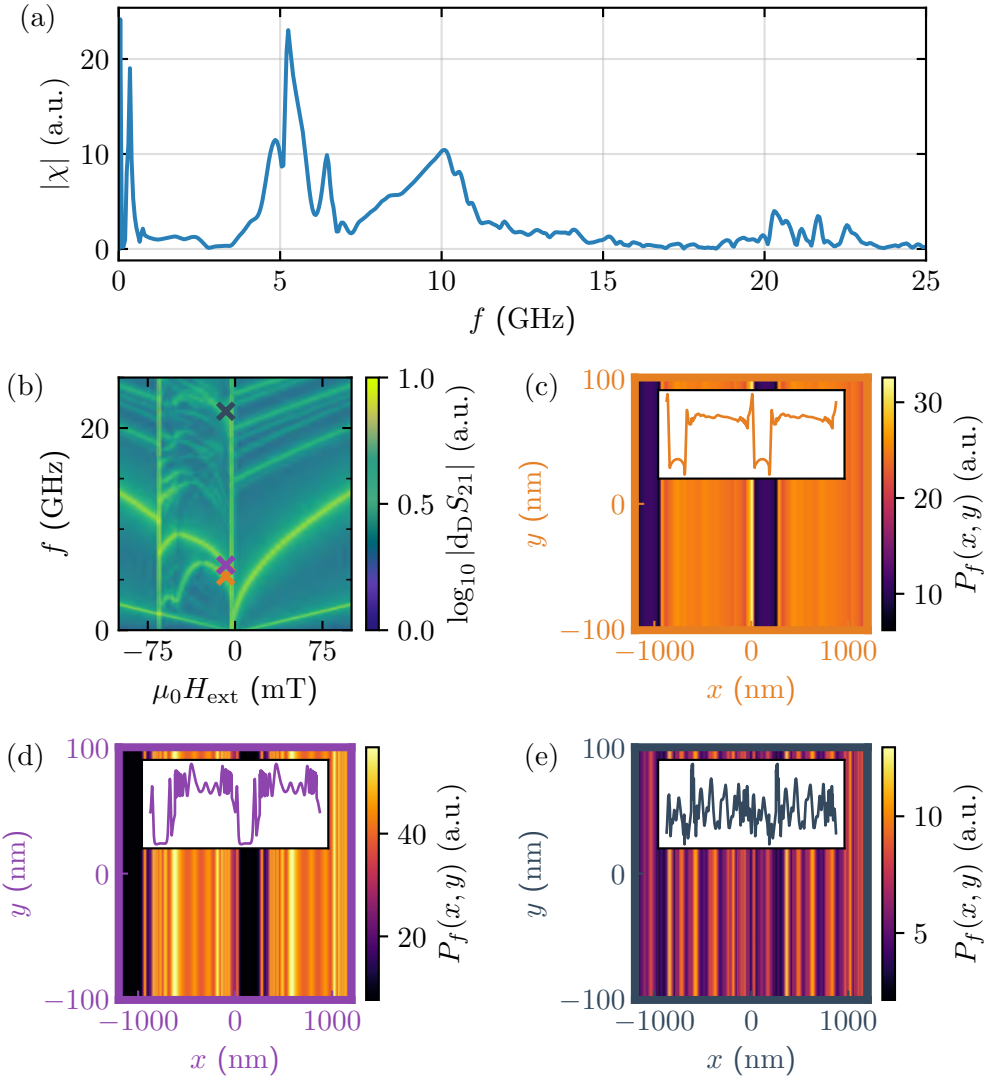

Figure A.11: Spatial mode profiles for a system of a CoFe alternating width nanowire array (AWNA) placed on a YIG thin film shortly after transitioning into an anti-ferromagnically ordered (AFO) state of adjacent wires at $\mu_0 H_{\text{ext}} = -8\,\text{mT}$. The system is the same as in Fig. A.8. **(a)** The line slice of the dynamical susceptibility $|\chi|$ at $\mu_0 H_{\text{ext}} = -8\,\text{mT}$ reveals that the system no longer responds with a characteristic Lorentzian line shape, indicating that in this state linear response theory (c.f. Sec. 2.3) does not apply. **(b)** FMR spectrum with color-coded markers indicating the location of the modes of interest at $\mu_0 H_{\text{ext}} = -8\,\text{mT}$. **(c)-(e)** The interpretation of the mode spectra is in large parts unclear, as the system is pertubed too far out of equilibrium to use the so-far applied methodology.

Appendix B

Code examples

This part of the appendix contains samples of code written for this thesis that we deem essential to recreate the presented work. While not exhaustive, they show the fundamental steps of how data for both ferromagnetic resonance (FMR) and spin wave dispersion spectra were obtained and evaluated.

B.1 Simulation

B.1.1 MuMax^3 sample code for FMR

```
OutputFormat = OVF2_TEXT
//###############################################//
//------------- SAMPLE DEFINITION --------------//
//###############################################//
//thin film height
lz_tf := 20e-9
//spacer between thin film and periodic structure/grating
sz := 0e-9
//Width of the periodic structures
dx := 110e-9
//Horizontal spacing between perdiodic structures
sx := 490e-9
//Etch depth of the periodic structures
dz := 20e-9
//Spacing between sample and antenna (z-dir)
s_ant := 0e-9
//Total simulation box height
lz := dz + sz + s_ant + lz_tf

//Sample lenghts/measurements in all spatial directions
//Set the unit-cell size to include n_wires nanowires
n_wires := 3
```

```
23 lx := n_wires*(dx + sx)
24 ly := 200e-9
25
26 /////Material parameters
27 //YIG
28 TF_Msat := 140e+3
29 TF_Aex := 3e-12
30 TF_alpha := 8e-5
31
32 //Co
33 NG_Msat := 1430e+3
34 NG_Aex := 13e-12
35 NG_alpha := 0.01
36
37
38 //Calculate the minimal exchange length of the system
39 lex_tf := sqrt(TF_Aex / (0.5 * mu0 * pow(TF_Msat, 2)))
40 lex_ng := sqrt(NG_Aex / (0.5 * mu0 * pow(NG_Msat, 2)))
41 lex_1 := min(lex_tf, lex_ng)
42 print(sprintf("Smallest exhange length - %.3f nm", lex_1*1e9))
43
44
45 ////Initialize FEM grid
46 //grid cell dimensions (approx. start point; automatically adjusted)
47 cx := 5e-9
48 cy := 5e-9
49 cz := 20e-9
50
51 //Number of grid cells (preeliminary)
52 Nx := pow(2, ilogb(lx/cx))
53 Ny := pow(2, ilogb(ly/cy))
54 Nz := pow(2, ilogb(lz/cz))
55
56 //override values with the actually chosen grid size
57 cx = lx/Nx
58 cy = ly/Ny
59 cz = lz/Nz
60
61 //check if cell size is less than exchange length (in-plane)
62 //if yes, increase the cell density until fulfilled
63 for cx>lex_1{
```

```
64      Nx = pow(2, ilogb(lx/cx)+1)
65      print("Cells in x-dir too large!")
66      print(sprintf("Reduce %.3f nm --> %.3f nm", cx*1e9, lx/Nx*1e9))
67      cx = lx/Nx
68  }
69
70  for cy>lex_1{
71      Ny = pow(2, ilogb(ly/cy)+1)
72      print("Cells in y-dir too large!")
73      print(sprintf("Reduce %.3f nm --> %.3f nm", cy*1e9, ly/Ny*1e9))
74      cy = ly/Ny
75  }
76
77
78  print(sprintf("Chosen Num. of cells: %f - %f - %f", Nx, Ny, Nz))
79
80  //periodic boundary conditions
81  PBCx := 100
82  PBCy := 100
83  PBCz := 0
84  SetMesh(Nx, Ny, Nz, lx/Nx, ly/Ny, lz/Nz, PBCx, PBCy, PBCz)
85
86  //edgesmoothing to better resolve edges of structure
87  Edgesmooth = 8
88
89  //override values with the actually chosen grid size
90  cx = lx/Nx
91  cy = ly/Ny
92  cz = lz/Nz
93
94
95
96
97  //################################################//
98  //-------------- SIMULATION PARAMS --------------//
99  //################################################//
100 //Define external Bias field
101 //FMR sweep parameterss
102 B_stat_max := 0.2
103 B_stat_min := -0.2
104 B_stat_step := 1e-3
```

```
105 N := trunc(abs(B_stat_max - B_stat_min)/B_stat_step)
106 B_stat := B_stat_max
107
108 //azimuth
109 phi := 89 * (pi/180)
110 //polar
111 theta := pi/2
112
113
114 //Define microwave excitation strength
115 //frequency [Hz]
116 f := 100e+9
117 //amplitude [T]
118 B_rf := 1e-3
119 //delay of the sinc pulse [s]
120 t_p := 100e-12
121
122 //Define the simulation time parameters
123 //Total simulated timespan (for each run) [s]
124 T_total := 20e-9
125 //Sampling interval for table and magnetization [s]
126 t_sample := 5e-12
127 //Total steps
128 N_T := trunc(T_total/t_sample)
129
130
131
132 //################################################//
133 //------------- OUTPUT CONFIG --------------//
134 //################################################//
135 outputformat = OVF2_TEXT
136 //Add (averaged) quantities to the output table
137 TableAdd(B_ext)
138 TableAddVar(B_stat, "B_stat", "T")
139 TableAdd(dt)
140 TableAddVar(t_sample, "t_sample", "s")
141 //Define saving interval
142 tableautosave(t_sample)
143
144
145 //////Timing and performance eval: Variable declaration
```

```
146 count := 0
147 count1 := 0
148 tic := Now()
149 tic_r := Now()
150 tic_s := Now()
151
152 mins := Since(tic).Minutes()
153 mins_r := Since(tic).Minutes()
154 mins_s := Since(tic).Minutes()
155
156 secs := Since(tic).Seconds()
157 secs_r := Since(tic).Seconds()
158 secs_s := Since(tic).Seconds()
159
160 hs := Since(tic).Hours()
161 eta_ms := Since(tic).Minutes()
162 eta_s := Since(tic).Seconds()
163 eta_hs := Since(tic).Hours()
164
165
166 //##############################################//
167 //-------------- SAMPLE GEOMETRY ---------------//
168 //##############################################//
169 //Define the nanograting
170 wire := cuboid(dx, ly, dz)
171 grating := wire.repeat(dx+sx, 0, 0).transl(0, 0, lz/2-dz/2-s_ant)
172 //Define the thin film
173 tf := cuboid(lx, ly, lz_tf).transl(0, 0, -lz/2+lz_tf/2-s_ant)
174
175 //set the geometry and save it
176 setgeom(tf.add(grating))
177 save(geom)
178
179 //Define material regions and save them!
180 defregion(1, tf)
181 defregion(2, grating)
182 save(regions)
183
184 //Assign material parameters to the regions
185 msat.setregion(1, TF_Msat)
186 alpha.setregion(1, TF_alpha)
```

```
187 aex.setregion(1, TF_Aex)
188 msat.setregion(2, NG_Msat)
189 alpha.setregion(2, NG_alpha)
190 aex.setregion(2, NG_Aex)
191
192 //Add the averaged response of the separate material regions to the output table
193 TableAdd(m.region(1))
194 TableAdd(m.region(2))
195
196
197 //###############################################//
198 //------------- CONF INITIAL STATE -------------//
199 //###############################################//
200
201 //Initialize the system with randomized magnetization in each cell
202 m = randommag()
203
204 //Save picture of magnet as .jpg as confirmation
205 snapshot(m)
206
207 //Apply strongest static field value and repeat steps
208 B_ext = vector(B_stat_max*sin(theta)*cos(phi),
209                B_stat_max*sin(theta)*sin(phi) ,
210                B_stat_max*cos(theta))
211 Relax()
212 snapshot(m)
213
214
215
216
217 //###############################################//
218 //--------------- RUN SIMULATION ---------------//
219 //###############################################//
220
221 tic = Now()
222
223 //Run field sweep simulation
224 for B_stat=B_stat_max; B_stat>=B_stat_min; B_stat-=B_stat_step{
225     t = 0
226
227     //Apply bias field, then relax structure
```

```
228     B_ext = vector(B_stat*sin(theta)*cos(phi),
229                    B_stat*sin(theta)*sin(phi),
230                    B_stat*cos(theta))
231     tic_r = Now()
232     Relax()
233     secs_r = Since(tic_r).Seconds()
234
235
236     //Run the time dynamics simulation
237     B_ext = vector(B_stat*sin(theta)*cos(phi) + B_rf*sinc(2*pi*f*(t-t_p)),
238             B_stat*sin(theta)*sin(phi),
239             B_stat*cos(theta))
240
241     tic_s = Now()
242     tableautosave(t_sample)
243     run(T_total)
244     mins_s = Since(tic_s).Minutes()
245     secs_s = Since(tic_s).Seconds()
246
247
248     //Keep track of the time consumed per evaluation in the console
249     if mins_s<1.0 {
250     print(sprintf("@%.5gT - Min:%.2fs - Sim:%.2fs", B_stat, secs_r, secs_s))
251     }
252     if mins_s>=1.0 {
253     secs_s = secs_s - 60*floor(mins_s)
254     print(sprintf("@%.5gT - Min:%.2fs - Sim:%.0fm %.2fs", B_stat, secs_r,
255          floor(mins_s), secs_s))
256     }
257
258     count += 1
259     count1 += 1
260
261     if count1 >= 10 {
262         hs = Since(tic).Hours()
263         mins = Since(tic).Minutes()
264         hs = hs - trunc(mins/60)
265         secs = Since(tic).Seconds()
266         secs = secs - trunc(mins)*60
267
268         eta_s = secs*(N-count)
```

```
269             eta_hs = Trunc(eta_s/3600)
270             eta_ms = Trunc(eta_s/60) - 60*eta_hs
271             eta_s = eta_s - (3600*eta_hs + 60*eta_ms)
272
273             print(sprintf("Elapsed: %.0f h:%.0f m:%.2f s", hs, mins, secs))
274             print(sprintf("--> ETA:%2.0f:%2.0f:%2.0f", eta_hs, eta_ms, eta_s))
275             print("")
276             count1 = 0
277         }
278
279     }
```

B.1.2 MuMax^3 sample code for spin wave transport

```
1   OutputFormat = OVF2_TEXT
2   //###############################################//
3   //------------- SAMPLE DEFINITION --------------//
4   //###############################################//
5   //thin film height
6   lz_tf := 20e-9
7   //spacer between thin film and periodic structure/grating
8   sz := 0e-9
9   //Width of the periodic structures
10  dx := 110e-9
11  //Horizontal spacing between perdiodic structures
12  sx := 490e-9
13  //Etch depth of the periodic structures
14  dz := 20e-9
15  //Spacing between sample and antenna (z-dir)
16  s_ant := 0e-9
17  //Total simulation box height
18  lz := dz + sz + s_ant + lz_tf
19
20  //Sample lenghts/measurements in all spatial directions
21  //Set the unit cell to include large number of nanowires (n_wires)
22  n_wires := 99
23  lx := n_wires*(dx + sx)
24  ly := 200e-9
25  /////Material parameters
26  //YIG
27  TF_Msat := 140e+3
```

```
28 TF_Aex := 3e-12
29 TF_alpha := 8e-5
30
31 //Co
32 NG_Msat := 1430e+3
33 NG_Aex := 13e-12
34 NG_alpha := 0.01
35
36
37 //Calculate the minimal exchange length of the system
38 lex_tf := sqrt(TF_Aex / (0.5 * mu0 * pow(TF_Msat, 2)))
39 lex_ng := sqrt(NG_Aex / (0.5 * mu0 * pow(NG_Msat, 2)))
40 lex_1 := min(lex_tf, lex_ng)
41 print(sprintf("Smallest exhange length - %.3f nm", lex_1*1e9))
42
43
44 ////Initialize FEM grid
45 //grid cell dimensions (approx. start point; automatically adjusted)
46 cx := 3e-9
47 cy := 3e-9
48 cz := 20e-9
49
50 //Number of grid cells (preeliminary)
51 Nx := pow(2, ilogb(lx/cx))
52 Ny := pow(2, ilogb(ly/cy))
53 Nz := pow(2, ilogb(lz/cz))
54
55 //override values with the actually chosen grid size
56 cx = lx/Nx
57 cy = ly/Ny
58 cz = lz/Nz
59
60 //check if cell size is less than
61 //.75 (transp.) exchange length (in-plane)
62 //if yes, increase the cell density until fulfilled
63 for cx>0.75*lex_1{
64     Nx = pow(2, ilogb(lx/cx)+1)
65     print("Cells in x-dir too large!")
66     print(sprintf("Reduce %.3f nm --> %.3f nm", cx*1e9, lx/Nx*1e9))
67     cx = lx/Nx
68 }
```

```
69
70  for cy>0.75*lex_1{
71      Ny = pow(2, ilogb(ly/cy)+1)
72      print("Cells in y-dir too large!")
73      print(sprintf("Reduce %.3f nm --> %.3f nm", cy*1e9, ly/Ny*1e9))
74      cy = ly/Ny
75  }
76
77
78  print(sprintf("Chosen Num. of cells: %f - %f - %f", Nx, Ny, Nz))
79  //periodic boundary conditions
80  //use no pbc for the transport direction
81  PBCx := 0
82  PBCy := 100
83  PBCz := 0
84  SetMesh(Nx, Ny, Nz, lx/Nx, ly/Ny, lz/Nz, PBCx, PBCy, PBCz)
85
86  //edgesmoothing to better resolve edges of structure
87  Edgesmooth = 8
88
89  //override values with the actually chosen grid size
90  cx = lx/Nx
91  cy = ly/Ny
92  cz = lz/Nz
93
94
95  /////Specifications of the antenna
96  //desired number of points in k_space
97  Nc := 1000
98  //cut off momentum
99  kc := Nc/2 * 2*pi/lx
100 //offset of excitation peak from sample middle (x-dir)
101 d_cc := 0
102
103
104
105 //################################################//
106 //------------- SIMULATION PARAMS --------------//
107 //################################################//
108 //Define external Bias field
109 //For transport: fixed static field, no sweep
```

```
B_stat := 50e-3
//azimuth
phi := 89 * (pi/180)
//polar
theta := pi/2

//Define microwave excitation strength
//frequency [Hz]
f := 100e+9
//amplitude [T]
B_rf := 1e-3
//delay of the sinc pulse [s]
t_p := 50e-12

//Define the simulation time parameters
//Total simulated timespan (for each run) [s]
T_total := 20e-9
//Sampling interval for table and magnetization [s]
t_sample := 5e-12
//Total steps
N_T := trunc(T_total/t_sample)



//################################################//
//-------------- OUTPUT CONFIG --------------//
//################################################//
outputformat = OVF2_TEXT
//Add (averaged) quantities to the output table
TableAdd(B_ext)
TableAddVar(B_stat, "B_stat", "T")
TableAdd(dt)
TableAddVar(t_sample, "t_sample", "s")
//Define saving interval
tableautosave(t_sample)



//################################################//
//-------------- SAMPLE GEOMETRY ---------------//
//################################################//
```

```
151 //Define the nanograting
152 wire := cuboid(dx, ly, dz)
153 grating := wire.repeat(dx+sx, 0, 0).transl(0, 0, lz/2-dz/2-s_ant)
154
155 //Define the thin film
156 tf := cuboid(lx, ly, lz_tf).transl(0, 0, -lz/2+lz_tf/2-s_ant)
157
158 //set the geometry and save it
159 setgeom(tf.add(grating))
160 save(geom)
161
162 //Define material regions and save them!
163 defregion(1, tf)
164 defregion(2, grating)
165 save(regions)
166
167 //Assign material parameters to the regions
168 msat.setregion(1, TF_Msat)
169 alpha.setregion(1, TF_alpha)
170 aex.setregion(1, TF_Aex)
171 msat.setregion(2, NG_Msat)
172 alpha.setregion(2, NG_alpha)
173 aex.setregion(2, NG_Aex)
174
175
176 //Manually add the avr magnn. of each wire to the table
177 //This is done by manually calculating the cell indices
178 //and cropping the magnetization to the respective cell ranges
179 for z_idx:=Nz-1; z_idx>=0; z_idx--{
180     for i:=0; i<n_wires; i++{
181         x := -lx/2 + (i+1/2)*(dx + sx)
182
183         //Add the wire
184         TableAdd(Crop(m, trunc((x+lx/2-dx/2)/cx),
185                          trunc((x+lx/2+dx/2)/cx)+1,
186                          0,
187                          Ny,
188                          z_idx,
189                          z_idx+1))
190
191         //Add the inter-wire spacing to the right
```

```
192         //of the current wire
193         if i<(n_wires-1){
194             TableAdd(Crop(m, trunc((x+lx/2+dx/2)/cx),
195                              trunc((x+lx/2+dx/2+sx)/cx)+1,
196                              0,
197                              Ny,
198                              z_idx,
199                              z_idx+1))
200         }
201     }
202 }
203
204 //################################################//
205 //------------- CALC ANTENNA FIELD -------------//
206 //################################################//
207 //Create vector mask array for the field distribution of the spatial sinc
208 //Vector mask to save field vectors in
209 mask := newVectorMask(Nx, Ny, Nz)
210
211 //Initialize vector norm as a float number
212 max_norm := 0.1
213 vec_norm := 1.2
214
215 for i:=0; i<Nx; i++{
216     for k:=0; k<Nz; k++{
217         r := index2coord(i, 0, k)
218         x := r.X() + d_cc
219         z := lz/2 - r.Z()
220
221         //Field at i, k from cc (Karlqvist equations)
222         vec_cc := vector(sinc(kc*x), 0, 0)
223
224         //Calc Norm of current vector and compare
225         //to previous one (Find max norm)
226         vec_norm = sqrt(pow(vec_cc.X(),2)+pow(vec_cc.Y(),2)+pow(vec_cc.Z(),2))
227         max_norm = max(vec_norm, max_norm)
228
229         //Set the vector as field direction along
230         //all y-coordinates y (for the x, z)
231         for j:=0; j<Ny; j++{
232             mask.SetVector(i, j, k, vec_cc)
```

```
233         }
234     }
235 }
236
237
238
239
240 //################################################//
241 //------------- CONF INITIAL STATE -------------//
242 //################################################//
243
244 //Initialize the system with randomized magnetization in each cell
245 m = randommag()
246
247 //Save picture of magnet as .jpg as confirmation
248 snapshot(m)
249
250 //Apply strongest static field value and repeat steps
251 B_ext = vector(B_stat*sin(theta)*cos(phi),
252                B_stat*sin(theta)*sin(phi),
253                B_stat*cos(theta))
254 Relax()
255 snapshot(m)
256
257
258
259
260 //################################################//
261 //--------------- RUN SIMULATION ---------------//
262 //################################################//
263 //Relax the structure to get constant magnetization
264 Relax()
265
266 //Add the sinc-shaped excitation field for the dynamic pulse
267 B_ext.Add(mask, B_rf*sinc(2*pi*f*(t-t_p)))
268
269 //Run simulation
270 run(T_total)
```

B.2 Post-processing

B.2.1 Python code to obtain FMR spectrum

```
import numpy as np
import pandas as pd
import scipy as sp
import matplotlib.pyplot as plt
import matplotlib.colors as colors
from collections import Counter
import scipy as sp
import scipy.signal as signal


def calc_susceptibility(df:pd.DataFrame, dt:float, interpolate=False,
                        BiasFieldDir='y', MWFieldDir='x'):
    """
    Takes as input the output "table.txt" of a mumax3 simulation.
    Calculates the systems dynamic susceptibility.

    Inputs----------------------------------------------------
    df: pd.Dataframe (loaded table.txt)
    dt: sampling rate of the simulation in seconds (saving interval)
    interpolate: choose wether interpolation of input data is performed
    BiasFieldDir: direction of the external (static) field
    MWFieldDir: direction of the (dynamic) microwave field


    Returns---------------------------------------------------
    fields: np.array with swept (static) external field values
    f: np.array with the (positive) frequency axis
    X: np.array containing the susceptibility X,
       frequency values along the rows, field values along columns
    """

    ###########################################################################
    ###----------------------- INPUT HANDLING ----------------------------##
    ###########################################################################

    if BiasFieldDir.lower() not in ['x', 'y', 'z']:
        raise ValueError("Bias field direction can only be 'x', 'y' or 'z'.")
```

```
38      else: BiasFieldDir = BiasFieldDir.lower()
39
40      if MWFieldDir.lower() not in ['x', 'y', 'z']:
41          raise ValueError("Microwave field direction can only be 'x', 'y' or 'z'.")
42      else: MWFieldDir = MWFieldDir.lower()
43
44
45      ##########################################################################
46      ###-----------------------   Processing   ----------------------------##
47      ##########################################################################
48
49      #Check if 'B_stats' provided -> If yes it gives the swept field values
50      if "B_stat (T)" in df.columns.to_list():
51          Use_B_stats = True
52      else:
53          Use_B_stats = False
54
55      #If not provided, use the user input to find the swept field values
56      if Use_B_stats:
57          B_stats = df["B_stat (T)"].unique()
58      else:
59          B_stats = df[f"B_ext{BiasFieldDir} (T)"].unique()
60
61      #Create lists to store swept field values and corresponding FFT(m(t))
62      FFTs = []
63      fields = []
64
65      #Keep track of lengths to identify possible incomplete simulation runs
66      Ls = []
67
68      #Sweep through field values
69      for i in range(len(B_stats)):
70          #Grab data recording during current field value
71          if Use_B_stats:
72              df_1 = df[df["B_stat (T)"]==B_stats[i]].copy()
73          else:
74              df_1 = df[df[f"B_ext{BiasFieldDir} (T)"]==B_stats[i]].copy()
75
76          #Remove potential duplicates
77          #(timepoints that have been recorded mult. times)
78          df_1 = df_1.drop_duplicates(subset="# t (s)")
```

```
79
80          #Extract data vectors for current field value
81          t = df_1["# t (s)"].to_numpy()
82          m = df_1[f"m{MWFieldDir} ()"].to_numpy()
83
84          #If interpolata==True: interpolate the data to obtain even timestep
85          if interpolate:
86              spl = sp.interpolate.CubicSpline(t, m)
87              t = np.linspace(0, np.max(t), int(np.max(t)/dt), endpoint=True)
88              m = spl(t)
89
90          #Calculate FFT(m(t)) (for positive frequencies)
91          L = len(t)
92          FFT = np.fft.fft(m)[0:int(L/2)]
93
94          #Append results to lists
95          Ls.append(L)
96          FFTs.append(FFT)
97          fields.append(B_stats[i])
98
99      #Find out if there are incomplete simulation runs
100     Ls = np.array(Ls)
101     L_vals, L_counts = np.unique(Ls, return_counts=True)
102     #Sort unique values by their number of occurences
103     L_vals = L_vals[np.argsort(-L_counts)]
104     L = L_vals[0]
105     if len(L_vals)>1:
106         print("\nNot all simulation runs of equal length!")
107         #Go through all L values that are not the maximum count
108         for j in range(len(L_vals)-1):
109             #Find the indices corresponding to the current L value
110             indices = [i for i,x in enumerate(Ls) if x == L_vals[j+1]]
111
112             for index in sorted(indices, reverse=True):
113                 print(f"Removing sim run of B_stat = {fields[index]}")
114                 del FFTs[index]
115                 del fields[index]
116
117
118     #Get the frequency axis (positive half)
119     f = np.fft.fftfreq(L, d=dt)[0:int(L/2)]
```

```
120
121     #Construct spectrum array
122     fields = np.array(fields)
123     FFTs = np.array(FFTs)
124
125     #Transposing the array returns array of shape
126     FFTs = np.transpose(FFTs)
127
128     #   ^    (   |     |     |          )
129     #   |    ( m(f)  m(f)  m(f) .....  )
130     #   f    (   |     |     |          )
131     #   |
132     #        --------B_stats---------->
133
134
135     #Calculate the suceptibility X by deriving w/ respect to B_stat
136     if fields.shape[0]>1: X = np.gradient(FFTs, axis=1)
137     else:
138         print("No field sweep. Returning m(f) insteand of susceptibility.")
139         X = FFTs
140
141     return fields, f, X
```

B.2.2 Python code to fit FMR spectrum

```
1  import numpy as np
2  import pandas as pd
3  import scipy as sp
4  import matplotlib.pyplot as plt
5  import matplotlib.colors as colors
6  from collections import Counter
7  import scipy as sp
8  import scipy.signal as signal
9
10
11
12 def fit_spectrum_peaks(X:np.array, f:np.array, fields:np.array,
13                         num_peaks:int, num_points:int,
14                         peak_prom:float = 1e-3, min_peak_freq=1,
15                         max_peak_freq=np.inf, Verbose=False):
16     """
```

```
17      Takes a spectrum as input (e.g. S21 or X) and fits a
18      sum of <num_peaks> Lorentzians to the respective field slices.
19      Note that the fit is done in a converted spectrum of T vs GHz.
20      Thus the output data is in units T/GHz respectively.
21      It is recommended to unpack the fit data using Params2Arrays().
22
23      Inputs----------------------------------------------------
24      X: np.array containing the spectral data
25      f: np.array containing the swept frequencies (i.e. y-axis of X)
26      fields: np.array containing the swept ext. fields (i.e. x-axis of X)
27      num_peaks: int, # peaks to (maximally) fit per slice
28                  -> number of modes desired
29      num_points: int, # of datapoints to return
30                  -> Number of field slices to be fitted
31
32      Optional:
33      peak_prom:  float, default = 1e-3:
34                  Filter factor of peak prominences for point
35                  to be considered a peak in the data
36      min_peak_freq:  float, default = 1:
37                      Minimum frequency value of a point to be considered a peak.
38                      This helps avoiding fitting artifacts in FFT data
39      max_peak_freq:  float, default = np.inf:
40                      Maximum frequency a point is allowed to have
41                      to be considered a peak
42      Verbose:    bool, default = False:
43                  If true, prints statements for failed fits
44
45
46      Returns---------------------------------------------------
47      fit_idx: list of all slice indices that were fit successfully
48      params: list of the fit parameters for all fitted peaks in pairs of 3:
49              First column: Intensity of the peak
50              Second column: Peak location (fres)
51              Third column: HWHM (Multiplied by 2 gives FWHM or \Delta f)
52
53      params_err: list of the uncertainties to params organized in the same way
54      """
55
56      #Define the fitting funtions
57      def Lorentzian(x, I, x0, gamma):
```

```
58          return I * (gamma**2)/((x-x0)**2 + gamma**2)
59
60      def sum_of_lorentzians(x, *params):
61          # Each Lorentzian has 3 parameters (A, x0, gamma)
62          num_peaks = len(params) // 3
63          result = np.zeros_like(x)
64          for i in range(num_peaks):
65              A = params[i * 3]
66              x0 = params[i * 3 + 1]
67              gamma = params[i * 3 + 2]
68              result += Lorentzian(x, A, x0, gamma)
69          return result
70
71      #Create empty lists to store fitting data
72      fit_idx = []     #indices of field slices that were (successfully) fitted
73      fit_p = []       #frequency value of fitted Lorentzian peak (f_res)
74      fit_p_err = []   #errors on resonance frequencies (\Delta f_res)
75
76      #Stepsize along the field axis
77      n = int(X.shape[1]/num_points)
78      #If step size is chosen too high, use every available data slice
79      if num_points>X.shape[1]:
80          if Verbose: print("Too many points chosen! Fitting all possible slices")
81          n = 1
82
83      #Iterate through field slices
84      for i in range(0, X.shape[1], n):
85          data = X[:, i]
86
87          #Determine peaks and sort them (descending order) by prominence
88          peaks, _ = signal.find_peaks(data, prominence=peak_prom*np.max(data))
89          prominences = signal.peak_prominences(data, peaks)[0]
90          sorted_peaks = [peak for _, peak in sorted(zip(prominences, peaks),
91                                                     reverse=True)]
92
93          #Check if minimum frequency condition is met
94          sorted_peaks = [peak for peak in sorted_peaks if f[peak]*1e-9>=min_peak_freq]
95
96          #If more peaks were found than fitted peaks desired
97          #->omit those of weaker prominence
98          if len(sorted_peaks)>num_peaks:
```

```
99              sorted_peaks = sorted_peaks[0:num_peaks]
100
101         #Construct initial guess for the Lorentzian fits
102         init_guess = []
103         for j in range(len(sorted_peaks)):
104             peak_idx = sorted_peaks[j]
105             # Amplitude, position, width
106             init_guess.extend([data[peak_idx], f[peak_idx]*1e-9, 0.1])
107
108
109         #Fit using sum of <num_peaks> Lorentzians
110         try:
111             popt, pcov = sp.optimize.curve_fit(sum_of_lorentzians,
112                                                f*1e-9, data,
113                                                p0=init_guess)
114             fit = True
115
116         except:
117             if Verbose:
118                 print(f"Fit didn't converge @ {fields[i]:.4f}T")
119             fit = False
120
121
122         #If fit was successful:
123         #note this in the list of fit_idx and save parameters
124         if fit:
125             fit_p.append(popt)
126             fit_p_err.append(np.sqrt(np.diag(pcov)))
127             fit_idx.append(i)
128
129
130     fit_idx = fit_idx
131     params = fit_p
132     params_err = fit_p_err
133
134     return fit_idx, params, params_err
135
136
137 def Params2Arrays(fields:list, fit_idx:list, params:list, params_err:list):
138     """
139     Takes lists of output of fit_spetrum_peaks() and
```

```
140         converts them into a sorted output dict "arrays".
141
142         Structure of output-dict:
143         1.First key gives the modenumber
144           (Fitted points associated with the <modenumber> most prominent peak)
145           Example: arrays[0] gives the data dict for the most prominent mode
146
147         2.Second-level key gives the desired quantity in regards to the mode fit.
148           Current options: 'field', 'fpeaks', 'fpeaks_err', 'deltaf', 'deltaf_err'
149           Example: arrays[0]['fpeaks'] gives peak freqs @ fields arrays[0]['field']
150         """
151
152         #Determine number of modes as maximum length of sublist in params
153         N = max([len(list) for list in params])
154
155         #Create dicts of emtpy lists w/ respective name for each mode
156         arrays = {}
157         for i in range(N):
158             arrays[i] = {'field(T)':[],
159                          'fpeaks(GHz)':[], 'fpeaks_err(GHz)':[],
160                          'deltaf(GHz)':[], 'deltaf_err(GHz)':[]}
161
162         #Iterate through params list
163         for i in range(len(params)):
164             #iterate through the number of fitted peaks
165             for j in range(int(len(params[i])/3)):
166                 #Store information in relevant arrays
167                 arrays[j]['field(T)'].extend([fields[fit_idx[i]]])
168
169                 arrays[j]['fpeaks(GHz)'].extend([params[i][1 + 3*j]])
170                 arrays[j]['fpeaks_err(GHz)'].extend([params_err[i][1 + 3*j]])
171
172                 arrays[j]['deltaf(GHz)'].extend([2*params[i][2 + 3*j]])
173                 arrays[j]['deltaf_err(GHz)'].extend([2*params_err[i][2 + 3*j]])
174
175         #Transform into npy arrays before returning
176         for modenum in list(arrays.keys()):
177             for quant in list(arrays[modenum].keys()):
178                 arrays[modenum][quant] = np.array(arrays[modenum][quant])
179
180
```

```
181     return arrays
182 
183 def sort_arrays_by_frequency(arrays):
184     """
185     Sorts the output dictionary of Params2Arrays function.
186     Retursn dict sorted by descending frequency values in 'fpeaks(GHz)'.
187     """
188     # Define custom key function to extract frequency value
189     def get_frequency(arr):
190         # If 'fpeaks(GHz)' is empty, return a high value
191         # This sorts it to the end later
192         if arr['fpeaks(GHz)']:
193             return arr['fpeaks(GHz)'][0]
194         else:
195             # Assign a high value for empty 'fpeaks(GHz)'
196             return float('inf')
197 
198     # Sort the dictionary based on frequency values for each mode
199     sorted_arrays = {k:v for k,v in sorted(arrays.items(),
200                                            key=lambda x: get_frequency(x[1]))}
201 
202     return sorted_arrays
```

B.2.3 Python code to obtain continuous medium spin wave dispersion

```
1  import numpy as np
2  import pandas as pd
3  import scipy as sp
4  import os
5  import re
6  from glob import glob
7  import multiprocessing
8  from functools import partial
9  import matplotlib as mpl
10 import matplotlib.pyplot as plt
11 
12 def dispersion_from_files_multithread(out_dir:str, comp='x',
13                                       dt=5e-12, filepat="m.region1[0-6]*"):
14     """
15     Calculates spin wave dispersion spectrum for a mumax3 simulation.
```

```
16
17      Inputs-----------------------------------------------------
18      out_dir:    str,
19                  dir containing the spatial .ovf output files
20
21      Optional
22      comp:       str, default 'x'.
23                  Desired dispersion component (i.e., kx)
24      dt:         float, default 5e-12s
25                  Sample rate of the mumax3 simulation
26      filepat:    str, default "m.region1[0-6]*"
27                  Regex pattern of the files to evaluate.
28
29
30      Returns----------------------------------------------------
31      k:          np.array of the sampled momenta
32      f:          np.array of the sampled (positive) frequencies
33      m_w_k:      np.array containing the spin wave dispersion spectrum,
34                  frequency values along the rows,
35                  field values along columns
36      """
37
38      #Remember current working directory
39      cwd = os.getcwd()
40      #Go to output directory
41      os.chdir(out_dir)
42
43      #Get list of the output magnetization files
44      m_files = glob(f"{filepat}.ovf")
45
46      #Translate the comp input to an index
47      comp_indices = {'x':0, 'y':1, 'z':2}
48      if comp.lower() in comp_indices: comp_idx = comp_indices[comp]
49      else: raise ValueError("comp has to be 'x', 'y' or 'z.")
50
51      #Manually determine the node dimensions in a first step
52      first_file = ovf.ovf_file(m_files[0])
53      xdim = int(first_file.xnodes)
54      ydim = int(first_file.ynodes)
55      zdim = int(first_file.znodes)
56
```

```
57      #Also determine the spacing in transport direction for FFT later
58      dx = float(first_file.xbase)
59      #Remove first_file from memory
60      del(first_file)
61
62      #Load in the remaining arrays multi-threaded
63      with multiprocessing.get_context("spawn").Pool() as pool:
64          multi_thread_files = list(pool.map(partial(ovf.loadarray,
65                                                     newshape=(zdim, ydim, xdim),
66                                                     column=comp_idx), m_files))
67      pool.close()
68      pool.join()
69
70      #Convert the file list to array
71      array = np.array(multi_thread_files)
72
73      #Release the file list from memory
74      del(multi_thread_files)
75
76      #Transpose array [t, z, y, x] ---> [t, x, y, z]
77      array = array.transpose((0,3,2,1))
78
79      #Calculate necessary window function
80      window_f = np.hanning(array.shape[0])
81      window_k = np.hanning(array.shape[1])
82      window_2D = np.sqrt(np.outer(window_f, window_k))
83
84      #Save memory: Use only in-place transformation for the FFTs
85      for y in range(array.shape[2]):
86          for z in range(array.shape[3]):
87              #Perform 2D FFT on windowed data
88              array[:, :, y, z] = np.abs(np.fft.fft2(window_2D*array[:, :, y, z]))
89
90      #Sum over the squared absolute values of |M_y_z (kx, f)|
91      #Finally, apply fftshift in order to get correct k-value alignment
92      m_w_k = np.fft.fftshift(np.sum(np.power(array, 2), axis=(2, 3)), axes=1)
93
94      #Get the frequency axes
95      k = np.fft.fftshift(np.fft.fftfreq(m_w_k.shape[1], d=dx))
96      f = np.fft.fftfreq(m_w_k.shape[0], d=dt)
97
```

```
98      #Remove array from memory
99      del(array)
100
101     #Return to original cwd
102     os.chdir(cwd)
103
104     #Return the spectral data
105     return k, f[:int(m_w_k.shape[0]/2)], m_w_k[:int(m_w_k.shape[0]/2), :]
```

B.2.4 Python code to obtain magnonic crystal spin wave dispersion

```
1  import numpy as np
2  import pandas as pd
3  import scipy as sp
4  import os
5  import re
6  from glob import glob
7  import multiprocessing
8  from functools import partial
9  import matplotlib as mpl
10 import matplotlib.pyplot as plt
11
12
13 def MagnonicCrystalDispersion_from_table(df:pd.DataFrame,
14                                          x:int, y:int, z:int,
15                                          a:float, dt:float):
16     """
17     Calculates the dispersion relation/spectrum P(f, kx)
18     in x-direction for 2D-Magnonic crystals from table.txt.
19     This function specifically takes tables as input, where columns
20     correspond to numerous crop-ins of the simulation grid.
21     Specifically, it is assumed that the crop-ins are ordered
22     from left to right and top to bottom.
23     These crops of the simulation grid are interpreted as "unit cells"
24
25     Input:-----------------------------------------------------------------
26     df:     pd.DataFrame, output table from mumax3
27     x:      int, number of "unit cells" in x-direction
28     y:      int, number of "unit cells" in y-direction
29     z:      int, number of "unit cells" in z-direction
30     a:      float, lattice constant of the "unit cells" (center-center)
```

```
31      dt:     float, sampling rate of table in seconds
32
33
34      Output:-----------------------------------------------------------------
35      k:      np.array, vector of momentum kx in [rad/m]
36      f:      np.array, vector of frequency f in [Hz]
37      m_f_k:  np.array, dispersion spectrum, f along rows, kx along columns
38      """
39
40      #If the single lattice sites of the magnonic crystal aren't defined as regions
41      #->rename them - Order: Left to right, Top to bottom
42      if df.filter(regex="m.region[0-9]+[xyz]").empty:
43          #Rename the columns if necessary
44          for comp in ['x','y','z']:
45              colnames = [col for col in df.columns if re.search(f"m_.*_{comp} ()", col
46              rename_dict = {}
47
48              for i in range(len(colnames)):
49                  rename_dict[colnames[i]] = f"m.region{i}{comp}"
50              df.rename(columns=rename_dict, inplace=True)
51
52      #Remove static magnetization
53      #df = df - df.iloc[0].squeeze()
54
55      #Loop over magnetization components, apply transformation
56      for comp in ['x','y','z']:
57          #Select subset of data
58          m_data = df.filter(regex=f"(?<=m.region)([0-9]+{comp})")
59          m_array = np.zeros(shape=(m_data.shape[0], x, y, z))
60
61          if comp=='x': m_f_k = np.zeros(shape=(m_data.shape[0], x, y, z))
62
63          #Reorder data on array reflecting proper magnonic crystal dimensions
64          counter = 0
65          for i in range(z):
66              for j in range(y):
67                  for k in range(x):
68                      m_array[:, k, j, i] = m_data.iloc[:, counter].to_numpy()
69                      counter += 1
70
71          #Calculate necessary window function
```

```
72          window_f = np.hanning(m_data.shape[0])
73          window_k = np.hanning(x)
74          window_2D = np.sqrt(np.outer(window_f, window_k))
75
76          #Apply FFT transformation
77          for i in range(y):
78              for j in range(z):
79                  m_f_k[:,:,i,j] += np.power(np.abs(
80                                    np.fft.fftshift(np.fft.fft2(
81                                    window_2D*m_array[:,:,i,j]), axes=(1))
82                                    ), 2)
83
84
85      #Apply FFT transformation
86      for i in range(y):
87          for j in range(z):
88              m_f_k[:,:,i,j] = np.sqrt(m_f_k[:,:,i,j])
89
90      #Shift the reciprocal arrays to fit plotting range
91      k = np.fft.fftshift(np.fft.fftfreq(n=x, d=a))
92      f = np.fft.fftfreq(n = m_data.shape[0], d=dt)
93      m_f_k = m_f_k[0:int(f.shape[0]/2),:,:,:]
94      f = f[0:int(f.shape[0]/2)]
95
96      return k, f, m_f_k
```

B.2.5 Python code to determine spatial mode profiles

```
1  def power_phase_pixelmap(out_dir:str, phase=False,
2                           filepat="m.region1[0-6]*",
3                           comps=[0,1,2]):
4      """
5      Creates a power/phase-pixelmap of a magnet
6      simulated in mumax3 from a top-down view.
7      The returned array has the frequency as first axis.
8      Choosing a frequency index i will give
9      the spectrum at the f[i].
10     Calculation of the spectra (after avr in z-dir for top-down view):
11     Power: spectrum = abs(sqrt(mx(f)^2 + my(f)^2 + mz(f)^2))
12     Phase: spectrum = unwrap(angle(mx(f) + my(f) + mz(f)))
13
```

```
14      Input:-------------------------------------------------------------
15      out_dir:    str, path to dir with the .ovf outputfiles
16      phase:      bool, choose between power or phase-pixelmap.
17                  (Default: False = Power spectrum)
18      filepat:    str, regex pattern to glob the corresponding .ovf files
19                  (Default: material region 1)
20
21
22      Output:------------------------------------------------------------
23      f:      np.array, vector containing the frequency f values in [Hz]
24      spectrum:  np.array, array of power/phase-spectrum with axes f, x, y
25      """
26
27      #Remember current working directory
28      cwd = os.getcwd()
29      #Go to output directory
30      os.chdir(out_dir)
31
32      #Get the table of the simulation
33      df = pd.read_csv("table.txt", sep='\t')
34
35      #Check if there is a duplicate for t
36      #(sometimes certain timepoints are recorded twice)
37      indices = df.duplicated(subset='# t (s)', keep='last').to_numpy()
38      if indices.any():
39          #drop duplicates out of the time series
40          df = df.drop_duplicates(subset="# t (s)")
41          #list of indices, where "# t (s)" has duplicate entries
42          double_indices = list(indices.nonzero()[0])
43
44
45      t = df["# t (s)"].to_numpy()
46      T = np.max(t)
47
48
49      #Get list of the output magnetization files
50      m_files = glob(f"{filepat}.ovf")
51
52      #Get the relevant spacing in time-space
53      try: dt = fmr.get_samplerate("log.txt")
54      except:
```

```
55          dt = 5e-12
56          print("No <log.txt> file found. Using default dt=5e-12s.")
57
58
59
60      #Manually determine the node dimensions in a first step
61      #-> Can use loadarray()
62      first_file = ovf.ovf_file(m_files[0])
63      xdim = int(first_file.xnodes)
64      ydim = int(first_file.ynodes)
65      zdim = int(first_file.znodes)
66
67      #determine the spacing in transport direction for FFT
68      dx = float(first_file.xbase)
69      #Remove first_file from memory again
70      del first_file
71
72      #Iterate through all components to get desired quantities
73      for comp_idx in comps:
74          #Load in the remaining arrays multi-threaded
75          with multiprocessing.get_context("spawn").Pool() as pool:
76              multi_thread_files = list(pool.map(partial(ovf.loadarray,
77                                                         newshape=(zdim, ydim, xdim),
78                                                         column=comp_idx), m_files)
79                                                         )
80          pool.close()
81          pool.join()
82
83
84          #Convert to array
85          array = np.array(multi_thread_files)
86
87          #Release list of files from memory after creating array
88          del multi_thread_files
89
90          #Transpose array [t, z, y, x] ---> [t, x, y, z]
91          array = array.transpose((0,3,2,1))
92
93          if indices.any():
94              total_indices = list(np.arange(array[:,0,0].shape[0]))
95              sel = list(set(total_indices).difference(set(double_indices)))
```

```
96          else:
97              sel = list(np.arange(array[:,0,0].shape[0]))
98
99          #Omit indices corresponding to double timepoints
100         array = array[sel,:,:]
101
102         #Average in z-direction
103         array = np.mean(array, axis=3)
104
105         #FFT in-place to conserve memory!
106         array = array.astype(np.complex128)
107
108
109
110         #Perform FFT for the time slices
111         for i in range(array.shape[1]):
112             for j in range(array.shape[2]):
113                 array[:,i,j] = np.fft.fft(array[:,i,j])
114
115         #Calculate the power/phase in frequency space
116         if comp_idx==0:
117             f = np.fft.fftfreq(array.shape[0], d=dt)
118             if phase: spectrum = np.angle(array)
119             else: spectrum = np.power(array, 2)
120
121         else:
122             if phase: spectrum += np.angle(array)
123             else: spectrum += np.power(array, 2)
124
125         #Release array from memory
126         del array
127
128     #Final processing on the spectra
129     if phase:
130         #unwrap takes the phase signal to the interval (-pi, pi],
131         #i.e., removing phases larger than 2pi
132         spectrum = np.unwrap(spectrum[:int(len(f)/2),:,:], axis=0)
133     else:
134         spectrum = np.abs(np.sqrt(spectrum[:int(len(f)/2),:,:]))
135
136     #Crop to positive frequencies
```

```
137     f = f[:int(len(f)/2)]
138     spectrum = spectrum[:int(len(f)/2),:,:]
139 
140     os.chdir(cwd)
141 
142     return f, spectrum
```

Bibliography

[1] Goldman Sachs. *AI is Poised to Drive 160% Increase in Data Center Power Demand*. May 2024. URL: https://www.goldmansachs.com/intelligence/pages/AI-poised-to-drive-160-increase-in-power-demand.html (visited on 23/05/2024).

[2] Richard Van Noorden and Richard Webb. *ChatGPT and Science: The AI System Was a Force in 2023 — For Good and Bad*. Dec. 2023. URL: https://www.nature.com/articles/d41586-023-03930-6 (visited on 23/05/2024).

[3] Thomas N. Theis and H.-S. Philip Wong. 'The End of Moore's Law: A New Beginning for Information Technology'. In: *Computing in Science Engineering* 19.2 (2017), pp. 41–50. DOI: 10.1109/MCSE.2017.29.

[4] V V Kruglyak, S O Demokritov and D Grundler. 'Magnonics'. In: *Journal of Physics D: Applied Physics* 43.26 (July 2010), p. 260301. DOI: 10.1088/0022-3727/43/26/260301. URL: https://dx.doi.org/10.1088/0022-3727/43/26/260301.

[5] Philipp Pirro et al. 'Advances in coherent magnonics'. In: *Nature Reviews Materials* 6.12 (2021), pp. 1114–1135. DOI: 10.1038/s41578-021-00332-w. URL: https://doi.org/10.1038/s41578-021-00332-w.

[6] A. V. Chumak. *Fundamentals of magnon-based computing*. 2019. arXiv: 1901.08934 [cond-mat.mes-hall].

[7] Jilei Chen, Haiming Yu and Gianluca Gubbiotti. 'Unidirectional spin-wave propagation and devices'. In: *Journal of Physics D: Applied Physics* 55.12 (Nov. 2021), p. 123001. DOI: 10.1088/1361-6463/ac31f4. URL: https://dx.doi.org/10.1088/1361-6463/ac31f4.

[8] Tao Yu et al. 'Chiral excitation of spin waves in ferromagnetic films by magnetic nanowire gratings'. In: *Phys. Rev. B* 99 (13 Apr. 2019), p. 134424. DOI: 10.1103/PhysRevB.99.134424. URL: https://link.aps.org/doi/10.1103/PhysRevB.99.134424.

[9] Tao Yu, Yaroslav M. Blanter and Gerrit E. W. Bauer. 'Chiral Pumping of Spin Waves'. In: *Phys. Rev. Lett.* 123 (24 Dec. 2019), p. 247202. DOI: 10.1103/PhysRevLett.123.247202. URL: https://link.aps.org/doi/10.1103/PhysRevLett.123.247202.

[10] Jilei Chen et al. 'Excitation of unidirectional exchange spin waves by a nanoscale magnetic grating'. In: *Phys. Rev. B* 100 (10 Sept. 2019), p. 104427. DOI: 10.1103/PhysRevB.100.104427. URL: https://link.aps.org/doi/10.1103/PhysRevB.100.104427.

[11] Christian Mang. *Unidirectional spin wave propagation in magnetic nanograting/thin film heterostructures*. Master's thesis. Available at https://example.com/thesis.pdf. Munich, Germany, Apr. 2023.

[12] Rudolf Gross and Achim Marx. *Festkörperphysik*. De Gruyter Oldenbourg, 2014. ISBN: 978-3-11-035870-4. DOI: doi:10.1524/9783110358704. URL: https://doi.org/10.1524/9783110358704.

[13] Lukas Liensberger. 'Magnon Hybrid Dynamics'. en. PhD thesis. Technische Universität München, 2021, p. 183.

[14] Troy Dion. 'Study of High Frequency Magnetisation Dynamics in Artificial Nanomagnets Using Micromagnetic Simulation and Spin Wave Spectroscopy'. Doctoral Thesis. UCL (University College London), 2020.

[15] Terunobo Miyazaki and Hanmin Jin. *The Physics of Ferromagnetism*. Springer-Verlag Berlin Heidelberg, 2012. ISBN: 978-3-642-25586-0. DOI: doi:10.1007/978-3-642-25583-0. URL: https://doi.org/10.1007/978-3-642-25583-0.

[16] Steven H. Simon. *The Oxford Solid State Basics*. Oxford University Press, Incorporated, 2013.

[17] Manuel M. Müller. 'Coupling phenomena in magnonic hybrid heterostructures'. en. PhD thesis. Technische Universität München, 2023, p. 253.

[18] R. C. O'Handley. *Modern Magnetic Materials: Principles and Applications*. 1st. Wiley, 1999, p. 740.

[19] J. A. Osborn. 'Demagnetizing Factors of the General Ellipsoid'. In: *Physical Review* 67.11 (1945), p. 351.

[20] Amikam Aharoni. 'Demagnetizing factors for rectangular ferromagnetic prisms'. In: *Journal of Applied Physics* 83.6 (Mar. 1998), pp. 3432–3434. ISSN: 0021-8979. DOI: 10.1063/1.367113. eprint: https://pubs.aip.org/aip/jap/article-pdf/83/6/3432/18698969/3432_1_online.pdf. URL: https://doi.org/10.1063/1.367113.

[21] Elena V. Tartakovskaya, Martha Pardavi-Horvath and Manuel Vázquez. 'Configurational spin reorientation phase transition in magnetic nanowire arrays'. In: *Journal of Magnetism and Magnetic Materials* 322.6 (2010), pp. 743–747. ISSN: 0304-8853. DOI: https://doi.org/10.1016/j.jmmm.2009.10.052. URL: https://www.sciencedirect.com/science/article/pii/S0304885309010749.

[22] Martin Maria Decker. 'Spin Current Induced Control of Magnetization Dynamics'. PhD thesis. Universität Regensburg, 2017.

[23] L. Landau and E. Lifshitz. 'On the theory of the dispersion of magnetic permeability in ferromagnetic bodies. Reprinted from Physikalische Zeitschrift der Sowjetunion 8, Part 2, 153, 1935.' In: (1992). Ed. by L.P. PITAEVSKI, pp. 51–65. DOI: https://doi.org/10.1016/B978-0-08-036364-6.50008-9. URL: https://www.sciencedirect.com/science/article/pii/B9780080363646500089.

[24] J. Anthony C. Bland and Bretislav Heinrich. *Ultrathin Magnetic Structures III: Fundamentals of Nanomagnetism*. Springer Berlin, Heidelberg, 2005. ISBN: 978-3-540-21953-8. DOI: 10.1007/b138703.

[25] T.L. Gilbert. 'A phenomenological theory of damping in ferromagnetic materials'. In: *IEEE Transactions on Magnetics* 40.6 (2004), pp. 3443–3449. DOI: 10.1109/TMAG.2004.836740.

[26] D. Polder. 'VIII. On the theory of ferromagnetic resonance'. In: *The London, Edinburgh, and Dublin Philosophical Magazine and Journal of Science* 40.300 (1949), pp. 99–115. DOI: 10.1080/14786444908561215.

[27] Charles Kittel. 'On the Theory of Ferromagnetic Resonance Absorption'. In: *Phys. Rev.* 73 (2 Jan. 1948), pp. 155–161. DOI: 10.1103/PhysRev.73.155. URL: https://link.aps.org/doi/10.1103/PhysRev.73.155.

[28] Alexander Altland and Ben Simons. 'Response Functions'. In: *Condensed Matter Field Theory*. Cambridge University Press, 2023, pp. 384–418.

[29] Stefan Horst Klingler. 'Magnetization dynamics in coupled magnetic systems'. en. PhD thesis. Technische Universität München, 2019, p. 162. URL: https://mediatum.ub.tum.de/1482691.

[30] S. Blundell. *Magnetism in Condensed Matter*. Oxford Master Series in Condensed Matter Physics. OUP Oxford, 2001. ISBN: 9780198505914. URL: https://books.google.de/books?id=OGhGmgEACAAJ.

[31] V. V. Kruglyak, S. O. Demokritov and D. Grundler. 'Magnonics'. In: *2010 IOP Publishing Ltd* (June 2010).

[32] A. V. Chumak et al. 'Magnon spintronics'. In: *Nature Physics* 11.6 (2015), pp. 453–461. ISSN: 1745-2481. DOI: 10.1038/nphys3347. URL: https://doi.org/10.1038/nphys3347.

[33] Luis Antonio Flacke. 'Spin-wave transport and skyrmion formation in CoFe-based thin film heterostructures'. en. PhD thesis. Technische Universität München, 2022, p. 125. URL: https://mediatum.ub.tum.de/1637205.

[34] Gavin S. Abo et al. 'Definition of Magnetic Exchange Length'. In: *IEEE Transactions on Magnetics* 49.8 (2013), pp. 4937–4939. DOI: 10.1109/TMAG.2013.2258028.

[35] Anil Prabhakar and Daniel D. Stancil. *Spin Waves: Theory and Applications*. 1st ed. Engineering (R0). Published: 17 April 2009. New York, NY: Springer New York, NY, 2009, pp. XII, 348. ISBN: 978-0-387-77864-8. DOI: 10.1007/978-0-387-77865-5. URL: https://doi.org/10.1007/978-0-387-77865-5.

[36] B A Kalinikos and A N Slavin. 'Theory of dipole-exchange spin wave spectrum for ferromagnetic films with mixed exchange boundary conditions'. In: *Journal of Physics C: Solid State Physics* 19.35 (Dec. 1986), p. 7013. DOI: 10.1088/0022-3719/19/35/014. URL: https://dx.doi.org/10.1088/0022-3719/19/35/014.

[37] R.W. Damon and J.R. Eshbach. 'Magnetostatic modes of a ferromagnet slab'. In: *Journal of Physics and Chemistry of Solids* 19.3 (1961), pp. 308–320. ISSN: 0022-3697. DOI: https://doi.org/10.1016/0022-3697(61)90041-5. URL: https://www.sciencedirect.com/science/article/pii/0022369761900415.

[38] R.E. Camley. 'Nonreciprocal surface waves'. In: *Surface Science Reports* 7.3 (1987), pp. 103–187. ISSN: 0167-5729. DOI: https://doi.org/10.1016/0167-5729(87)90006-9. URL: https://www.sciencedirect.com/science/article/pii/0167572987900069.

[39] M. Kostylev. 'Non-reciprocity of dipole-exchange spin waves in thin ferromagnetic films'. In: *Journal of Applied Physics* 113.5 (Feb. 2013), p. 053907. ISSN: 0021-8979. DOI: 10.1063/1.4789962. eprint: https://pubs.aip.org/aip/jap/article-pdf/doi/10.1063/1.4789962/15105963/053907_1_online.pdf. URL: https://doi.org/10.1063/1.4789962.

[40] O. Gladii et al. 'Frequency nonreciprocity of surface spin wave in permalloy thin films'. In: *Phys. Rev. B* 93 (5 Feb. 2016), p. 054430. DOI: 10.1103/PhysRevB.93.054430. URL: https://link.aps.org/doi/10.1103/PhysRevB.93.054430.

[41] Kin L. Wong et al. 'Unidirectional propagation of magnetostatic surface spin waves at a magnetic film surface'. In: *Applied Physics Letters* 105.23 (Dec. 2014), p. 232403. ISSN: 0003-6951. DOI: 10.1063/1.4903742. eprint: https://pubs.aip.org/aip/apl/article-pdf/doi/10.1063/1.4903742/13674028/232403_1_online.pdf. URL: https://doi.org/10.1063/1.4903742.

[42] L. D. Landau and E. M. Lifshitz. *Electrodynamics of Continuous Media*. 2nd. Oxford: Butterworth-Heinemann, 1984.

[43] Avner Friedman. 'Micromagnetics'. In: *Mathematics in Industrial Problems: Part 5*. New York, NY: Springer New York, 1992, pp. 182–192. ISBN: 978-1-4615-7405-7. DOI: 10.1007/978-1-4615-7405-7_17. URL: https://doi.org/10.1007/978-1-4615-7405-7_17.

[44] D Kumar and A O Adeyeye. 'Techniques in micromagnetic simulation and analysis'. In: *Journal of Physics D: Applied Physics* 50.34 (July 2017), p. 343001. DOI: 10.1088/1361-6463/aa7c04. URL: https://dx.doi.org/10.1088/1361-6463/aa7c04.

[45] Arne Vansteenkiste et al. 'The design and verification of Mumax3'. In: *AIP Advances* 4.10 (2014), p. 107133. DOI: 10.1063/1.4899186. URL: http://doi.org/10.1063/1.4899186.

[46] W Brown. *Micromagnetics*. Interscience Tracts on Physics and Astronomy. New York: Interscience, 1963.

[47] Sang-Koog Kim. 'Micromagnetic computer simulations of spin waves in nanometre-scale patterned magnetic elements'. In: *Journal of Physics D: Applied Physics* 43.26 (June 2010), p. 264004. DOI: 10.1088/0022-3727/43/26/264004. URL: https://dx.doi.org/10.1088/0022-3727/43/26/264004.

[48] Akira Tezuka. 'Finite Element and Finite Difference Methods'. In: *Springer Handbook of Materials Measurement Methods*. Ed. by Horst Czichos, Tetsuya Saito and Leslie Smith. Berlin, Heidelberg: Springer Berlin Heidelberg, 2006, pp. 973–1000. ISBN: 978-3-540-30300-8. DOI: 10.1007/978-3-540-30300-8_19. URL: https://doi.org/10.1007/978-3-540-30300-8_19.

[49] J. Leliaert and J. Mulkers. 'Tomorrow's micromagnetic simulations'. In: *Journal of Applied Physics* 125.18 (May 2019), p. 180901. ISSN: 0021-8979. DOI: 10.1063/1.5093730. eprint: https://pubs.aip.org/aip/jap/article-pdf/doi/10.1063/1.5093730/15225107/180901_1_online.pdf. URL: https://doi.org/10.1063/1.5093730.

[50] *The Go Programming Language Specification*. URL: https://go.dev/ref/spec (visited on 21/05/2024).

[51] John Nickolls et al. 'Scalable Parallel Programming with CUDA: Is CUDA the parallel programming model that application developers have been waiting for?' In: *Queue* 6.2 (Mar. 2008), pp. 40–53. ISSN: 1542-7730. DOI: 10.1145/1365490.1365500. URL: https://doi.org/10.1145/1365490.1365500.

[52] J.C. Butcher. *Differential and Difference Equations*. John Wiley Sons, Ltd, 2016. DOI: https://doi.org/10.1002/9781119121534.ch1. eprint: https://onlinelibrary.wiley.com/doi/pdf/10.1002/9781119121534.ch1. URL: https://onlinelibrary.wiley.com/doi/abs/10.1002/9781119121534.ch1.

[53] C.E. Shannon. 'Communication in the Presence of Noise'. In: *Proceedings of the IRE* 37.1 (Jan. 1949), pp. 10–21. DOI: 10.1109/jrproc.1949.232969. URL: https://doi.org/10.1109/jrproc.1949.232969.

[54] *MuMax3 FAQ*. URL: https://mumax.ugent.be/mumax3-workshop/questions.html (visited on 21/05/2024).

[55] G. Venkat et al. 'Proposal for a Standard Micromagnetic Problem: Spin Wave Dispersion in a Magnonic Waveguide'. In: *IEEE Transactions on Magnetics* 49.1 (2013), pp. 524–529. DOI: 10.1109/TMAG.2012.2206820.

[56] *MuMax3 API*. URL: http://mumax.github.io/api.html (visited on 21/05/2024).

[57] Hannes Maier-Flaig et al. 'Note: Derivative divide, a method for the analysis of broadband ferromagnetic resonance in the frequency domain'. In: *Review of Scientific Instruments* 89.7 (July 2018), p. 076101. ISSN: 0034-6748. DOI: 10.1063/1.5045135. eprint: https://pubs.aip.org/aip/rsi/article-pdf/doi/10.1063/1.5045135/13420020/076101_1_online.pdf. URL: https://doi.org/10.1063/1.5045135.

[58] H. J. von Bardeleben, J. L. Cantin and F. Gendron. 'Ferromagnetic Resonance Spectroscopy: Basics and Applications'. In: *Electron Paramagnetic Resonance Spectroscopy: Applications*. Cham: Springer International Publishing, 2020, pp. 351–383. ISBN: 978-3-030-39668-8. DOI: 10.1007/978-3-030-39668-8_12. URL: https://doi.org/10.1007/978-3-030-39668-8_12.

[59] X. Zhou et al. 'Axially and radially quantized spin waves in thick permalloy nanodots'. In: *Phys. Rev. B* 92 (5 Aug. 2015), p. 054401. DOI: 10.1103/PhysRevB.92.054401. URL: https://link.aps.org/doi/10.1103/PhysRevB.92.054401.

[60] Kai Wagner et al. 'Numerical Ferromagnetic Resonance Experiments in Nanosized Elements'. In: *IEEE Magnetics Letters* 12 (2021), pp. 1–5. DOI: 10.1109/LMAG.2021.3055447.

[61] A. Ciuciulkaite. 'Micromagnetic simulations of magnetization dynamics in iron-palladium nanostructure arrays'. MA thesis. Uppsala University, 2016. URL: https://urn.kb.se/resolve?urn=urn:nbn:se:uu:diva-302889.

[62] Dheeraj Kumar et al. 'Numerical calculation of spin wave dispersions in magnetic nanostructures'. In: *Journal of Physics D: Applied Physics* 45.1 (Dec. 2011), p. 015001. DOI: 10.1088/0022-3727/45/1/015001. URL: https://dx.doi.org/10.1088/0022-3727/45/1/015001.

[63] Zhiwei Ren et al. 'MuFA (Multi-type Fourier Analyzer): A tool for batch generation of MuMax3 input scripts and multi-type Fourier analysis from micromagnetic simulation output data'. In: *Computer Physics Communications* 244 (2019), pp. 311–318. ISSN: 0010-4655. DOI: https://doi.org/10.1016/j.cpc.2019.06.023. URL: https://www.sciencedirect.com/science/article/pii/S0010465519302115.

[64] J. Feilhauer et al. 'Unidirectional spin-wave edge modes in magnonic crystal'. In: *APL Materials* 11.2 (Feb. 2023), p. 021104. ISSN: 2166-532X. DOI: 10.1063/5.0134099. eprint: https://pubs.aip.org/aip/apm/article-pdf/doi/10.1063/5.0134099/16696084/021104_1_online.pdf. URL: https://doi.org/10.1063/5.0134099.

[65] J. E. Bresenham. 'Algorithm for computer control of a digital plotter'. In: *IBM Systems Journal* 4.1 (1965), pp. 25–30. DOI: 10.1147/sj.41.0025.

[66] H. S. Körner et al. 'Magnetic damping in poly-crystalline Co25Fe75: Ferromagnetic resonance vs. spin wave propagation experiments'. In: *Applied Physics Letters* 111.13 (Sept. 2017), p. 132406. ISSN: 0003-6951. DOI: 10.1063/1.4994137. eprint: https://pubs.aip.org/aip/apl/article-pdf/doi/10.1063/1.4994137/14503565/132406_1_online.pdf. URL: https://doi.org/10.1063/1.4994137.

[67] J. Ding, M. Kostylev and A. O. Adeyeye. 'Magnetic hysteresis of dynamic response of one-dimensional magnonic crystals consisting of homogenous and alternating width nanowires observed with broadband ferromagnetic resonance'. In: *Phys. Rev. B* 84 (5 Aug. 2011), p. 054425. DOI: 10.1103/PhysRevB.84.054425. URL: https://link.aps.org/doi/10.1103/PhysRevB.84.054425.

[68] Jesco Topp, Detlef Heitmann and Dirk Grundler. 'Interaction effects on microwave-assisted switching of $Ni_{80}Fe_{20}$ nanowires in densely packed arrays'. In: *Phys. Rev. B* 80 (17 Nov. 2009), p. 174421. DOI: 10.1103/PhysRevB.80.174421. URL: https://link.aps.org/doi/10.1103/PhysRevB.80.174421.

[69] M. P. Kostylev, A. A. Stashkevich and N. A. Sergeeva. 'Collective magnetostatic modes on a one-dimensional array of ferromagnetic stripes'. In: *Phys. Rev. B* 69 (6 Feb. 2004), p. 064408. DOI: 10.1103/PhysRevB.69.064408. URL: https://link.aps.org/doi/10.1103/PhysRevB.69.064408.

[70] A. O. Adeyeye et al. 'Magnetostatic interactions and magnetization reversal in ferromagnetic wires'. In: *Phys. Rev. B* 56 (6 Aug. 1997), pp. 3265–3270. DOI: 10.1103/PhysRevB.56.3265. URL: https://link.aps.org/doi/10.1103/PhysRevB.56.3265.

[71] Bharat B. Pant. 'Effect of interstrip gap on the sensitivity of high sensitivity magnetoresistive transducers'. In: *Journal of Applied Physics* 79.8 (Apr. 1996), pp. 6123–6125. ISSN: 0021-8979. DOI: 10.1063/1.362107. eprint: https://pubs.aip.org/aip/jap/article-pdf/79/8/6123/18684042/6123_1_online.pdf. URL: https://doi.org/10.1063/1.362107.

[72] G. Gubbiotti et al. 'Collective spin modes in monodimensional magnonic crystals consisting of dipolarly coupled nanowires'. In: *Applied Physics Letters* 90.9 (Feb. 2007), p. 092503. ISSN: 0003-6951. DOI: 10.1063/1.2709909. eprint: https://pubs.aip.org/aip/apl/article-pdf/doi/10.1063/1.2709909/13160329/092503_1_online.pdf. URL: https://doi.org/10.1063/1.2709909.

[73] A.O Adeyeye, M.K Husain and V Ng. 'Magnetic properties of lithographically defined lateral Co/Ni80Fe20 wires'. In: *Journal of Magnetism and Magnetic Materials* 248.3 (2002), pp. 355–359. ISSN: 0304-8853. DOI: https://doi.org/10.1016/S0304-8853(02)00336-0. URL: https://www.sciencedirect.com/science/article/pii/S0304885302003360.

[74] S. Goolaup et al. 'Magnetization switching in alternating width nanowire arrays'. In: *Phys. Rev. B* 75 (14 Apr. 2007), p. 144430. DOI: 10.1103/PhysRevB.75.144430. URL: https://link.aps.org/doi/10.1103/PhysRevB.75.144430.

[75] Robert E. Camley and Karen L. Livesey. 'Consequences of the Dzyaloshinskii-Moriya interaction'. In: *Surface Science Reports* 78.3 (2023), p. 100605. ISSN: 0167-5729. DOI: https://doi.org/10.1016/j.surfrep.2023.100605. URL: https://www.sciencedirect.com/science/article/pii/S0167572923000201.

[76] R. A. Gallardo et al. 'Flat Bands, Indirect Gaps, and Unconventional Spin-Wave Behavior Induced by a Periodic Dzyaloshinskii-Moriya Interaction'. In: *Phys. Rev. Lett.* 122 (6 Feb. 2019), p. 067204. DOI: 10.1103/PhysRevLett.122.067204. URL: https://link.aps.org/doi/10.1103/PhysRevLett.122.067204.

[77] J. Flores-Farías et al. 'Omnidirectional flat bands in chiral magnonic crystals'. In: *Scientific Reports* 12.1 (25th Oct. 2022), p. 17831. ISSN: 2045-2322. DOI: 10.1038/s41598-022-20539-3. URL: https://doi.org/10.1038/s41598-022-20539-3.

[78] Szymon Mieszczak and Jarosław W. Kłos. 'Interface modes in planar one-dimensional magnonic crystals'. In: *Scientific Reports* 12.1 (5th July 2022), p. 11335. ISSN: 2045-2322. DOI: 10.1038/s41598-022-15328-x. URL: https://doi.org/10.1038/s41598-022-15328-x.

Acknowledgments

Am Ende meiner Masterarbeit und damit auch meines Physikstudiums möchte ich allen danken, ohne die diese Arbeit nicht möglich gewesen wäre. Mein Jahr am Walther-Meißner-Institut in Garching durfte ich an der Seite von vielen inspirierenden Personen verbringen, die stets ein angenehmes Arbeitsklima geschaffen haben. Von daher möchte ich mich beim gesamten WMI-Personal für die eindrucksreiche Zeit herzlich bedanken. Im Besonderen gilt mein Dank:

Prof. Dr. Rudolf Gross für die Möglichkeit, meine Master Thesis am Walther-Meißner-Institut zu schreiben. In besonderer Weise hat er diese Arbeit durch das unkomplizierte Genehmigen eines neuen Simulationsrechners unterstützt.

Dr. Stephan "Steve" Geprägs, der mich während meiner Thesis beraten und meine Aufmerksamkeit auf dieses Thema gelenkt hat. Für dein großes Vertrauen in meine Arbeit und dafür, dass du trotz allem immer Zeit für mich gefunden hast wenn ich Fragen hatte, bin ich sehr dankbar. Deine Motivation für das Thema war sehr ansteckend und es war immer spannend, neue Ergebnisse mit dir zu diskutieren. Ich möchte dir für deine zahlreichen Beiträge dieser Arbeit danken, zwischen neuen Ideen, genereller Ratschläge und deiner immer positiven Einstellung, nicht zuletzt aber auch für dein aufwendiges Korrekturlesen dieser Arbeit.

Monika Scheufele, für die enorme Zeit, die du in meine Betreuung investiert hast. Dafür, dass du quasi immer erreichbar warst, wenn ich Fragen oder Probleme hatte, aber auch für die lustigen Gespräche abseits des Themas. Nicht zuletzt möchte ich auch dir für deine große Geduld beim Korrekturlesen der Arbeit danken.

Matthias Grammer und **Manuel Müller**, für die nützlichen Diskussionen über nanogratings.

Meinen Masterkollegen, insbesondere **Florian Maier**, **Jan Wozniak**, **Julius Feigl**, **Nicolas Jungwirth** & **Vincent Koch**, für die unterhaltsamen Mittagspausen, die gemeinsamen Diskussionen und eure Ratschläge, wenn ich irgendwo nicht weiter kam. Unsere gemeinsamen Kaffeepausen waren eine große

Bereicherung und haben in jeder Phase dieser Thesis dazu beigetragen, dass ich Spaß an der Arbeit hatte.

All meinen Freunden, in und abseits der Universität. Für euren stetigen Rückhalt und die tolle gemeinsame Zeit bin ich sehr dankbar. Dafür, dass ihr immer ein offenes Ohr für mich habt und mich im positiven Sinne auch mal von der Uni ablenken konntet. Ohne euch hätte ich mein Studium sicher nicht gemeistert.

Meinen Eltern für ihre unbeschreibliche Unterstützung und die Möglichkeit, studieren zu können. Nicht zuletzt habt ihr das auch finanziell erst ermöglicht. **Meinen Schwestern** für euren emotionalen Beistand und dafür, dass ich mit euch immer gut lachen kann.

Zuletzt gilt besonderer Dank meiner Freundin **Gloria**, die mich nicht nur im Rahmen dieser Arbeit, sondern durch verschiedene Phasen des Studiums immer unterstützt und motiviert hat.